To the Graduate Council:

I am submitting herewith a dissertation written by Terry Evans Vaughn entitled "Photochemistry of Chlorobenzene Interacting with the Surface of Amorphous Ice." I have examined the final copy of this dissertation for form and content and recommend that it be accepted in partial fulfillment of the requirements for the degree of Doctor of Philosophy, with a major in Chemistry.

Dr. Fred Grimm, Major Professor

We have read this dissertation
and recommend its acceptance

Accepted for the Council:

Associate Vice Chancellor and
Dean of The Graduate School

Photochemistry of Chlorobenzene Interacting with the Surface of Amorphous Ice

A Dissertation

Presented for the

Doctor of Philosophy

Degree

The University of Tennessee, Knoxville

Terry Evans Vaughn

December 1998

ACKNOWLEDGMENTS

The author would like to give thanks to a few people who through their influences facilitated the production of this volume. The first few years of graduate school would have been difficult without the companionships of Charles Ngowe, Randy Hayes, and Dan Marsh. I am in debt to these three people for fruitful discussions and endless debates over what was considered at the time fundamental chemistry. These discussions sparked a much needed competitive chord within those who participated and aided in completion of unsavory tasks. The author would also like to thank Sabella Bowers for her friendship and support. She has been a good friend, and her companionship made graduate school a little more bearable.

Also, the author would like to thank the following people for their support and advice, be it personal or scientific: Carol Moulton, Pat Martin, Dr. William Bull, Dr. Alex Van Hook, and Dr. Charles Feigerle. Special thanks goes to Dr. R.J. Hinde for his support and counseling. Also, thanks goes to Dr. Debra Huntley and co-workers at ORNL for the use of their instrumentation and for lively discussions. The author would like to extend a special thanks to his advisor, Dr. Fred Grimm, for his continued support throughout the program and above all for his remarkable patience. His counseling and discussions have proven to be invaluable and his efforts are greatly appreciated.

Finally, the author would like to thank his family for their support and encouragement. This work would not have been possible were it not for their presence. This work is dedicated to the author's family in hopes that they celebrate their accomplishment.

ABSTRACT

The photochemistry of chlorobenzene adsorbed to an amorphous ice surface has been investigated at ultra-high vacuum (UHV). Ultra-thin ice films (< 50 Å) were grown on the surface of a Ni (111) crystal in a vacuum chamber evacuated at a pressure on the order of 10^{-10} torr. These thin ice films were determined to be continuous and void of large cracks and fissures which might expose the underlying nickel substrate. Various exposures of chlorobenzene were dosed to the amorphous ice surface at both submonolayer and multilayer coverages. Broad band UV irradiation of this system produced benzene as the primary photolysis product as determined by thermal desorption spectroscopy (TDS). The chlorine, once photodissociated from the phenyl ring, was determined to diffuse through the ice layers to the nickel surface. A thermal desorption spectrum taken after irradiation indicated no chlorine species to desorb from the surface of the ice except for the parent chlorobenzene. The chlorobenzene adsorbate showed only physisorption to the ice surface with no evidence for any stronger interaction. Deuteration studies indicated that the source of hydrogen to form the benzene during irradiation was primarily from an adjacent phenyl ring species and not from the ice surface. This implies stronger lateral interaction between the adsorbates and appreciable mobility of chlorobenzene on the ice surface. Thermal desorption profiles of multilayer chlorobenzene adsorbed to ice also corroborates the apparent weak interaction at the interfacial region. Interestingly, it was found that multilayer chlorobenzene had a higher desorption temperature than did monolayer chlorobenzene from the ice surface. This indicates that the chlorobenzene-chlorobenzene interaction is potentially larger than the chlorobenzene-H_2O interaction. A

possible explanation for the observed desorption profiles is that island aggregation of chlorobenzene is occurring on the ice surface. These islands could contain multilayer coverages of chlorobenzene at the center and taper to monolayer coverages at the edges. Desorption for the monolayer coverage at the edges of the islands with a steady reduction in island size is thought to explain the observed temperature profiles of monolayer and multilayer coverages. Island aggregation would also facilitate the experimentally observed abstraction of hydrogens from adjacent phenyl compounds.

Theoretical calculations at the ab initio level, including Hartree-Fock and higher order corrections, were performed to investigate the interactions at the interfacial region of the adsorbate and ice surface. One to one molecular complexes of chlorobenzene and H_2O were explored as precursors to the larger macroscopic interfacial system. Binding energies of benzene, chlorobenzene, and fluorobenzene with H_2O were calculated. Benzene and fluorobenzene were theoretically investigated for the purposes of comparing the effects of ring substitution on the binding interactions. It was found that benzene possessed a higher binding energy than did the substituted benzene compounds. Interestingly, the chlorobenzene and fluorobenzene complexes were shown to have very similar binding energies. Global minimums for all three hydrogen bonded complexes were found with H_2O acting as the proton donor and the phenyl ring acting as the electron donation source. Chlorobenzene was found to be participating in a possible double hydrogen bonded complex with H_2O. One of the H_2O hydrogens was preferentially directed toward the para-carbon on the phenyl ring in what appears to be a σ-type hydrogen bond with the p_y orbital of the para-carbon. The other hydrogen is directed over

the center of the ring in a more traditional π-type hydrogen bond. Vibrational frequencies were also calculated to complement the theoretical investigation of the hydrogen bonding interaction of the complexes.

Calculations on the possible interactions of atomic chlorine with ice were also carried out to explore chlorine radical complexation with H_2O monomers within the ice with relevancy to possible mechanisms for chlorine diffusion. Binding energies and preferred complex geometries for the chlorine anion and chlorine radical complex formation with H_2O were determined for one to one complexes. H_2OCl^- has been investigated previously and is used here for comparative purposes. The structure and binding energies reported previously are in excellent agreement with our work. H_2OCl has not been previously investigated either experimentally or theoretically. The H_2OCl radical complex was found to have a binding energy of 1.8 kcal/mol. The interactions between a chlorine anion and a chlorine radical with H_2O were found to be distinctly different in mechanism and orientation. The chlorine radical is bound to the H_2O monomer through a lone pair on the oxygen in a tetrahedral arrangement whereas the chlorine anion displayed a more traditional hydrogen bonded interaction. The geometry of the ionized form of the radical complex, H_2OCl^+, was also theoretically determined. Calculated vibrational frequencies were compared to recently reported experimental values of the cation complex. The complex has been recently proposed to act as an intermediate in heterogeneous reactions occurring on stratospheric ice particulates over Antarctica.

CONTENTS

CHAPTER		PAGE
INTRODUCTION		1
I	BACKGROUND	15
II	EXPERIMENTAL PROCEDURES	33
III	EXPERIMENTAL RESULTS	43
	RESULTS	45
	H_2O/Ni(111)	45
	Chlorobenzene/Ni(111)	47
	Photolysis of chlorobenzene/Ni(111)	49
	Chlorobenzene/H_2O/Ni(111)	50
	Photolysis of chlorobenzene/ice	52
	XPS of chlorobenzene/ice	55
	DISCUSSION	59
	CONCLUSION	64
IV	THEORETICAL TECHNIQUES	66
V	THEORETICAL RESULTS OF CHLOROBENZENE AND CHLOROBENZENE-H_2O COMPLEX	74
	GEOMETRY AND ENERGETICS	76
	Geometry of benzene	76
	Geometry of chlorobenzene	80
	Dipole moment of chlorobenzene	85
	Benzene-H_2O	87
	Chlorobenzene-H_2O	93
	Binding energy	96
	VIBRATIONAL ANALYSIS	98
	Benzene	98
	Chlorobenzene	104
	Chlorobenzene-H_2O	111
	DISCUSSION	117

VI CHLORINE ANION AND RADICAL COMPLEXATION WITH WATER 123

H_2OCl^- 124

Geometry 124
Dipole 126
Vibrational frequencies 126
Energy 129
NBO analysis 134

H_2OCl 140

Geometry 140
Dipole 143
Vibrational frequencies 146
Energy 146
NBO analysis 150

DISCUSSION 152

H_2OCl^+ 157

CONCLUSION 165

LIST OF REFERENCES 169

VITA 176

LIST OF FIGURES

1-1 Schematic diagram of the thermal divisions of the atmosphere as a function of altitude in kilometers. 17

1-2 Diagram of solar radiation incident on the earth's atmosphere as a function of wavelength in microns. Radiation flux is given in units of W/m^2. 20

1-3 Total ozone observations above Halley Bay and the South Pole showing the development of the ozone hole. Total chlorine abundances in the troposphere and stratosphere are also indicated, based on an assumed 3.5 year lag time between the two atmospheric regimes. Natural chlorine abundances are believed to be ~ .6 ppbv, with man-made chlorine making up the remainder of the stratospheric chlorine budget. (taken from Farman et al.). 24

3-1 Thermal desorption spectrum of H_2O (m/e=18) adsorbed to Ni(111) for various coverages. H_2O was dosed for all coverages at T<100K. Desorption peaks at 168K and 173K are assigned as multilayer and monolayer desorption species respectively. The temperature ramp is 5K/s. 46

3-2. Thermal desorption spectrum of chlorobenzene (m/e=112) directly adsorbed to the nickel(111) surface. The nickel crystal was heated from 100K to 800K at a temperature ramp of 5K/s. The inset is an

Auger spectrum after thermal desorption and subsequent cooling. The chlorine signature is seen at 180eV. The peaks at 60 eV and 840 eV are Auger electron energies characteristic of nickel. 48

3-3 Chlorobenzene desorption profile from an ice surface as a function of various coverages. Both chlorobenzene and H_2O were dosed at T<100K. The ice coverage is approximately 18ML. Chlorobenzene is monitored as m/e=112. The temperature ramp is 5K/s. 51

3-4 Thermal desorption spectrum of a UV irradiated sample of chlorobenzene adsorbed to an ice surface. Irradiation time is 30min. The crystal was ramped to 800K at 5K/s. Both chlorobenzene and H_2O were dosed at T<100K. The photoproduct formed is benzene(m/e=78), which desorbs at a temperature ~ 145K. The small shoulder at a slightly higher temperature is a cracking fragment of chlorobenzene at an ionization energy of 70eV. 53

3-5 Isotopic study of deuterated chlorobenzene(m/e=117) adsorbed to an amorphous ice surface. Sample was irradiated for 30min and then thermally desorbed to 800K. Both chlorobenzene and H_2O were dosed to the nickel at T<100K. Partially deuterated benzene(m/e=83) and fully deuterated benzene(m/e=84) were monitored during the desorption process. Fully deuterated benzene is clearly shown to have a greater intensity than partial deuterated

benzene suggesting preferred hydrogen abstraction from an adjacent phenyl ring. 56

3-6 An XPS spectrum of chlorobenzene adsorbed to an ice surface. Both species were dosed at T<100K. The chlorine 2p energy level was monitored for various irradiation intervals. The chlorine 2p signal was acquired for 1) chlorobenzene adsorbed to ice before irradiation, 2) after the sample was irradiated for 11min, and 3) after thermal desorption to 800K which shows chlorine adsorbed to the nickel surface. 58

3-7 A leading edge analysis for a zeroth order plot of the natural log of the desorption rate versus inverse temperature. Both curves represent chlorobenzene desorption from an amorphous ice film. The lower E_{act} is shown for the α- chlorobenzene directly interacting with the ice surface. The higher E_{act} is given for the condensed ß-phase chlorobenzene. 60

5-1 Optimized geometry of benzene at RHF/6-31G* with verytight convergence criteria. Structure has D_{6h} symmetry. 77

5-2 Optimized geometry of chlorobenzene at RHF/6-31G* with verytight convergence criteria. Structure has C_{2v} symmetry. 81

5-3 Optimized geometry for benzene-H_2O calculated at RHF/6-31G*. The structure has C_s symmetry. θ = 15-13-X-4 dihedral. 90

5-4 Orientational considerations of H_2O complexes with benzene and chlorobenzene. 92

5-5 Fully optimized minimum geometry for chlorobenzene-H_2O calculated at RHF/6-31G*. Complex has C_1 symmetry. 95

5-6 B_{2u} normal mode of vibration for benzene. 102

5-7a Calculated normal modes of vibration for chlorobenzene at the RHF/6-31G* level of theory. 105

5-7b Calculated normal modes of vibration for chlorobenzene at the RHF/6-31G* level of theory. 106

5-7c Calculated normal modes of vibration for chlorobenzene at the RHF/6-31G* level of theory. 107

5-8 Intermolecular modes of the chlorobenzene-H_2O complex. The plane of the chlorobenzene ring is in the xy plane with the plane of the water molecule in the yz plane bisecting the C_2 axis from a perpendicular direction. 114

6-1 Calculated structure of the chlorine anion complex with H_2O at RHF/6-31+G*. Complex has C_s symmetry. 125

6-2 Vibrational displacements for the intermolecular modes of H_2OCl^-. Complex has C_s symmetry. 130

6-3 Trial geometry of H_2OCl^- complex for angle considerations. 138

6-4 Geometry of the H_2OCl radical complex calculated at the UHF/6-31+G* level of theory. The structure has C_s symmetry. 141

6-5 Vibrational displacements for the intermolecular normal modes of the H_2OCl radical complex calculated at UHF/6-31+G*. 148

6-6 Optimized geometry for the H_2OCl^+ cation at the MP2/6-311++G** level of theory. Cation possesses C_s symmetry. The chlorine dihedral with the H-O-H plane is 122.9401 °. 160

LIST OF TABLES

4-1	Constants used by *Gaussian 92* program package.	67
5-1	Calculated values for benzene at various levels of theory. Convergence criteria for optimization is verytight.	78
5-2	Optimized values for chlorobenzene at various levels of theory. See Figure 5-2 for numbering scheme. Polarizabilities are given in xx, yy, zz tensors along with the average value in parentheses.	82
5-3a	Optimized values for chlorobenzene at the MP2 level of theory. Optimization is at verytight convergence criteria. See Figure 5-2 for numbering scheme.	86
5-3b	Optimized values for chlorobenzene at the BLYP level of theory. Optimization is at verytight convergence criteria. See Figure 5-2 for numbering scheme.	88
5-3c	Optimized values for chlorobenzene at the SVWN level of theory Optimization is at verytight convergence criteria. See Figure 5-2 for numbering scheme.	89
5-4	Calculated values for H_2O complexes with benzene, chlorobenzene, and fluorobenzene at both the RHF/6-31G* and MP2/6-31G*//RHF/6-31G* levels of theory.	94
5-5	Calculated frequencies for normal modes of vibration for benzene at the RHF/6-31G* level of theory.	99

5-6 Calculated vibrational frequencies for chlorobenzene at the RHF/6-31G*. 108

5-7 Correlation Table ($D_{6h} \rightarrow C_{2v}$). Values are calculated at the RHF/6-31G* level of theory. Experimental values are shown in parentheses. Wilson and Mulliken notation is used for labeling modes of benzene. 110

5-8 Calculated vibrational frequencies for chlorobenzene-H_2O complex at RHF/6-31G*. 112

5-9 Natural bond orbital analysis of the bimolecular complexes giving the occupancy of the specified bond orbital. The atomic nomenclature can be seen in figure 5-5. For fluorobenzene and chlorobenzene, H15 is nearest the para-carbon of the substituted ring. For benzene, the oxygen is labeled 13. 121

6-1a Vibrational frequencies (cm^{-1}) of H_2OCl^- complex and H_2O monomer at the RHF/6-31+G*. 127

6-1b Force constants (mDyne/Å) for H_2OCl^- complex and H_2O monomer at the RHF/6-31+G*. 127

6-2 Calculated values for the Chlorine anion-Water Complex(H_2OCl^-). The values were calculated with a 6-31+G* level of theory. 131

6-3 Calculated values for the fully optimized H2OCl$^-$ Complex under MP2/6-31+G*. 133

6-4 Occupation of natural bond orbitals in H_2OCl^- complex as a function of monomer separation (R). 135

6-5a Charge occupation and energy for H_2OCl^- complex as a function of angle (α). Angle considerations are shown in Figure 6-3. 136

6-5b Charge occupation and energy for H_2OCl^- complex as a function of angle (β). See figure 6-3. 137

6-6 Calculated values for the Chlorine Radical-Water Complex (H_2OCl) using a basis set of 6-31+G* at the UHF level. Complex is C_s symmetry. 142

6-7 Calculated values for H_2OCl radical complex with various basis sets. 144

6-8 Calculated values for Chlorine and H_2O radical complex MP2/6-31+G*. 145

6-9a Calculated Vibrational Frequencies for the Chlorine-H_2O radical complex. 147

6-9b Calculated Force Constants (mDyne/Å) for H_2OCl. 147

6-10a Occupation of natural bond orbitals in H_2OCl radical complex. Alpha spin. Values are calculated as a function of monomer separation at the UHF/6-31+G* optimized geometry. 151

6-10b Occupation of natural bond orbitals in H_2OCl radical complex. Beta spin. 151

6-11 An NBO analysis showing charge occupation values for the stable optimized chlorine anion complex (B) shown in figure 5-1 and the complex with the chlorine anion replaced by the chlorine radical for the same (above) geometry (A). Values calculated at the UHF/6-31+G* and RHF/6-31+G* levels of theory respectively. 155

6-12 Calculated values for H_2OCl^+ cation as a function of basis set at the MP2 level of theory. Cation has C_s symmetry. The polarizability values are given in units of $Å^3$ as tensor coordinates xx, yy, zz respectively. The average polarizability is given in parentheses. Both vertical (V) and adiabatic (A) electron affinities are given in units of eV. Dipole moments are calculated in Debye. 159

6-13 Calculated vibrational frequencies for H_2O and H_2OCl^+ at the MP2 level of theory. Experimental values for H_2O were collected from Herzberg. 162

INTRODUCTION

Ice particulates in the stratosphere have been proposed as major contributors to the seasonal reduction of ozone over the polar regions[1-5]. The surfaces of these ice particulates are suspected to act as key reaction sites for the catalytic production of ozone destructive species[6]. However, the exact nature of the surface (and subsurface) of the ice particulates and their involvement in reaction mechanisms are not well understood and are currently under considerable investigation[7-10]. There has recently been a resurgence both experimentally and theoretically in the characterization of ice itself and particularly the surface layers. The previous understanding of pressure induced melting of ice surfaces is being revised, and the surface of ice is now considered to exist in a quasi-liquid state[11].

Organic reactions on an ice surface have recently become an enthusiastic topic for many research groups involved in water interfacial interactions. There have been several attempts to probe the reactivity of the ice surface, but in lieu of a detailed description of the surface of ice, a full understanding of the interface between an adsorbing organic layer and the ice surface is far from achieved. Much less is known about the mechanisms involved in organic reactions occurring in the presence of ice. Most of what is known about this interfacial region is surmised from classical interaction scenarios between either polar or nonpolar adsorbates and the ice surface. It is speculated, however, that hydrogen bonding plays a large role in governing the interfacial interaction and chemistry occurring within this region. Considering the possible liquid-like quality of the ice surface, it is argued whether reactions occurring on ice surfaces can be considered as ionic aqueous or

multi-body gas phase interaction. However, very little experimental information has been gathered to fully support any speculations at this time.

Simulations of ice particulates in the laboratory present difficult challenges especially due to the unusual conditions surrounding ice particulates in the polar stratosphere. These ice particulates are about a micron in size and exist at temperatures between 180 K and 200 K at an altitude of approximately 15-20 Km. The interesting problem for experimentalists is to form predominantly micron size ice particles at temperatures relevant to the polar regions and characterize atmospherically important species adsorbed to these surfaces under similar conditions of the stratosphere.

There are several methods in use to experimentally study ice particles. One method consists of forming these ice particles in inert cryogenic matrices. For an excellent description of this method see Devlin et al[12]. H_2O vapor can be introduced into an evacuated chamber and dosed to a cold ZnS or KCl window and studied spectroscopically. The advantages of this method are low overhead costs and relatively facile experimental procedures. The disadvantages however are very little control of the formation of ice particulates, matrix interferences, and with regards to surface species, adsorbates are usually incorporated into the bulk of the ice instead of on the surface.

Another method to form ice particulates is to utilize a flow reactor[13,14]. A tubular fast-flow reactor allows admitted gases to be injected, usually with a movable coaxial injector, into a cylinder reactor where the water vapor is condensed onto the reactor walls. The cylinder can be coupled to a mass spectrometer to detect the adsorbates of interest. These flow tube reactors have the advantage of simulating atmospheric conditions very well with

respect to the partial pressures of adsorbing species of interest and to temperature control. Impure ice mixtures, such as Type I NAT's (Nitric Acid Trihydrate), are also more facile to form by this method with reasonable control of impurity concentration. Also, due to the understood flow dynamics of this process, diffusion rates and reaction rates are easily found for these flow reactor methods. These methods are usually the choice when investigating adsorbant uptakes by ice substrates. The disadvantage is again lack of control of the surface coverage and ice morphology.

Another alternative, which will be introduced and discussed in this volume, is growing ultra-thin ice films on the surfaces of well characterized substrate crystals (i.e. Ni, W, Pt) under ultra-high vacuum conditions (~ 10^{-10} torr). This technique offers the distinctive advantage of better control of the ice morphology. Also, the ice-adsorbate interface is more easily achieved and characterized on a molecular scale. The disadvantage however, is the operating conditions. Water can be adsorbed to almost any substrate at low temperatures (i.e. < 170 K). As the temperature of the crystal increases however, there is a characteristic temperature at which the water will sublime from the surface of the substrate. For example, nickel (111), which is used in this investigation, has a critical desorption temperature for water of ~ 160 K. This is at least 20 K lower than the formation temperature of ice particulates in the stratosphere. Also, the dimensions of the ice films are quite different than those of the ice particulates in the stratosphere. The surface to volume ratio is much greater for the ice films grown under UHV conditions than the ice particulates. Yet, the thickness of the ice films is approximately four orders of magnitude smaller than the micron size ice particulates. It is not experimentally feasible to

grow ice films larger than ~ 80 monolayers and still maintain an adequate vacuum. Still, the latter technique is by far the better method to investigate the interactions at the interfacial region of organochlorine adsorbates on ice. Also, this technique offers a variety of tools to characterize the adsorbate-ice interface. These include Thermal Desorption Spectroscopy (TDS), X-ray Photoelectron Spectroscopy (XPS), Auger Electron Spectroscopy (AES), and Electron Energy Loss spectroscopy (EELS). The first three are the primary tools used in this volume of work. It was not feasible to utilize EELS for characterization of adsorbates on the ice due to interference from the libration modes of ice. It should be noted here that very few investigations of organic species adsorbed to ice surface with relevance to heterogeneous atmospheric chemistry have been performed under UHV conditions. The author is aware of only two groups (Roberts *et al*[15,16,17], Sodeau *et al*[18]) that have used UHV techniques to investigate adsorbate-ice interactions with emphasis on exploring stratospheric problems. Also, Sodeau's work is unique in that photolysis of the sample was investigated under UHV.

A detailed investigation, from both an experimental and theoretical viewpoint, of the interactions between the ice surface and the adsorbates is the primary focus of this work. However, a description of the ice surface depends on the morphology of the underlying bulk. Water in the solid phase displays a variety of properties depending on the conditions of formation. There are nine structural phases of ice existing at various temperatures and pressures[19]. However, these are all ordered crystal structures, and the ice particulates existing in the stratosphere are of an amorphous nature. It is the amorphous state of ice that is of primary interest here. The structure of the surface of amorphous ice is still being

debated. For example, it is not been determined to what extent the surface is terminated with dangling hydrogens, or oxygens, or some mixture of both. However, recent experimental evidence indicates that the surface of amorphous ice may be populated primarily by non-hydrogen bonded hydrogens[12,17]. This is in contrast to the proposed structures of annealed ice (crystalline ice), which exist as a network of extensive hydrogen bonding. The hydrogen bonding network requires that the surface hydrogens are directed into the bulk to better participate in hydrogen bonding. As a result, crystalline ice is believed to have fewer dangling hydrogens than amorphous ice.

In this work, the interaction of chlorobenzene with an amorphous ice surface is investigated. Chlorobenzene was chosen as the adsorbate for several reasons. It has been proposed that chlorine radicals are the major contributor to ozone destruction[4]. Chlorine radicals are speculated to form in the Antarctic stratosphere from photodissociation of compounds such as Cl_2 and HOCl. These compounds in turn are believe to form on the surfaces of the ice particulates from a heterogeneous reaction involving the two atmospheric reservoir compounds HCl and $ClONO_2$[4].

Due to the obvious importance of chlorine with regards to the mechanisms of ozone depletion in the Antarctic stratosphere, it was sought by this research group to investigate the interactions of chlorine radicals with ice surfaces. Chlorobenzene offered a reasonable choice to accomplish this investigation. It has two important properties which make it a useful compound to investigate chlorine. Chlorobenzene displays unique photochemistry. Upon irradiation in the near UV, chlorobenzene undergoes dissociation along the carbon-chlorine bond. In the gas phase, the homolytic cleavage of the compound is well known to

produce phenyl radicals and chlorine radicals[20,21] and hence a convenient source of chlorine. The other useful property of chlorobenzene is that it has a relatively high sticking coefficient for ice surfaces. Not all compounds will be taken up by ice surfaces. Diatomic chlorine gas, for example, is known not to appreciably stick to ice surfaces. These useful properties along with its easy handling made chlorobenzene the adsorbate of choice.

Theoretical considerations of the interaction between chlorobenzene and a single water molecule are investigated in this work as a precursor to the larger scale interfacial region of chlorobenzene adsorbed to an ice surface. The calculated properties of the interactions for these one to one complexes could lead to valuable information with regards to future modeling of molecular interfaces. The binding forces between chlorobenzene and H_2O are almost exclusively hydrogen bonding. Calculations for a one to one molecular complex show that the water molecule is oriented atop of the chlorobenzene ring with both hydrogens directed toward the ring. With regards to the interfacial region of chlorobenzene adsorbed to the ice surface, this would imply that the dangling hydrogens terminating the surface of the ice could act as binding sites for the chlorobenzene. However, the extent of the interaction between the chlorobenzene and the ice surface would depend on the orientation of the water molecules at the surface.

The interaction between adsorbates and the ice surface is largely comprised of hydrogen bonding and van der Waals interactions depending on the molecular adsorbate. As a result, the interaction energy at the interface is expected to be weak (on the order of 5-10 kcal/mol, i.e. hydrogen bonding), but of course, this depends on the particular

adsorbate. Theoretical investigations into the properties of gas phase-like complexes involving hydrogen bonding can offer unique insight into the binding interaction at the interfacial region. Hydrogen bonded complexes between two individual molecules have been shown to display a variety of properties. For example, the binding energies for a number of hydrogen bonded complexes have been determined and range from 1 kcal/mol to 25 kcal/mol and are known to exhibit a wide variety of binding orientations. Moreover, hydrogen bonding is found to occur in more situations than previously understood. Hydrogen bonding is now known to not only occur for N, O, F containing compounds, but also to Cl[22], C[23], and S[24] as well. One of the more recent topics in hydrogen bonding is the π-hydrogen bond which has received considerable attention as of late[25,26]. The benzene-water complex is probably considered as the quintessential aromatic π-hydrogen bonded system. This complex is known to form a hydrogen bond between the donor hydrogens of water and the conjugated pi ring as the proton acceptor. A complete description of the binding mechanism between the benzene ring and a water molecule and the perturbations brought on by ring substitution (chlorobenzene) could provide information on the binding properties of the interface between an aromatic adsorbate and the ice surface. A description of these one to one complexes could also provide information as to the sticking probability and the surface mobility of the individual adsorbates.

A brief overview of the literature concerning the ozone depletion problem and its dependence on the ice particulates is given in chapter I. A current standing of the theories involved is examined here in detail from the first observation of ozone reduction at Halley

Bay in Antarctica to the present theories which propose to account for the heterogeneous nature of the reduction of ozone. This description is intended solely for the purposes of educating the reader on current advancements regarding the atmospheric chemistry of PSCs and is not to be deemed a necessary portion of the thesis.

In chapter II, a brief description of the experimental techniques used in this work is given. A description of the ultra-high vacuum apparatus is discussed along with the primary investigative tools consisting of X-ray Photoelectron Spectroscopy, Auger Spectroscopy, and Thermal Desorption Spectroscopy. There will also be given a brief description of the method of introduction of ice to the metal substrate and the pros and cons involved in this process.

The experimental results of this investigation will be discussed in chapter III. The photochemistry of chlorobenzene adsorbed to an ice surface was the primary focus of the experimental research. The experimental results are divided into different adsorption regimes and coverages involving chlorobenzene and ice. The coverage of ice used throughout the investigation was on the order of 18 monolayers and represented a continuous surface on which to introduce adsorbates. Several adsorption sequences and coverages were investigated. It was necessary to investigate the surface chemistry of chlorobenzene adsorbed to the nickel surface in sub-monolayer and multilayer coverages to complement and to separate the chemistry indicative of the ice and nickel surfaces. Also, the chemistry of chlorobenzene displayed a dependence on the particular surface (i.e. ice or nickel) it was adsorbed to. For example, chlorobenzene was observed to dissociate along the carbon-chlorine bond once adsorbed to the nickel surface with the production of

benzene and chemisorbed chlorine. On the other hand, chlorobenzene adsorbed to the ice surface shows no such thermal decomposition, and the adsorption process is observed to be reversible. The photochemistry of chlorobenzene shows similar dependencies on adsorption conditions with quantitative respect to product formation. For instance, it was observed that for approximately equal monolayer coverages of both H_2O and chlorobenzene on the nickel substrate there was observed a rather large increase in the production of benzene as the photoproduct after 30 min of irradiation time.

The interaction of chlorine radicals with the ice surface was one of the primary initiatives of this research. Some interesting observations were made for the chlorine interaction with the ice. Two pieces of evidence point to diffusion as the principal fate of the chlorine radical. First, after irradiation of a sample of chlorobenzene adsorbed to an ice surface and subsequent thermal desorption of the system to 800 K, no chlorine compounds in the form of Cl (m/e=35), HCl (m/e=36), Cl_2 (m/e=71), or HOCl (m/e=52) were found to desorb *from the ice* in the Temperature Programmed Desorption (TPD) spectrum. An Auger spectrum taken immediately after thermal desorption to 800 K showed chlorine as the primary constituent on the nickel surface. Second, an XPS spectrum was taken of chlorobenzene adsorbed on ice before and at various time intervals after irradiation. Two chlorine 2p XPS signals were observed. It is believed that these two signals are consistent with a chlorine species on top of the ice (presumably in the form of chlorobenzene) during irradiation and a species below the ice (presumably in the form of atomic chlorine) on the nickel surface. This latter species was shown to be chlorine on the nickel by taking an XPS of the system after thermal desorption of the system to 800 K,

at which point chlorine remains on the surface. The XPS signatures are consistent with each other. It is believed by the author that chlorine, once photodissociated from the phenyl ring, does not recombine to a product but instead diffuses through the ice surface until removed from the diffusion process in the ice interior by chemisorption to the nickel surface.

The transport medium for chlorine to the nickel surface is not known. There are several possibilities. Atomic chlorine could for example diffuse through the ice structure by continuous complexation and decomplexation with H_2O monomers within the ice forming a weak H_2OCl complex intermediate in equilibrium with the individual monomers. This equilibrium process might allow chlorine to be transported through the ice medium to the nickel surface and may be somewhat analogous to a chromatographic separation. It might also be possible that the extensive hydrogen bonding network in solid H_2O at 90 K negates the orientational requirements for the above complexation, and the chlorine radical could diffuse through the ice unhindered as if the ice structure presented an inert hydrogen bonded cage, although even at 90 K, there is still expected to exist some form of van der Waals or hydrogen bonding interaction. Still another possibility is that the chlorine radical is combining molecularly to form, for example, HCl, HOCl, or Cl_2 and these compounds are diffusing through the ice undetected. Organo-chlorine compounds, i.e. methyl chloride, formed from photolytic destruction of the phenyl ring are also considered possible given the long irradiation periods (30 mins). If the diffusion is fast enough and the path length is short enough (< 50 Å) then the diffusion process could transport the chlorine containing compound to the nickel surface before being observed in the TPD.

The apparent lack of observation of these species desorbing from the ambient or on the surface could be due to nickel induced dissociation into chemisorbed chlorine and by-products once these chlorine containing compounds reach the nickel surface.

Chapter IV contains a brief description of the theoretical methods utilized in this volume. All theoretical investigations were performed with the aid of the *Gaussian 92* package of programs[27]. Theoretical calculations have been performed at the ab initio level of theory to investigate the interactions of hydrogen bonded and van der Waals systems with relevancy to molecular species investigated here. A discussion of the techniques and approximations in this chapter will provide useful information for a complete understanding of the theoretical results discussed in later chapters. A detailed description of the ab initio theoretical method with respect to the Hartree-Fock self consistent field approach is beyond the scope of this volume and is not given here. However, the reader is referred to several excellent literature sources on the subject[28,29]. However, a description of the parameters involved in the calculations such as basis set dependency and some of the more useful programs provided by *Gaussian 92* will be discussed here. Several physical observables can be calculated at the ab initio level. Calculations of these properties inherently have some approximations employed, and it is these approximations which need addressing. A discussion of the theoretical determination of binding energies, vibrational frequencies, intensity spectra, and thermodynamic quantities will be given here to provide some insight into the nature of these calculations.

Chapter V involves a discussion of the theoretical analysis of substituted benzenes and H_2O and the hydrogen bonding interactions between these compounds. Binding energies

have been determined for the interaction of benzene, chlorobenzene, and fluorobenzene with a single water molecule. It was found that the benzene-H_2O complex has the highest binding energy, with chlorobenzene and fluorobenzene having smaller but interestingly similar binding energies relative to the benzene-H_2O complex. This is surprising in light of the electrostatic properties of the individual molecules. Both chlorobenzene and H_2O have considerable dipole moments, and the dipole-dipole interaction could be considered as formidable. On the other hand, benzene has no dipole moment, and the dipole-induced dipole interaction inherent in the benzene-H_2O complex should be expected to be smaller than the dipole-dipole interactions of the two polar constituents. However, it was found that the interaction is not of the classical electrostatic nature, and π-hydrogen bonding dictates the interaction between the water molecule and the phenyl species, whether it is benzene, chlorobenzene, or fluorobenzene. The substituent on the phenyl ring was, however, found to have a pronounced effect on the binding location of the water molecule to the ring. The substituent is found to perturb the highly symmetric interaction experimentally observed for the benzene-H_2O system to a more asymmetric orientational interaction. Theoretical arguments are given to the possibility of two types of hydrogen bonding occurring within the same complex, namely a σ-type and a π-type hydrogen bond.

Vibrational information was also calculated for benzene, chlorobenzene and the complexes with H_2O. The vibrational spectra of chlorobenzene and benzene were theoretically determined using the harmonic approximation. Although the vibrational spectrum of the chlorobenzene-ice system was not experimentally determined, the information gathered from the calculations was useful and necessary in developing a full

description of the hydrogen bonding interaction between these compounds. A vibrational analysis is given here in terms of employing the normal modes of chlorobenzene and H_2O as a probe to the extent of hydrogen bonding occurring between the molecules. It was found that perturbations to the vibrational structure of chlorobenzene complexed with H_2O were minimal as was expected considering the stability of the conjugated ring and the weak hydrogen bonding interaction. However, useful information for characterization was obtained from the shifts in frequency and intensity upon complexation.

The last chapter, chapter VI, involves a discussion of the theoretically calculated interactions between a chlorine radical and a chlorine anion with a single water molecule. The information provided in this chapter gives some indication as to the differences in the interactions between an anion and a radical with a water molecule. A discussion of the possible, as of yet experimentally unobserved, complex formation between a chlorine radical and a water molecule is given along with a discussion of the complexes' relevance to possible diffusion mechanisms mentioned previously. The interaction between the two complexes follow the expected electrostatic predictions. The chlorine anion-water complex is shown to have a much higher binding energy than the chlorine radical-water complex. The chlorine anion complex has been studied previously by various groups and the interaction is consistent with what is determined by the author. The information gathered for the anion complex is used to complement the theoretically determined interactions observed for the radical complex. Also given is a brief description of the H_2O-chlorine cation (H_2OCl^+) which is believed to be a possible intermediate in the

reaction of chlorine nitrate and HCl on an ice surface. Vibrational frequencies for H_2OCl^+ are given and compared to recent experimentally determined values by Sodeau *et al*[18].

Chapter I

BACKGROUND

The phenomenon of ozone depletion within the polar stratospheric regions has prompted a considerable amount of research in the area of atmospheric chemistry. In the past decade or so, a number of research groups have attempted to define the mechanisms involved in ozone reduction. Although much information has been gathered as to the cause of the ozone loss, a complete theory involving detailed mechanistic pathways is still being debated. It is now confirmed that heterogeneous processes play a pivotal role in ozone depletion[4-6,30]. Micron size ice particles formed in the stratosphere above the polar regions during the winter vortex act as catalytic substrates on which atmospheric reservoir compounds are converted into photoactive species. The exact nature of these ice particles and the mechanisms by which they promote reactions are still under investigation.

Before discussing the ozone loss phenomenon specific to the Antarctic stratosphere, a brief and general description of the atmosphere will be discussed along with the characteristics of the ozone layer and its importance. The atmosphere is divided into regions based on the inherent thermal properties of each region. There are essentially four divisions: 1) troposphere, 2) stratosphere, 3) mesosphere, 4) thermosphere. The troposphere is the region closest to the surface of the earth. This region is responsible for the dynamic weather patterns as observed on the surface. These weather patterns are caused by pressure changes accompanying the continual motion of air parcels. This region displays a characteristic decrease in temperature with increasing altitude up to a height of

approximately 17 kilometers. One of the important properties of the troposphere is that it is mostly responsible for removing impurities that may migrate to the upper atmosphere. The tropospheric region is capped by an inversion point known as the tropopause where an inflection in the temperature gradient is observed.

At an altitude somewhat higher than the tropopause, the atmospheric temperature starts to increase steadily with increasing altitude. The region of increasing temperature is known as the stratosphere and exists roughly between 15 Km and 50 Km. The stratosphere displays primarily more lateral motion of airmasses than vertical churning characteristic of the troposphere and is responsible for the stratus layered clouds seen from the surface. The stratosphere has the important property of maintaining most of the ozone within its region. A thin sphere, sometimes referred to as the ozonesphere, exists in the lower stratosphere with a maximum in ozone concentration at approximately 15-25 Km[31]. The temperature of the stratosphere continues to increase with altitude to a maximum at 50 Km where the temperature of this region is approximately the same as the surface temperature. An inflection in the temperature gradient marks the stratopause and the beginning of the mesosphere. The mesosphere contains the coldest temperatures of the atmosphere. The last inflection point in the temperature gradient occurs at the mesopause and is followed by a monotonically increasing temperature ramp with increasing altitude. This region is known as the thermosphere. A complete schematic diagram of the thermal structure of the atmosphere is shown in figure 1-1.

The region of interest in this volume of work is the stratosphere. The stratosphere is divided into two divisions, the lower stratosphere and the upper stratosphere. The lower

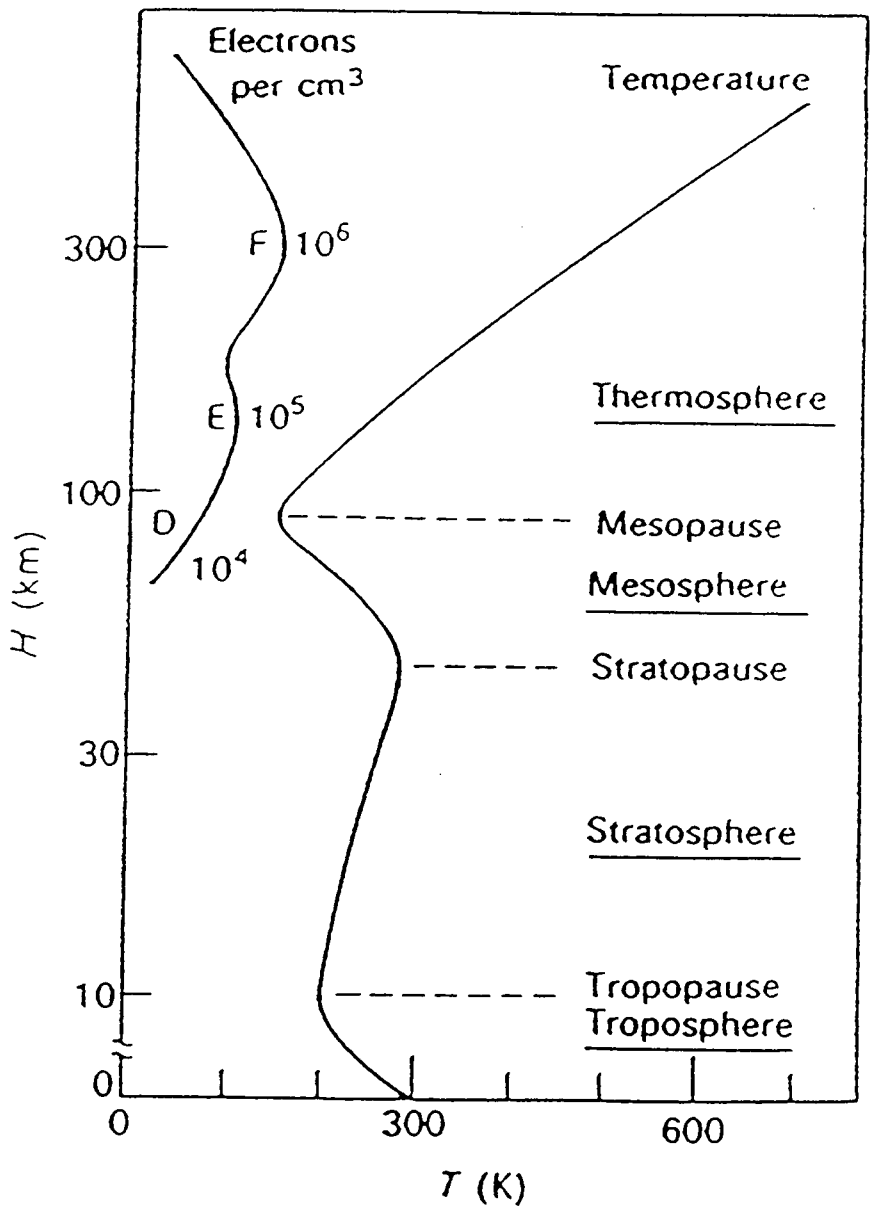

Figure 1-1. Schematic diagram of the thermal divisions of the atmosphere as a function of altitude in kilometers.

stratosphere, existing between 15 Km and 25 Km, contains, as mentioned previously, the bulk of the atmosphere's supply of ozone. Interestingly, ozone is the primary cause of the increase in temperature displayed by the stratospheric region. Ozone possesses a large absorption coefficient over a wide range of wavelengths in the near UV with a somewhat smaller absorption band in the visible. It absorbs most of the solar radiation between the wavelengths of 200 nm to 300 nm and is largely responsible for the removal of this biologically harmful radiation. Absorption by ozone in the near UV results in dissociation of ozone into O_2 and atomic oxygen. This dissociation eventually leads to a deposit of energy to the region in the form of heat due to collisions of the ozone fragments with neighboring species, i.e. N_2 and O_2. A recombination reaction of the form

$$(1.1) \quad O + O_2 \rightarrow O_3^*$$

$$(1.2) \quad O_3^* + M \rightarrow O_3 + M$$

gives the regeneration of ozone and completes the photochemical cycle.

The solar radiation incident on the earth's atmosphere shows a broad distribution of bands from < 100 nm to the far IR and beyond. Most of the intense bands are located at shorter wavelengths between 100 nm and 700 nm. The absorption of the shorter wavelengths of solar radiation are of primary importance to the biosphere and occur in essentially three regions of the atmosphere. Radiation bands below 100 nm and into the vacuum UV are absorbed at the high altitudes of the thermospheric region. This absorption of relatively high energy photons accounts for the monotonic increase in temperature with increasing altitude which is characteristic of this region. As previously mentioned, ozone is the primary absorbing species of radiation between 200 and 300 nm.

Solar radiation larger than 350 nm is incident on the surface of the earth and is either reflected or re-emitted back into the atmosphere. Figure 1-2 gives the incident flux of solar radiation to the atmosphere as a function of wavelength in microns.

Global ozone exists primarily in the lower stratosphere, but smaller concentrations are found in the upper stratosphere and throughout the troposphere as well. The amount of ozone in the atmosphere is measured in units called Dobson Units (DU). A Dobson unit is related to the physical thickness of the ozone layer if it could be brought down to the earth's surface. The global average ozone layer thickness is approximately 300 Dobson units[32], which equals approximately 1/8 of an inch. This is a relatively small concentration compared to other trace components of the lower atmosphere. However, the importance of ozone to the biosphere is undisputed and is exemplified in the research and attention that the ozone depletion phenomenon has drawn.

Ozone is continuously being destroyed and formed in the stratosphere through its photochemical cycle. However, any perturbations brought to the region allow unexpected destruction pathways to proliferate. There are a number of destructive pathways for ozone by highly reactive species. Ozone reacts readily with odd electron species such as Cl, Br, ClO, BrO, NO, and OH. Ozone is known to catalytically react with the halogen radicals with ClO and/or BrO acting as the catalytic carrier species[5]. Anthropogenic sources of chlorine and bromine are the primary cause of introduction of these halogens into the stratosphere. The only non-anthropogenic source would be CH_3Cl and CH_3Br from ocean evaporation cycles[33]. The average concentration of chlorine species before human intervention was approximately 1.6 ppbv[33]. The current concentration of these

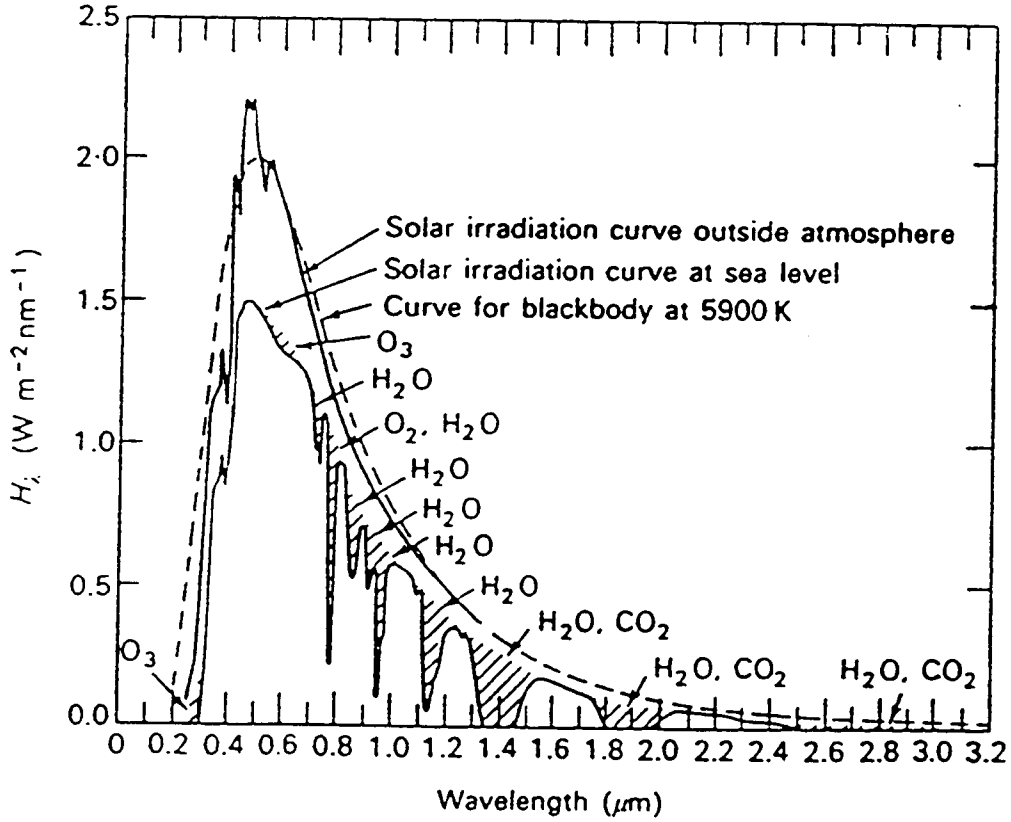

Figure 1-2. Diagram of solar radiation incident on the earth's atmosphere as a function of wavelength in microns. Radiation flux is given in units of W/m^2·nm. Absorption ranges for molecular atmospheric species are also shown.

species is approximately 2.7 ppbv and is expected to maximize its atmospheric presence in the late 1990's before declining[32]. The anthropogenic source of chlorine compounds, in the form of chlorofluorocarbons (CFC's), was suspected in the early seventies to introduce perturbations to the lower atmosphere. It was suggested in the early seventies by Molina and Roland[34] that CFC's released into the atmosphere could reduce the levels of ozone appreciably in the stratosphere.

CFC's are inert compounds that are used in industry as propellants, refrigerants, etc. They have three characteristics which make them susceptible to by-passing the safeguards of the troposphere and penetrate to the upper atmosphere. As previously mentioned, the troposphere is considered the safeguard against unwanted compounds in the upper atmosphere and acts to remove impurities by either of three methods: 1) solubility (rain), 2) chemical reactivity, 3) photolytic destruction. CFC's possess unusual characteristics which allow them to freely traverse the troposphere. First, CFC's are insoluble in aqueous solution thereby rendering rainfall useless in its impurity removal efficiency. Second, CFC's are highly chemically inert which is one their defining characteristics for commercial use. Third, CFC's are essentially transparent to wavelengths inherent in the troposphere.

The ozone destructive capability of these chlorine containing compounds becomes evident in the following photochemical cycle. When the CFC's are able to reach the *upper* stratosphere, the wavelengths inherent to that region are capable of rupturing bonds producing radical species such as shown in the following reaction

(1.3) $CF_2Cl_2 + h\nu \rightarrow Cl + CF_2Cl$

The chlorine radicals produced here can effectively destroy ozone in this region by the following catalytic reactions

(1.4) $2 \times (Cl + O_3 \rightarrow ClO + O_2)$

(1.5) $ClO + ClO + M \rightarrow Cl_2O_2 + M$

(1.6) $Cl_2O_2 + h\nu \rightarrow Cl + ClO_2$

(1.7) $ClO_2 + M \rightarrow Cl + O_2 + M$

Net: $2O_3 + h\nu \rightarrow 3O_2$

In this catalytic cycle[31], the rate limiting step is believed to be the reaction of ClO with itself to form the Cl_2O_2 dimer. This reaction scheme is highly dependent on the availability of reactive chlorine, in the form of Cl or ClO, within the region. However, at the altitude where bond rupturing radiation is available and appreciable amounts of Cl and ClO exist, ozone is not readily available, and is certainly not present in the amounts necessary for the large reduction observed in the Antarctic stratosphere. Hence there existed a glaring contradiction in the expected altitude for ozone reduction and the actual lower observed altitude where reduction in ozone was reported to occur.

At lower altitudes, these odd chlorine species, Cl and ClO exist in the inert nonphotoreactive forms of HCl and $ClONO_2$ at concentrations ~ 100 times larger than ClO[4]. These compounds are essentially transparent to the radiation available in the region of the lower stratosphere. Therefore, to account for the observed altitude of ozone reduction, it seems likely that these chlorine reservoir compounds are being converted into

more photoactive chlorine species thereby enabling them to reduce the ozone in the lower stratosphere. However, the mechanism for this conversion of inert forms of chlorine compounds into more reactive forms must be highly specific to temporal and latitudinal considerations of the Antarctic stratosphere.

The observation of the ozone "hole" over the southern polar region was first reported by Farman *et al.* in 1985[35]. Since 1957, stratospheric ozone measurements have been made continuously at the British Antarctic Survey stations located at Argentine Islands and Halley Bay. It was noticed in 1984, however, that a seasonal variation of ozone concentration was occurring. Ozone measurements taken in October were much lower than the values measured in March, yet this phenomenon was completely absent in the data measurements for years 1957-1973[35]. Recent measurements of the southern polar region in September and October of 1993 show a 50% reduction of the global average of 300 Dobson units with some areas repeatedly dropping below 120 Dobson units[32]. Farman *et al.* suggested that their observation of ozone depletion could be caused by increasing concentrations of CFC's in the region. Figure 1-3 shows the results obtained by Farman *et al* which indicates the ozone reduction at two different locations within Antarctica measured over time. Also shown is the total chlorine concentration in both the troposphere and stratosphere as a function of time. The correlation between a sharp rise in the chlorine content of the lower atmosphere and a sudden decrease in ozone is apparent and gave credence to the theory of ozone depletion by a halogen.

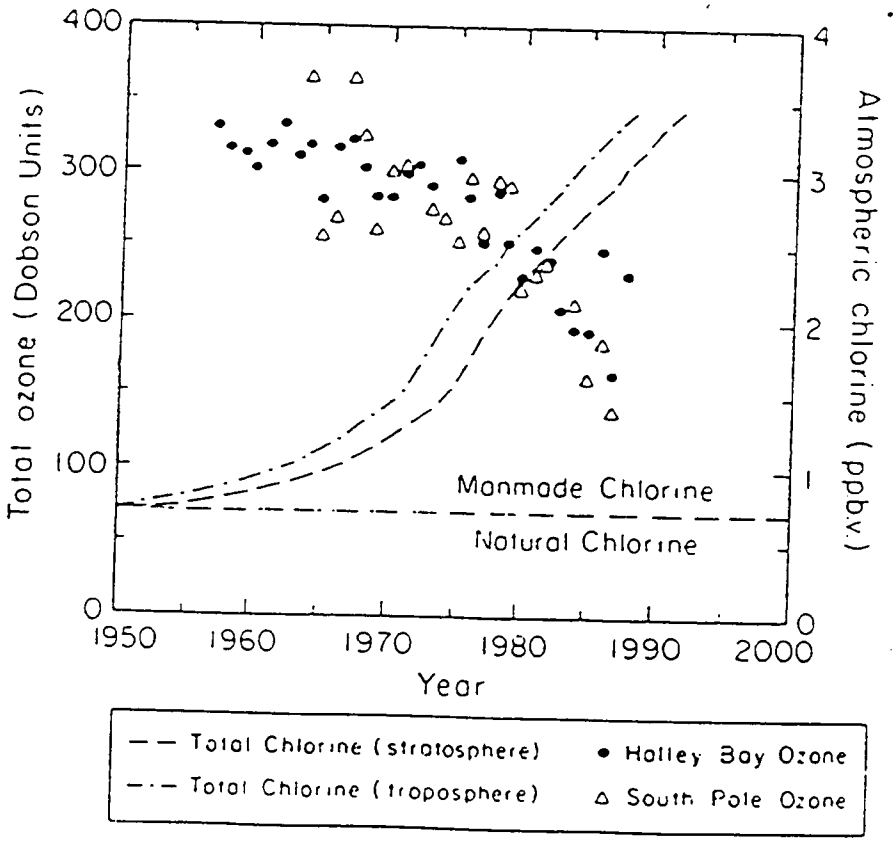

Figure 1-3. Total ozone observations above Halley Bay and the South Pole showing the development of the ozone hole. Total chlorine abundances in the troposphere and stratosphere are also indicated, based on an assumed 3.5 year lag time between the two atmospheric regimes. Natural chlorine abundances are believed to be ~ .6ppbv, with anthropogenic chlorine sources making up the remainder of the stratospheric chlorine budget. (graph is a reprint in Solomon's paper[31] of research contributed by Farman *et al.*)

It is now understood that the hole formation is seasonal. The hole appears approximately late August to early September (Antarctic spring) and continues to grow until roughly mid-October when the catalytic reduction comes to a halt. The atmospheric reactions that normally maintain the concentrations within the region eventually replenish the ozone.

Obviously, the southern polar region displays unusual circumstances involving ozone depletion. The geographic location and the existing conditions of the area are key contributors to the unusual circumstances involving ozone depletion. Winter in the southern hemisphere occurs from late June to early September. During this time, the southern polar stratosphere experiences the coldest temperatures in the stratosphere and is 10-15 K colder than the northern polar region for similar time periods[31]. These conditions result in what is termed the polar vortex. The polar vortex is a mass of cold air in a circumpolar flow around the Antarctic continent which remains essentially isolated from the lower latitudes. The speed of the winds existing around the polar vortex can reach on the order of tens of meters per second effectively allowing air masses to circumnavigate the continent in a matter of weeks. These volatile weather patterns give an indication of the dynamics of the system existing within the vortex. The vortex does however remain isolated from the lower latitudes of the southern hemisphere.

The conditions prevalent in the Antarctic winter are ideal for production of aerosols within the Antarctic stratosphere. These aerosols are referred to as Polar Stratospheric Clouds (PSC's). PSC's are classified into two distinct groups known as type I and type II. Type I PSC's are considered a composite of compounds in an ice matrix which is primarily

composed of nitric acid in the form of nitric acid trihydrate or NAT. Type I PSC's are expected to form at temperatures less than 195K[30,36]. Type II PSC's consist solely of water-ice particles and are expected to condense at lower temperatures than type I PSC's[37]. Type I PSC's are much more abundant than type II PSC's and are considered by some authors to play a more important role, however there exists debate over this subject[38].

PSC formation is suspected to be the key contributor to the seasonal variation in ozone reduction observed in the Antarctic stratosphere by acting as catalytic sites for conversion of unreactive chlorine reservoir compounds to photoreactive chlorine species. The reaction speculated to most likely contribute to the conversion is

$$(1.8)\quad HCl + ClONO_2 \rightarrow Cl_2 + HNO_3$$

This reaction has been studied extensively on ice surfaces and is known to react slowly in the gas phase[39,30,40]. Molina *et al.*[41] reported an upper limit rate constant (k) to reaction 1.8 in the gas phase of 10^{-19} cm^3 $molecules^{-1}$ sec^{-1}. There are uncertainties as to whether reaction 1.8 occurs solo on the ice surface or in a mechanistic pathway. Reaction 1.8 is believed by some investigators to proceed via two steps:

$$(1.9)\quad ClONO_2 + H_2O \rightarrow HOCl + HNO_3$$

$$(1.10)\quad HCl + HOCl \rightarrow Cl_2 + H_2O$$

Like reaction 1.8, the hydrolysis of chlorine nitrate, reaction 1.9, is not considered to react appreciably in the gas phase. The reaction between water and chlorine nitrate in the gas phase has been found to have a rate constant (k) less than 2.0×10^{-21}

cm^3/molecule·sec[18]. However, heterogeneous processes on ice surfaces allow reaction 1.9 to proceed quite rapidly producing nitric acid which is incorporated into the bulk of the ice and hypochlorous acid which subsequently reacts with HCl to produce chlorine gas. However, it has been suggested that reaction 8 can occur independently of reaction 1.9 and 1.10 and still account for the observable rates of active chlorine species being produced.[42]

The above reaction scenarios greatly depend on the uptake and molecular form of HCl on ice particulates. If the above reactions are responsible for producing the large amounts of photoreactive chlorine species in a brief period of time, then HCl must have an appreciable residence time on the ice surface. It has been suggested that the necessary requirement for reaction 1.8 (and reactions 1.9, 1.10) to occur is that appreciable amounts of HCl reside on the surface of the ice prior to co-reactant adsorption[43]. The partial pressure of HCl in the Antarctic stratosphere is approximately 10^{-7} to 10^{-8} torr or 10^{10} to 10^9 molecules/cm^3 respectively[44]. Extensive studies of adsorption and absorption of HCl by ice surfaces have been performed previously[45-48,15,7,14]. It has been shown that HCl uptake occurs rapidly on pure water ice particulates (type II PSC). However, the amount of HCl uptake depends on the components of the ice. For NAT ice, Hanson *et al.*[46] have reported a small decrease in the HCl uptake relative to HCl uptake by pure ice. They reported saturation coverages of 2-3 x 10^{14} molecules cm^{-2} and 5 x 10^{14} molecules cm^{-2} for NAT and pure ice respectively. However, they also indicated that the time constant for HCl uptake on both surfaces were roughly similar. Leu *et al.*[14]. find somewhat similar results. They report a saturation coverage of HCl on both ice and NAT to be 2 x 10^{13}

molecules cm^{-2}. However, they indicate that the available surface area for ice is an order of magnitude greater than the surface area of NAT with values of 10^{-7} cm^2/cm^3 and 10^{-8} cm^2/cm^3 respectively. They further report concentrations of HCl within or on ice particulates to be 2×10^6 molecules cm^{-3} and 2×10^5 molecules cm^{-3} for ice and NAT respectively. There does appear to be agreement that increasing adsorbate uptake as well as increasing reaction probabilities are observed with increasing water content in the ice particulates of the polar stratosphere. Also, HCl uptake by an ice surface shows a dependency on the dimensions of the ice. Increasing thickness of ice allows for increased surface area for adsorption due to extra surface area created within the pores and cracks of the ice structure. Hanson *et al.*[46] noticed an increase in HCl uptake with increasing thickness of ice (3 μm to 30 μm) by a factor of 2. Leu *et al.*[14] reported an HCl uptake increase of a factor of 5 in going from an ice thickness of .5 μm to 15.7 μm.

The possibility of ice induced decomposition and/or conversion of HCl to hydrated forms is still being debated. Upon adsorption of HCl to an ice surface, HCl could conceivably be incorporated into the surface as hydrated H^+ and Cl^- ions. However, there are discrepancies in the literature as to the *extent* of dissociation of HCl on ice. For instance Hanson *et al.*[46] argue that the incorporation of HCl in the ice as dissociated HCl is quite small. They indicate that the adsorption of HCl is predominantly reversible. However, they do show evidence for partial reduction of molecular HCl, but at a rate that is significantly smaller than the HCl uptake rate. Roberts *et al.*[15] also report molecularly adsorbed HCl on an ice surface. On the other hand, Devlin *et al.*[48] and Banham *et al.*[45] indicate that dissociation of HCl on ice readily occurs. Banham *et al.* report that HCl at

low coverages exists within the ice surface as a hexahydrate consistent with the following reaction

$$(1.11) \quad HCl + 6H_2O \rightarrow H_9O_4^+Cl^-2H_2O$$

A hexahydrate phase is then considered to be the predominant feature of the ice surface. They also indicate that upon increasing HCl concentration, lower hydrates can be formed but these are restricted to the surface region above the hexahydrate phase. Both Banham and Devlin report vibrational evidence to support the more likely proposition of dissociated HCl incorporation within an ice surface at temperatures relevant to stratospheric ice (180 K to 200 K).

The other chlorine reservoir compound, chlorine nitrate, is known to readily adsorb to ice surfaces with appreciable residence times. Hydrolysis of chlorine nitrate is expected to produce HOCl and nitric acid in accord with reaction 1.9. As mentioned previously, there are two mechanistic possibilities: reaction 1.8 and reaction 1.9 may occur independently of each other, or as suggested by some investigators, reaction 1.8 may proceed via reaction 1.9 and 1.10. However, most authors investigating mechanistic pathways for reactions 1.8-1.10 make the *reasonable* assumption that HCl is dissociated into hydrated ions upon introduction to the ice surface. Both mechanistic possibilities involve conversion of Chlorine nitrate and HCl to photoactive chlorine species. A discussion of the two possible mechanistic pathways are given below.

The first possible mechanism involves the reaction between molecular chlorine nitrate and hydrated chlorine anions incorporated in the ice surface. Haas *et al.*[8] have proposed the following reaction as occurring on the ice surface.

(1.12) $Cl^- + ClONO_2 \rightarrow [Cl\text{---}Cl\text{---}ONO_2^-] \rightarrow Cl_2 + ONO_2^-$

This reaction involves a nucleophilic attack by the chlorine anion to the positive end of chlorine nitrate (the chlorine in chlorine nitrate has been shown to have an appreciable positive charge character) to produce molecular chlorine gas which desorbs into the ambient and the nitrate anion which is incorporated into the bulk ice.

The second possible mechanism involves hydrolysis of chlorine nitrate on the ice surface, reaction 1.9, as the limiting step. Reaction 9 is thought to proceed by the following mechanism

(1.13) $ClONO_2 + H_2O \rightarrow [H_2OCl^+\text{---}NO_3^-] \rightarrow HOCl + HNO_3$

The H_2OCl^+ as a possible intermediate to the above reaction was first reported by Sodeau *et al.*[18]. They performed ionization experiments of chlorine nitrate on an ice surface under ultra-high vacuum. They reported vibrational frequencies that they believe were indicative of H_2OCl^+ formation on an ice surface. Upon formation of the intermediate, the reaction proceeds to produce HOCl and dissolved nitric acid in the form of the hydronium cation and nitrate anion. HOCl is considered the only stratospherically important species that does not hydrolyze on the ice surface. At this point, HOCl could conceivably enter the gas phase where it can be photolyzed into OH and Cl radicals, or it can react with ambient HCl to produce H_2O and Cl_2. HCl and HOCl are known to interact exothermically in the gas phase. The more likely fate of HOCl, however, is reaction on the surface of the ice with either molecular HCl or more likely hydrated chlorine anions to produce Cl_2 and H_2O or OH^- respectively. However, the sticking probability of HOCl reportedly has a large temperature dependency with increasing sticking probability with decreasing

temperature.[42] Therefore, the fate of HOCl would depend strongly on the existing enviromental conditions of the PSC's.

Both reaction mechanisms are plausible and more likely compete with each other on the ice surface. However, a very recent investigation by Oppliger *et al.*[42] indicates that the direct reaction between HCl and chlorine nitrate (reaction 1.8) is the more likely mechanism for production of photoactive Cl_2. They investigated both mechanisms under varying reactant concentrations and temperatures and argue that the direct reaction between chlorine nitrate and HCl is considerably faster than the rate of formation of HOCl by hydrolysis of chlorine nitrate. However they did report HOCl formation rates that seemed to corroborate Sodeau[18] *et al.*'s proposal of an HOCl precursor intermediate. Opplinger *et al.*[42] reported a fast hydrolysis rate for chlorine nitrate, but a considerable time lag was observed for the production of HOCl indicating a possible stable reaction intermediate that released HOCl at a slower rate than the rate of chlorine nitrate hydrolysis.

The proposed mechanism for formation of photoactive chlorine compounds on ice particulates must account for the observed loss rate of ozone depletion ~ 4-5 weeks. As previously mentioned, both reaction 1.8 and 1.9 proceed extremely slow in the gas phase ($< 10^{-19}$ cm^3 $molecules^{-1}$ sec^{-1}). The fast time period of ozone depletion and the ambient concentration of reactants suggests that the rate of conversion of the reservoir chlorine compounds to photoactive chlorine compounds is considerably fast (Solomon *et al.*[4] suggest a rate on the order of 2×10^{-14} cm^3 sec^{-1}). Leu *et al.*[14] suggested that based on their laboratory reaction probability results, the conversion of reservoir inactive chlorine

compounds to active chlorine compounds occurs within a day for reaction 1.8 and within a week for a reaction scheme consistent with reaction 1.9 and 1.10. Similar reaction probabilities were found by Hanson *et al.*[46] and Abbatt *et al.*[49] indicating very short time scales for conversion of the chlorine reservoir compounds.

More experimental investigations are still required for a complete understanding of the mechanisms involved in ozone depletion within the Antarctic stratosphere. Particularly, the dynamics of PSC condensation and evaporation and how PSC sedimentation effects the above reaction scenarios. PSC's have a high turnover rate with reported lifetimes on the order of a couple of days[50]. Also size distribution and impurity concentrations of PSCs need to be addressed for a complete description of the phenomenon.

Chapter II

EXPERIMENTAL PROCEDURES

The experimental techniques utilized within this volume are consistent with standard ultra-high vacuum methods. The vacuum generator consisted of a cylindrical stainless steel vacuum chamber (volume ~ 50L) which was self designed to house several investigative techniques at various ports to the chamber. The chamber was evacuated by a turbo pump with an average pumping speed of approximately 170 L/s for sputtering gases and backed by a rotary pump for initial rough vacuums. A titanium sublimator was also used in conjunction with the turbo pump to achieve a higher vacuum. The manipulator arm, upon which the crystal substrate was mounted, could be filled with liquid nitrogen (LN). The LN served two objectives. First, it allowed for low temperature studies (90 K) of the sample through thermal contact with the manipulator arm. Second, the cold manipulator arm made feasible the uptake of ambient gases through adsorption to the arm resulting in an increased vacuum. The apparatus routinely achieved pressures on the order of 2 $x10^{-10}$ torr measured by an ionization gauge housed at the upper portion of the vacuum chamber.

The vacuum chamber was equipped with a double pass cylindrical mirror analyzer for Auger electron spectroscopy (AES) and x-ray photoelectron (XPS) measurements and a multiplexed quadrupole mass spectrometer for thermal desorption spectroscopy (TDS). A magnesium anode was used for the XPS measurements. Nickel surface cleanliness was

achieved by neon ion sputtering followed by annealing to restore crystallographic order and was monitored by AES.

A circular nickel crystal cut to the (111) plane was mounted to the manipulator arm inside the chamber and used as the substrate for ice film growth. The crystal was approximately 1 cm in diameter and on the order of 1mm in thickness. Heating elements in the form of two tungsten wires were attached along the edges of the crystal. Resistive heating through these tungsten wires allowed the crystal to be routinely heated to 1000 K for cleaning, annealing, and desorption purposes. The lowest temperatures achieved by thermal contact of the nickel crystal to the LN filled manipulator arm was approximately 90 K. The temperature of the crystal was measured with a chromel-constantan (Type E) thermocouple spot welded to the back of the crystal.

At ultra-high vacuum, the primary background gases were H_2, CO, and CO_2. After repeated dosing of the nickel crystal with H_2O, water vapor also became an increasing component of the background pressure. Prior to each experimental day, a background mass spectrum was taken of the ambient and of the material to be studied.

Chlorobenzene (Aldrich), d_5-chlorobenzene (Cambridge Isotope) and H_2O (99.9% purity spectrometric grade) were purified prior to an experiment by repeated freeze-pump-thaw cycles, and the purity was monitored by mass spectroscopy. The gases were introduced to the crystal via directed dosers. The exposure for chlorobenzene and d_5-chlorobenzene was achieved from a differentially pumped reservoir and monitored in units of torr·sec (torr refers to line pressure). Monolayer coverages of chlorobenzene on the ice were determined from the onset of the condensed phase desorption peak. Precise

monolayer coverages were not determined, and only approximate submonolayer and multilayer coverages were investigated.

Thin ice films were deposited on a nickel (111) crystal at T~ 90 K. Dosing occurred via directed dosing with the nickel crystal facing the doser at a distance of approximately 1-3 mm. The doser was designed to allow for uniform coverage across the substrate. A cylinder filled with distilled water at -5° C (vapor pressure ~ 4 torr[51]) was used as the H_2O dosing source. Various H_2O coverages were achieved by controlling the flow time of the H_2O vapor through a Knudsen type orifice (dia=15 μm) at the above vapor pressure. The dosing time required to achieve a monolayer coverage was taken at the onset of the multilayer peak. The ratio of the multilayer to monolayer thermal desorption peak area was used to obtain a rough estimate of multilayer coverages of ice. The average multilayer coverage of ice for all adsorbate trials was approximately ~18 ML.

Thermal desorption spectroscopy, which will be described later in this section, was used to determine parent species and photoproducts desorbing from the surface. The crystal was aligned directly in front of the ionizing grid at a distance of approximately 1 cm. The substrate temperature was ramped at 5 K/s from 90 K to 800 K while the intensity of selected masses was monitored as a function of temperature. Ionization was achieved by electron impact at an ionizing voltage of 70 eV or 20 eV. The sample was biased at -70 volts to reduce electron stimulated desorption or reaction. XPS core level energies in this report are calibrated with respect to the nickel 2p and nickel 3p binding energy for a clean nickel surface. All systems were studied with an experimental xps resolution of ~ 1.5 eV with MgKα radiation.

The UV source used in this study was a 200 W HgXe arc lamp (Oriel), which generates photons with a broad distribution from 250 nm to 900 nm. The most intense photons generated in the UV region were centered around 254 nm (5 eV). The photons were directed through a sapphire window onto the crystal at an angle normal to the surface plane. No filters were used with the source. The nickel crystal experienced an increase in temperature of ~ 11 K during irradiation and never surpassed 101 K during the experiments reported here.

A brief description of the UHV techniques used in this volume will be discussed here to familiarize the reader with the processes involved in these methods. The first and probably the most applied surface tool is Auger electron spectroscopy (AES). Auger spectroscopy offers the advantage of being specifically a surface technique, and as a result, this method is primarily used for qualitative determination of adsorbates on the surface. It is used in this volume mostly as a method for determination of the cleanliness of the nickel surface after desorption and annealing processes. The theory of Auger spectroscopy is as follows. AES is considered a two-electron process. The first step is the removal of a core electron of energy E_{core} within an atom of the surface of interest and the generation of an excited atomic species, S^+. This core ionization can be achieved by irradiating the sample with X-rays or by bombarding the surface with electrons of comparable energy. For the experimental work in this volume, electrons with kinetic energies of 3000 eV were focused onto a small area of the sample surface. However, the overall Auger process is such that monochromatic radiation or electrons is not necessary. Once the excited atom is formed by removal of a core electron, another electron at energy E^*_{core} in a higher orbital

drops down to fill the vacancy left by the ejected electron. The energy gained when the second electron drops to the vacant orbital is deposited to a third electron, known as the Auger electron, which is subsequently ejected from the surface with a kinetic energy that is approximately equal to the energy difference of E_{core} - E^{*}_{core} inclusive of relaxation effects and work function energetics. However, as stated above, the Auger electron is independent of the energy of the initial ionization source.

The Auger electrons produced in the above description are highly characteristic of the atomic species from which they were ejected. The above transitions are given special nomenclature. For example, KLL is an abbreviation for the process involving an initial ejection of an electron from the K shell followed by a relaxation of an electron from the L_1 shell with subsequent ejection of the Auger electron from L_{11}. For the experimental work in this volume, the nickel (111) crystal is the substrate of interest. Two prominent Auger transitions are of interest. One occurs at an Auger electron energy of ~ 64 eV and represents the KLL transition of nickel. The other occurs at ~ 848 eV and is considered the MNN transition. The molecular adsorbates of interest in this volume also produce Auger peaks that are characteristic of the atomic components of the adsorbate. The chlorine KLL process occurs at an Auger electron energy of ~ 180 eV. The KLL transitions for carbon and oxygen occur at approximately ~ 260 eV and ~ 510 eV respectively.

Auger spectroscopy offers two distinct advantages as a surface tool. The first lies in the penetration power of the Auger electrons. Auger electrons, once formed, typically

have escape energies from 25 eV to as high as 1000 eV. However, the low energy nature of these electrons implies that only electrons from the first couple of layers of the surface can escape even though Auger electrons may be formed deeper in the bulk. The electrons that do escape are highly characteristic of the surface composition. The second advantage lies in the spatial resolution of the individual Auger signals. Derivatives of the counting rate of electrons are taken to maximize and distinguish characteristic Auger peaks. The signals produced are readily resolved thereby allowing for easy qualitative determination of the peaks. Differentiation also facilitates determination and separation of individual Auger peaks from background interference. Although Auger spectroscopy is very useful for qualitative determination of surface composition, it has less application as a quantitative surface tool.

Probably the most useful method for studying reactions on surfaces from a qualitative and quantitative sense is thermal desorption spectroscopy (TDS) or, as it is sometimes referred to, temperature programmed desorption spectroscopy (TPD). For the experimental work in this volume, thermal desorption spectra were taken by utilizing a quadrupole mass spectrometer mounted through a portal inside the vacuum chamber. Thermal desorption spectra are taken by mass to charge filtering of different compounds desorbing from the sample surface as a function of temperature. All adsorbates desorbing from the crystal generally have desorption temperatures characteristic of the species. For example, in our experimental setup, a submonolayer coverage of H_2O on Ni (111) has a characteristic desorption temperature of approximately 160 K.

Thermal desorption spectroscopy has the advantage of not only qualitatively determining the desorbing species (based on characteristic desorption temperature), but it also has the advantage of quantitatively determining relative coverages of the adsorbate on the substrate. As mentioned above, H_2O at submonolayer coverages on Ni (111) has a distinct desorption temperature. However, as the exposure of H_2O on Ni (111) is increased, new desorption temperatures indicative of the coverage is observed. Monolayer and multilayer coverages of a compound usually have distinct desorption temperatures with monolayer coverage *usually* having the higher desorption temperature. Once the first monolayer coverage has been achieved, increased exposure results in multilayer coverages by adsorption to the top of the first monolayer. The distinct desorption temperatures for these two coverages arise because of the binding differences indicative of the chemical environment. For the monolayer coverage, the H_2O is bound directly to the nickel with a characteristic binding energy (adsorption energy). The second and higher layers are indicative of H_2O bound to the first H_2O monolayer with a somewhat smaller binding energy, hence the lower desorption temperature.

The number and position of desorption peaks of a particular adsorbed species is also dependent on the rate of temperature increase of the sample. Better resolution of peaks can be achieved with a smaller temperature ramp, i.e. 2 K/sec. At smaller temperature ramps, it is possible to observe what are termed transition coverages. For example, at a substrate temperature increase of 5 K/sec, two desorption peaks are observed for greater than monolayer exposures of H_2O to nickel corresponding to multilayer and monolayer coverages. However, if the temperature ramp is reduced to 2 K/sec, then it is possible to

observe the second and to a lesser extent the third monolayers of coverage. The second and third monolayer coverages are in effect transitions between monolayer water coverage and bulk multilayer ice coverage. They both possess binding energies indicative of the chemical environment that are intermediate between the two extremes. All exposures greater than three monolayers have effectively similar binding energies and to an extent is independent of the underlying crystal substrate. These multilayer coverages generally have desorption energies (binding energies) characteristic of the bulk phase of the material.

Gas phase adsorption to a solid generally will always be exothermic with an energy deposit to the surface from the loss of translational degrees of freedom of the adsorbate. Alternatively, desorption is an endothermic process with a subsequent loss of energy at the surface. Desorption of particular adsorbates sometimes follows zeroth order kinetics. Zeroth order kinetics is sometimes used in TDS to determine enthalpies of desorption, ΔH_{des}. A particular method known as leading edge analysis is useful in determining desorption enthalpies. In accord with zeroth order kinetics, the enthalpy of desorption can be approximated by the energy of activation for desorption assuming of course that no barrier exists for adsorption. The data points for the leading edge of a desorption peak is taken as the zeroth order rate of desorption. The activation energy (and consequently the enthalpy of desorption) is taken as the slope of the desorption rate versus the inverse temperature. This is somewhat similar to an Arrhenius plot. The activation energy gives a description of the chemical environment of a particular compound and gives an indication of the binding interactions. For example, leading edge analysis of the multilayer

desorption peak of H_2O shows a similar energy value to the bulk phase enthalpy of sublimation for pure ice (50 KJ/mol)[52] as expected for multilayer coverages.

X-ray photoelectron spectroscopy (XPS) is the last technique to be studied here. The XPS process is similar to processes involved with Auger spectroscopy. Like Auger spectroscopy, core ionization of a particular surface species can be achieved by focusing higher energy x-ray radiation onto the surface in question. Core electrons from a specific atom are ejected and the kinetic energy of the ejected electrons is measured. Determination of the kinetic energies (KE) lead to determination of core binding energies which is strongly characteristic of the particular atomic species. Binding energies (BE) are determined by the following equation (relaxation effects not included)

$$(2.1) \quad BE = h\nu - KE$$

Also, the core ionization by XPS is highly indicative of surface atoms of a bulk sample for similar reasons as discussed for AES. However, unlike AES, the XPS process does depend on incident energy.

Ionization of core electrons by XPS give excellent signatures of a particular atoms within a multi-atom sample due to the substantial independence of core electrons of the molecular environment. However, XPS is not entirely insensitive to the molecular environment and has found application in determining chemically inequivalent atoms due to slight but detectable shifts in the binding energies of core electrons. These shifts are a result of small perturbations to the core orbital energies brought on by the electronic environment. For example, the 2p XPS peak for gas phase atomic chlorine (actually $2p_{1/2}$ and $2p_{3/2}$; splitting factor of ~ 1.6 eV)[53] has a binding energy of approximately 200.8 eV.

However, the exact value depends on the environment of the chlorine species. Values to be given in chapter III will indicate two different binding energies for the chlorine 2p core electron depending on whether it ionizes from chlorine as chlorobenzene on the ice or as chlorine chemisorbed to the nickel surface. Considerable electron density surrounding the chemisorbed chlorine would be expected for chlorine on the surface relative to chlorine on the ice surface. As such, the higher electron density at the nickel surface for chlorine environment should lower the core ionization energies for chlorine. This is indeed the case with nickel bound chlorine having a maximum in the 2p XPS peak at ~ 2.4 eV lower in energy relative to the chlorobenzene bound chlorine on the ice surface.

Chapter III

EXPERIMENTAL RESULTS

Heterogeneous processes in the lower atmosphere may play an important role in governing the reaction mechanisms of highly reactive odd electron species such as Cl and ClO that are produced in minute concentrations in the stratosphere upon photolytic decomposition of volatile chlorine containing compounds. Chlorine radicals, regardless of their origins, have been implicated as major contributors to ozone depletion in stratospheric polar regions. For this reason, we undertook an investigation of the photochemistry of chlorobenzene adsorbed to an ice surface in order to probe not only interactions between atomic chlorine and ice but also to explore the interface interactions between organochlorine compounds with ice surfaces.

While chlorobenzene is not considered to be an atmospheric problem, it does possess properties that may lend itself experimentally useful for probing organochlorine-ice interactions. Photolysis of gas phase chlorobenzene has been well documented,[54-56] and it is known to homolytically photodissociate upon irradiation in the UV, producing atomic chlorine and phenyl radicals

$$(3.1)\quad PhCl + h\nu \rightarrow Cl\cdot + Ph\cdot$$

which ultimately form benzene and HCl[56]. In aqueous media however, chlorobenzene forms phenol and HCl during UV irradiation from intermediates that are considered more zwitterionic than homolytic due to solvation effects of the transition state[57].

We present here our study of UV photolysis of chlorobenzene adsorbed on thin ice films under ultra-high vacuum conditions. Our goal was to investigate the bonding characteristics and photochemistry of chlorobenzene and ice at the interface and to ascertain the photolysis products of chlorobenzene adsorbed on an ice surface. Specifically, we are interested in the interactions between chlorine radicals and the ice film and whether or not abstraction of a hydrogen from water to form HCl is feasible. We use analysis of photoproducts by mass spectrometry to investigate the role of the ice surface in directing photochemical or photophysical processes exhibited by the excited chlorobenzene.

The evidence given here indicates that the ice films are essentially inert toward chemical reactivity with the adsorbate. Photolysis of chlorobenzene adsorbed in submonolayer coverages to the surface of thin ice films gives benzene as the sole photoproduct observed in the desorption data. Furthermore, isotopic studies with d_5-chlorobenzene under similar conditions show that the hydrogen source to form benzene is primarily another chlorobenzene molecule. This is similar to gas phase photochemistry of chlorobenzene indicating little chemical interaction with the ice surface at temperatures between 90 and 101 K. Also, the chlorine radical, once formed, apparently does not interact chemically with the H_2O but diffuses rapidly through the ice to the nickel surface where it remains chemisorbed. No chlorine containing species is seen to desorb during the

thermal desorption studies except the parent chlorobenzene. Our XPS studies indicate that chlorine is transported to the nickel surface while the ice is still intact. The nature of the transporting species has not been ascertained, but the lack of desorbing molecular chlorine species (HCl, Cl_2) suggests that atomic chlorine may be the likely candidate. We give some estimate of the kinetics of diffusion for transport of chlorine to the nickel surface.

RESULTS

H_2O/Ni(111). Deposition of chemisorbed water on nickel surfaces has been well documented[58-60]. The thermal desorption spectrum as a function of H_2O coverage is shown in Fig. 3-1. Two desorption peaks are distinguishable at 173 K and 168 K. These are considered monolayer and multilayer adsorbed H_2O respectively. The multilayer peak continues to grow with increasing exposure until the monolayer peak is concealed underneath giving a single multilayer desorption peak at ~ 170 K. Ice films deposited at temperature <100 K are considered amorphous[61]. We did attempt to compare the photolysis in terms of desorption photoproducts between chlorobenzene adsorbed on amorphous and annealed ice. Annealed ice was formed by increasing substrate temperature to 150 K and subsequent cooling. Our investigations showed little difference in the photochemistry of chlorobenzene adsorbed on annealed and amorphous ice, and as a consequence, amorphous ice was the primary ice structure used in these experiments.

The integrity of the ice films were evaluated by investigating various adsorbates on the ice surface. Methanethiol was dosed to the surface of the ice to identify access channels

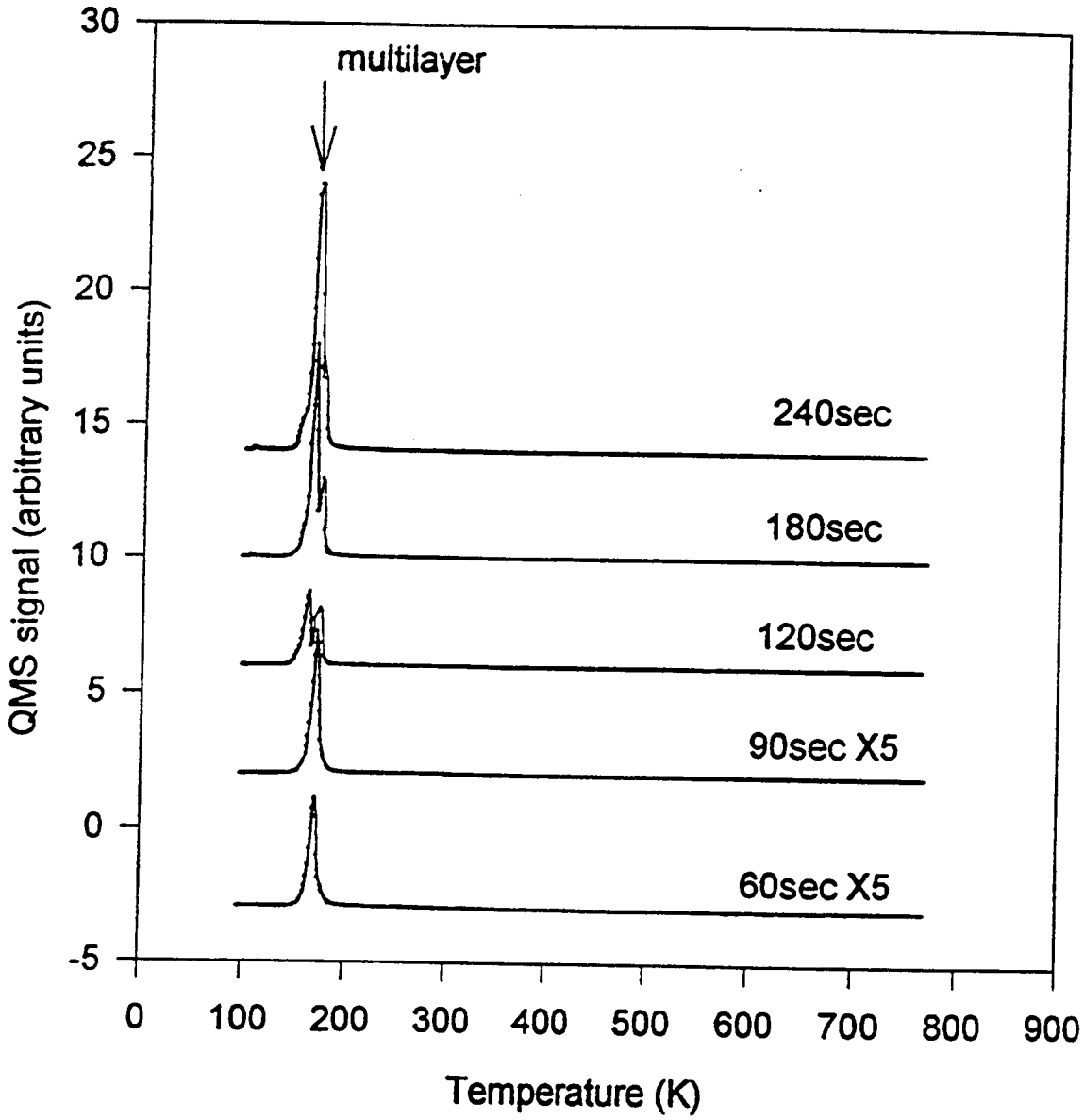

Figure 3-1. Thermal desorption spectrum of H_2O (m/e=18) adsorbed to Ni(111) for various coverages. H_2O was dosed for all coverages at T<100 K. Desorption peaks at 168 K and 173 K are assigned as multilayer and monolayer desorption species respectively. The temperature ramp is 5 K/s.

to the nickel surface. Methanethiol, upon adsorption on nickel, will leave sulfur as a thermal desorption product. Auger analysis identified no sulfur on the nickel after heating the substrate to 800 K. Chlorobenzene will also thermally dissociate upon access to the nickel surface leaving behind atomic chlorine. Again no access pathways for the adsorbate to reach the nickel substrate were observed. We conclude that the ice films were continuous and that we were indeed investigating ice surface chemistry.

UV radiation damage to the ice film was considered negligible. The nickel substrate did however undergo a temperature increase from irradiation, but the total change in the substrate temperature was approximately 11 K. The temperature for all irradiation trials never exceeded 101 K. The temperature increase from photolysis is not sufficient to adversely affect the morphology of the ice films. Integrated thermal desorption peak areas of H_2O from the nickel after 30 min UV irradiation indicated no noticeable loss of H_2O during the photolysis. For submonolayer exposures of chlorobenzene on the ice surface, no evidence was found for chlorobenzene access to the nickel upon irradiation, indicating little morphological change within the ice.

Chlorobenzene/Ni(111). It is necessary to describe the chemistry of chlorobenzene directly adsorbed on the nickel surface in order to provide comparative information for the chlorobenzene/ice system and to further distinguish the two. Fig. 3-2 shows the thermal desorption spectrum of chlorobenzene adsorbed on Ni(111). The Auger spectrum (fig.3-2 inset) shows that surface induced decomposition occurs for submonolayer coverages of chlorobenzene adsorbed to Ni(111). Carbon-chlorine bond scission generates chemisorbed chlorine to the nickel and a phenyl group. The benzene is

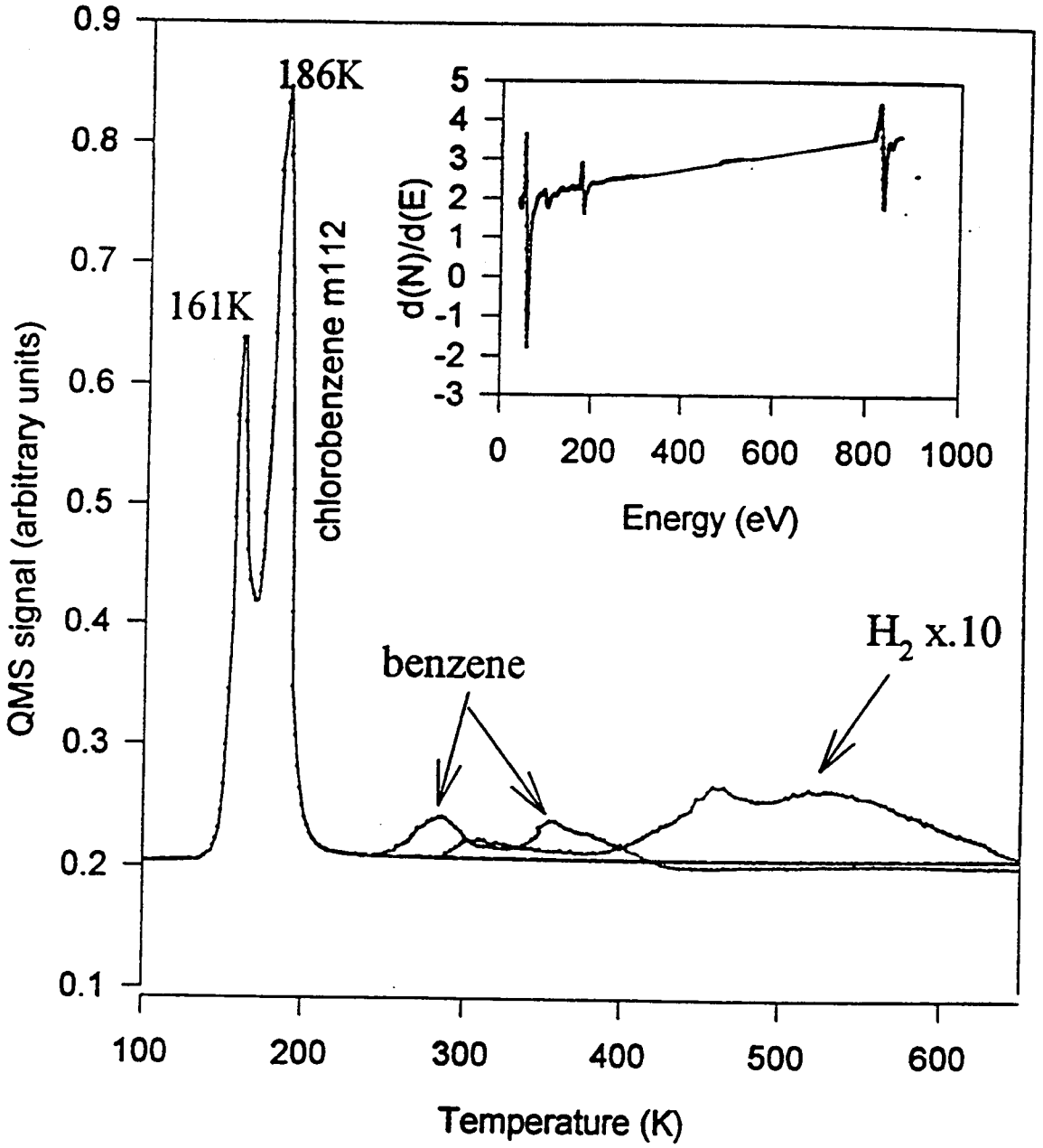

Figure 3-2. Thermal desorption spectrum of chlorobenzene (m/e=112) directly adsorbed to the nickel(111) surface. The nickel crystal was heated from 100 K to 800 K at a temperature ramp of 5 K/s. The inset is an Auger spectrum after thermal desorption and subsequent cooling. The chlorine signature is seen at 180 eV. The peaks at 60 eV and 840 eV are Auger electron energies characteristic of nickel.

presumed to form by either abstraction of a hydrogen from another phenyl group or scavenging surface hydrogen from partial dissociation or background adsorption. The desorption spectrum of benzene shows two desorption peaks centered at approximately 284 K and 364 K. There is also a very broad H_2 desorption peak starting at 420 K and ending around 610 K which agrees well with previous work on benzene/Ni(111)[62]. An Auger spectrum indicates atomic chlorine as the only adsorbate after thermal desorption to 800 K and subsequent cooling. No other dissociation products were observed. Also, no chlorine species is seen to desorb except for small amounts of HCl at a temperature between 500 K and 600 K. HCl at this desorption temperature is assumed to be due to surface hydrogen interacting with adsorbed chlorine.

Photolysis of chlorobenzene/Ni (111). Although we are primarily interested in the photochemistry of chlorobenzene interacting with ice, some comparative information can be obtained by investigating the irradiation of chlorobenzene adsorbed to the nickel surface. The desorption temperatures of the photoproducts are dependent on whether chlorobenzene is adsorbed on ice or whether chlorobenzene is adsorbed on nickel. This distinction must be understood in order to differentiate photolysis of adsorbate-ice systems from photolysis of adsorbate-Ni systems. The photochemistry of chlorobenzene on nickel is dependent on coverage. At submonolayer coverages, the photolysis product benzene desorbs at approximately 425 K and is the sole desorption product. For an irradiation time of 30 min, submonolayer chlorobenzene is completely converted to benzene. No chlorine species is found to desorb after irradiation, and Auger analysis indicates atomic chlorine adsorbed to the nickel. For multilayer coverages, photolysis of

chlorobenzene adsorbed on the nickel surface again produces benzene but at three desorption temperatures. After 30 min photolysis, benzene is found to desorb at 145 K, 284 K, and 364 K. The first desorption temperature is believed to be physisorbed benzene. This peak is absent in the non-irradiated samples. The desorption peaks at 284 K and 364 K are similar to benzene desorption from a nonirradiated sample and is believed to be a product of thermal decomposition of chlorobenzene on the nickel. Interestingly, benzene desorption at 284 K increases with increasing irradiation period while the benzene desorption at 364 K decreases.

Chlorobenzene/H_2O/Ni(111). Chlorobenzene was dosed on continuous thin films of ice at T < 100 K. Fig. 3-3 shows the thermal desorption spectrum of chlorobenzene as a function of coverage. At low coverages, chlorobenzene desorbs from the ice surface at a temperature of approximately 157 K. This desorption peak is assigned as α-chlorobenzene and is indicative of chlorobenzene-ice interfacial interaction. With increasing coverage, a second peak appears at a higher desorption temperature of 168 K. This higher desorption peak is considered to be the physisorbed(condensed) multilayer chlorobenzene and is designated β-chlorobenzene. This phenomenon of a higher multilayer desorption temperature than the monolayer desorption temperature has been seen in other investigations as well[16]. The higher desorption temperature for the physisorbed chlorobenzene provides some qualitative information about the relative strengths of interaction between the chlorobenzene and the ice. The higher desorption temperature indicates that the chlorobenzene-chlorobenzene interaction is stronger than the chlorobenzene-H_2O interaction.

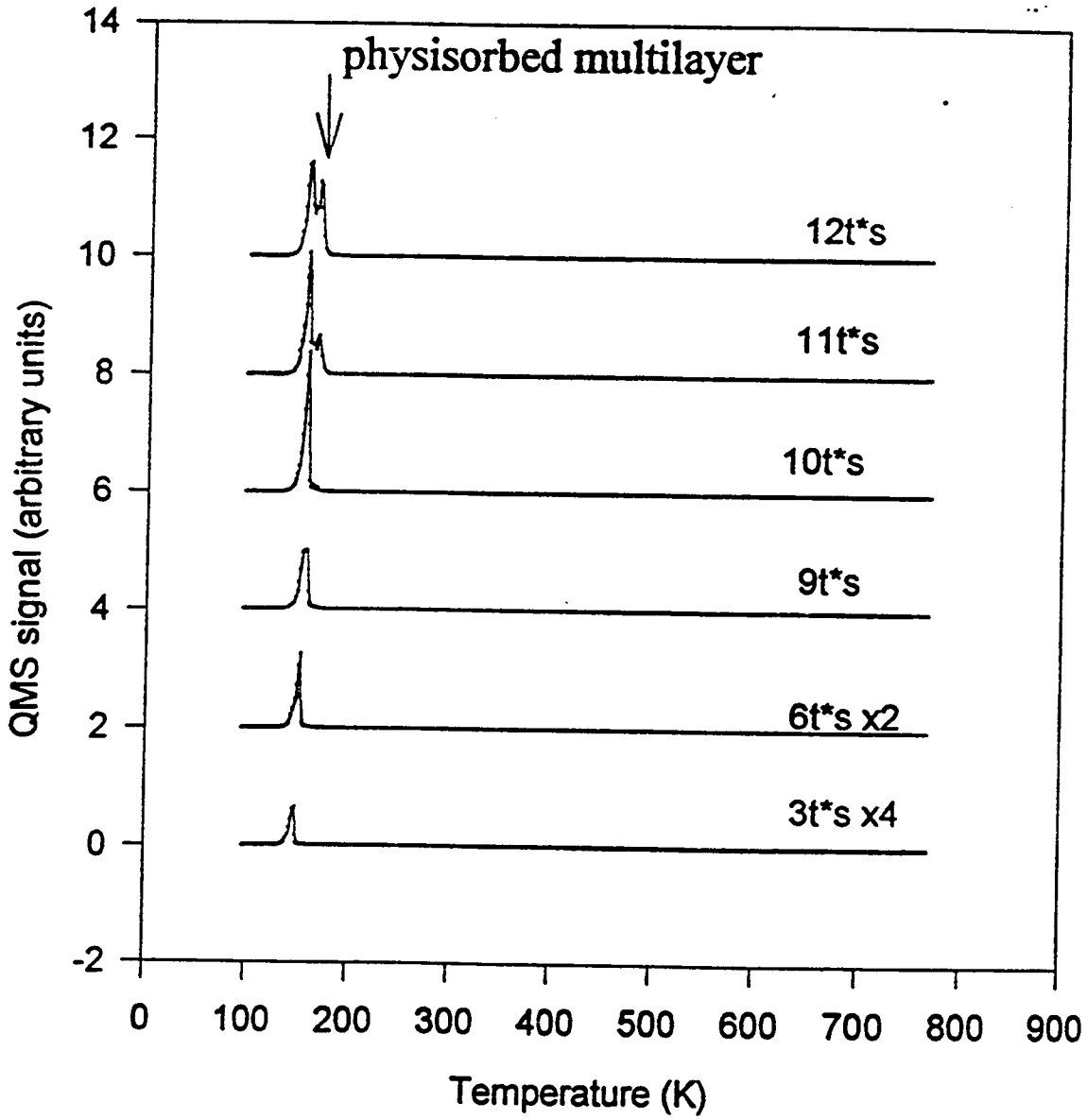

Figure 3-3. Chlorobenzene desorption profile from an ice surface as a function of various coverages. Both chlorobenzene and H_2O were dosed at T<100K. The ice coverage is approximately 18ML. Chlorobenzene is monitored as m/e=112. The temperature ramp is 5 K/s. The notation (t*s) refers to the dosing time (s) at a backing pressure in torr (t).

Due to the weak interaction, chlorobenzene is believed to be molecularly adsorbed to the surface of the ice film. Upon thermal desorption, no dissociative products are observed. Chlorobenzene is the sole desorption product which indicates little thermal reactivity with the ice. In contrast, chlorobenzene on the nickel surface undergoes dissociative reactions producing chemisorbed chlorine and benzene.

With chlorobenzene coverages larger than a monolayer on the ice film, Auger analysis shows small amounts of chlorine bound to the nickel surface. This is not ascribed to defects in the ice film because of the absence of the observation for low coverages of chlorobenzene on a similiar ice surface. This dependence of chlorine access to the nickel surface as a function of coverage is not entirely understood, but it could be attributed to similar desorption temperatures of H_2O and chlorobenzene. If the multilayer coverages for both species were desorbing at similar temperatures, porous cavities formed during the sublimation process could allow access to the nickel for chlorobenzene. For submonolayer coverages, no atomic chlorine is found chemisorbed to the nickel in the Auger spectrum. The desorption temperature for submonolayer chlorobenzene adsorbed on ice is well below the multilayer peak of H_2O.

Photolysis of chlorobenzene/ice. Irradiation of submonolayer coverages of chlorobenzene adsorbed on a continuous film of ice gives benzene as the primary photoproduct. Fig. 3-4 gives the desorption profile of the photoproducts as well as the parent molecule. The benzene desorption temperature is approximately 145 K. This desorption peak is significantly lower than the desorption temperature of H_2O indicating that benzene desorbs from the ice surface. Chlorobenzene is also found to desorb at

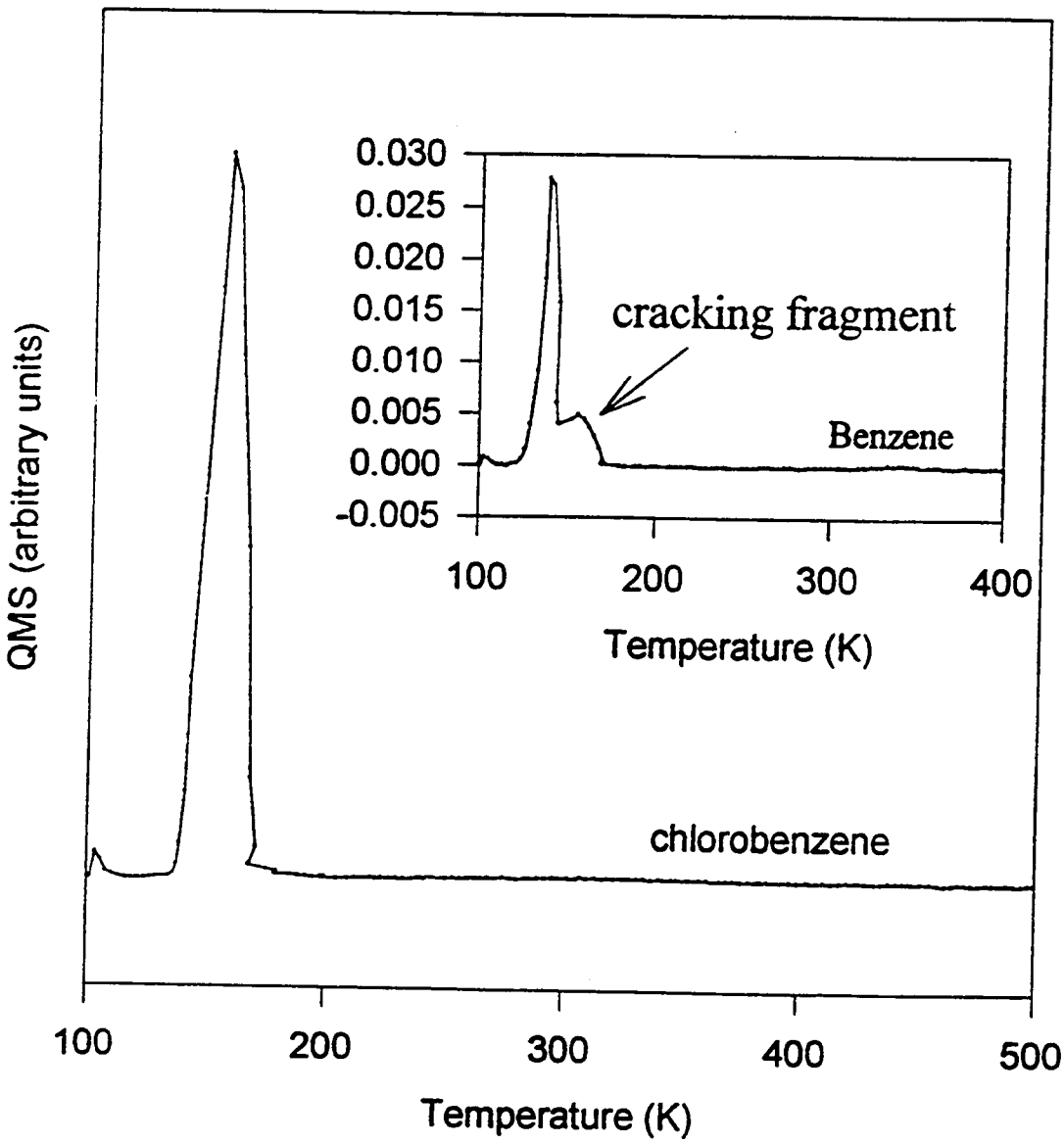

Figure 3-4. Thermal desorption spectrum of a UV irradiated sample of chlorobenzene adsorbed to an ice surface. Irradiation time is 30min. The crystal was ramped to 800K at 5K/s. Both chlorobenzene and H_2O were dosed at T<100K. The photoproduct formed is benzene (m/e=78), which desorbs at a temperature ~ 145K. The small shoulder at a slightly higher temperature is a cracking fragment of chlorobenzene at an ionization energy of 70 eV.

approximately 175 K but with decreasing signal as a function of irradiation time. The amount of benzene obtained increases proportional to the irradiation time. The benzene desorption peak at 145 K is however similar to the irradiated multilayer chlorobenzene coverage on the nickel suggesting that this particular benzene formation is indicative of photophysical processes. No other photoproducts were observed for irradiation of submonolayer chlorobenzene on ice. Following the irradiation and thermal desorption to 800 K, Auger analysis gave atomic chlorine as the only species bound to the nickel surface. No HCl or other chlorine containing species was observed during the thermal desorption process suggesting that nickel is the sole recipient of photolytically dissociated chlorine.

Multilayer coverages of chlorobenzene on the ice show similar photoproducts when irradiated for equal periods with the following exceptions. A small benzene desorption peak at approximately 284 K is observed along with the usual 145 K desorption peak. The 284 K peak increases as a function of irradiation time Also, an Auger spectrum taken after the desorption process indicated carbon as well as chlorine left behind on the nickel surface.

Isotopic studies were incorporated to further elucidate the mechanism of benzene production during UV photolysis and in particular, to determine the source of the hydrogen for benzene production. The phenyl radical once formed can either abstract a hydrogen from the surrounding H_2O or it can form benzene by abstracting a hydrogen(deuterium) from an adjacent parent molecule. D_5-chlorobenzene (m117) was dosed on a continuous ice film at temperatures less than 100 K. Following UV photolysis

for 30 min, a thermal desorption spectrum was taken of the irradiated sample. The desorption temperature for submonolayer coverages of d_5-chlorobenzene is approximately 171 K after irradiation. D_5-benzene at mass 83 and d_6-benzene at mass 84 were also monitored during the desorption process as shown in fig 3-5. Both d_5-benzene and d_6-benzene were found to desorb from ice following irradiation and thermal desorption. d_6-benzene was the more abundant desorbing species indicating abstraction of deteurium from another chlorobenzene source as the primary reaction pathway for photoproduction of benzene. No other chlorine containing species was observed in the thermal desorption profile. Auger analysis again showed chlorine chemisorbed on the nickel surface after thermal desorption.

Multilayer coverages of d_5-chlorobenzene adsorbed to ice were also investigated. Similar desorption profiles for d_5-benzene and d_6-benzene were observed where the fully deuterated benzene was the larger desorption peak. As was the case for the non-deuterated chlorobenzene under similar conditions, an Auger spectrum showed small amounts of carbon as well as chlorine on the surface of the nickel after thermal desorption.

XPS of chlorobenzene/ice. The fate of the chlorine after dissociation from the phenyl ring is of primary interest. In order to determine the reaction pathway of the chlorine, XPS studies of chlorobenzene adsorbed on ice before and after irradiation periods were conducted. A submonolayer coverage of chlorobenzene was introduced to an amorphous ice surface. An XPS spectrum of the chlorine 2p energy level was taken giving a broad peak at a binding energy of 197.7 eV.

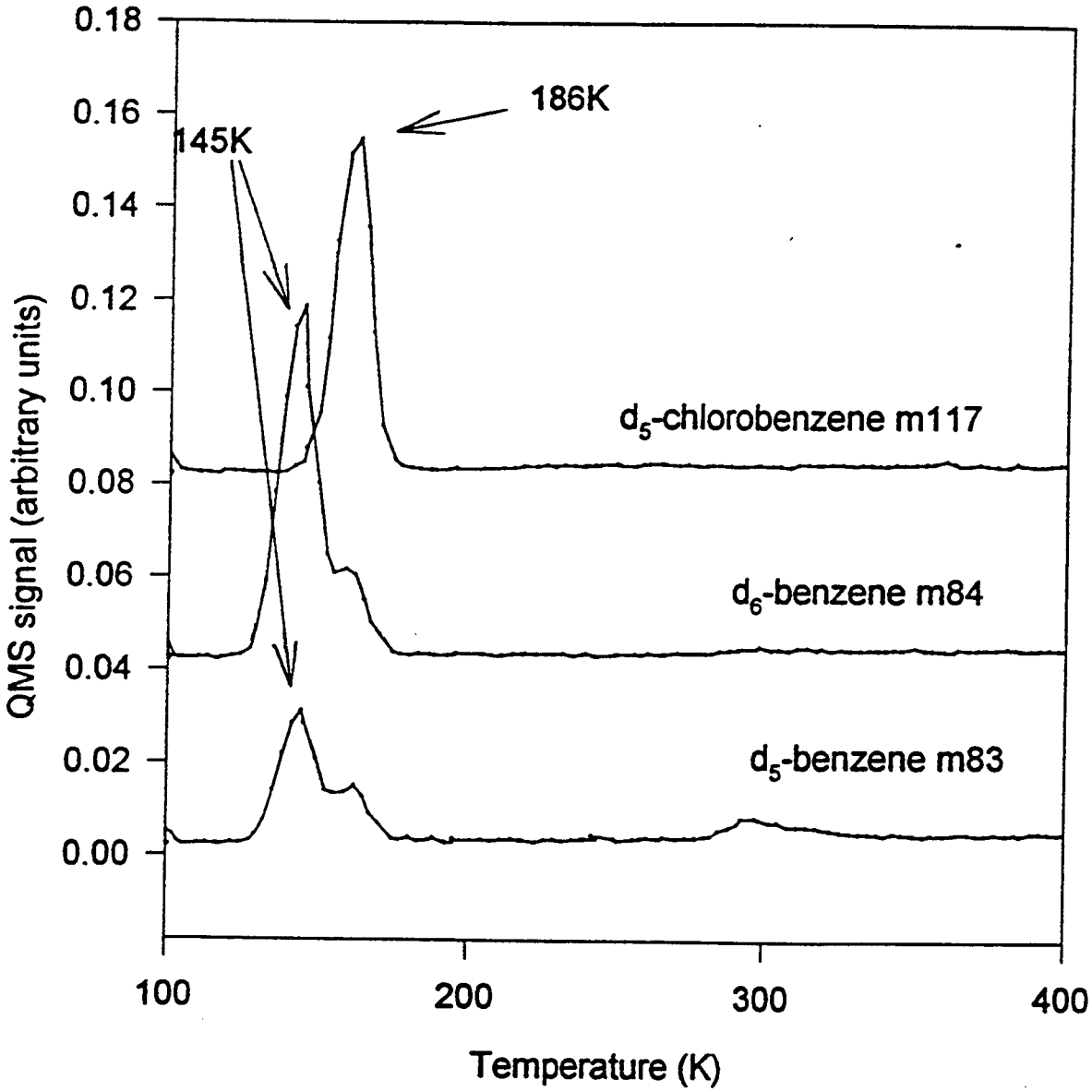

Figure 3-5. Isotopic study of deuterated chlorobenzene (m/e=117) adsorbed to an amorphous ice surface. Sample was irradiated for 30min and then thermally desorbed to 800K. Both chlorobenzene and H_2O were dosed to the nickel at T<100K. Partially deuterated benzene (m/e=83) and fully deuterated benzene (m/e=84) were monitored during the desorption process. Fully deuterated benzene is clearly shown to have a greater intensity than partially deuterated benzene suggesting preferred hydrogen abstraction from an adjacent phenyl ring.

A small shoulder can be seen at a higher binding energy of about 199 eV which we believe is the $2p_{1/2}$ peak. The chlorobenzene gas phase core atomic energy levels for the L_{II} and L_{III} are 201.6±0.3 eV and 200.0±0.3 eV respectively[53]. An XPS spectrum was also taken for the system where chlorobenzene is adsorbed on the nickel surface and thermally desorbed leaving behind chlorine adsorbed on the nickel surface. The chlorine 2p spectrum consisted of a broad peak centered at approximately 195.1 eV. To investigate the chlorine dissociation, a submonolayer coverage of chlorobenzene was dosed on an ice surface at T<100 K. An XPS was taken of the Cl 2p for various irradiation times as depicted in fig. 3-6. Each irradiation period was followed by an XPS scan. The results indicated two peaks at 197.5 eV and 195.1 eV. The higher energy peak attenuated after subsequent photolysis periods and is attributed to a decrease in the molecular chlorobenzene on the surface of the ice. The 195.1 eV peak increases with increasing irradiation time. This peak is attributed to chlorine bound to the nickel. After these sequence of irradiation studies were performed, the system was thermally desorbed and Auger spectrum taken. Chlorine was found on the surface of the nickel. No loss of H_2O occurred during the irradiation for the XPS studies indicating that the ice films were unaffected. Also, a carbon XPS spectrum taken after irradiation showed no noticable change in energy or signal intensity which indicates no loss of carbon compounds to the ambient or to diffusion to the nickel surface. The emergence of the two XPS peaks indicate that during photolysis, two chlorine species were apparent. We attribute these peaks to molecular chlorobenzene on top of the ice and chlorine chemisorbed to the

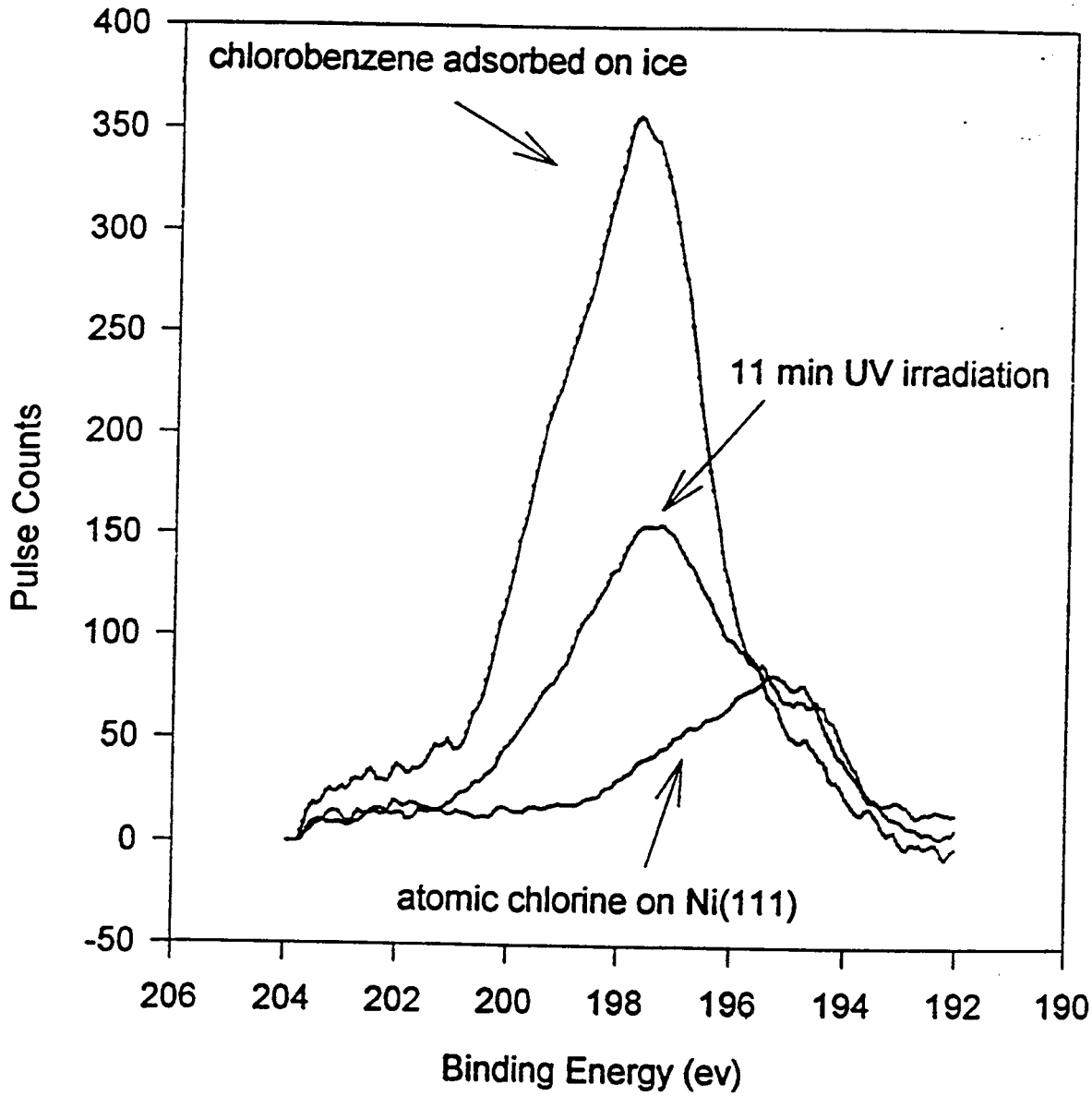

Figure 3-6. An XPS spectrum of chlorobenzene adsorbed to an ice surface. Both species were dosed at T<100K. The chlorine 2p energy level was monitored for various irradiation intervals. The chlorine 2p signal was acquired for 1) chlorobenzene adsorbed to ice before irradiation, 2) after the sample was irradiated for 11min, and 3) after thermal desorption to 800K which shows chlorine adsorbed to the nickel surface.

nickel surface. No other chlorine XPS signatures were observed within the resolution of the experiment.

DISCUSSION

The interaction between the chlorobenzene adsorbate and the ice surface is considered a weak van der Waals type interaction. The higher desorption temperature for the multilayer chlorobenzene relative to the monolayer chlorobenzene suggests that the interaction between the chlorobenzene and ice at the interface is weaker than the bulk phase sublimation energy of the adsorbate. This comparison rests on the assumption that the cohesive energy (binding energy) of multilayer chlorobenzene is approximately represented by the sublimation energy. Fig. 3-7 gives the E_{act} for α-chlorobenzene and ß-chlorobenzene using leading edge analysis. The linearity of the data suggest that the activation energy for desorption is independent of coverage as is expected for zero- order kinetics. The E_{act} for ß-chlorobenzene is higher than the α-chlorobenzene by approximately 15 kJ/mol, and the former is reasonably close to the bulk sublimation energy of chlorobenzene(41 kJ/mol)[63]. This would indicate preferential island formation by the chlorobenzene adsorbate on the ice. Adsorbate island aggregates could facilitate hydrogen abstraction from an adjacent phenyl ring species and possibly explain the observation of d_6-benzene as the favored photolysis product.

Also, the photolysis of chlorobenzene in the presence of ice is similar to photolysis of gas phase chlorobenzene. In the gas phase, photolysis of chlorobenzene gives benzene as the primary photoproduct. The mechanism of benzene production is considered to be

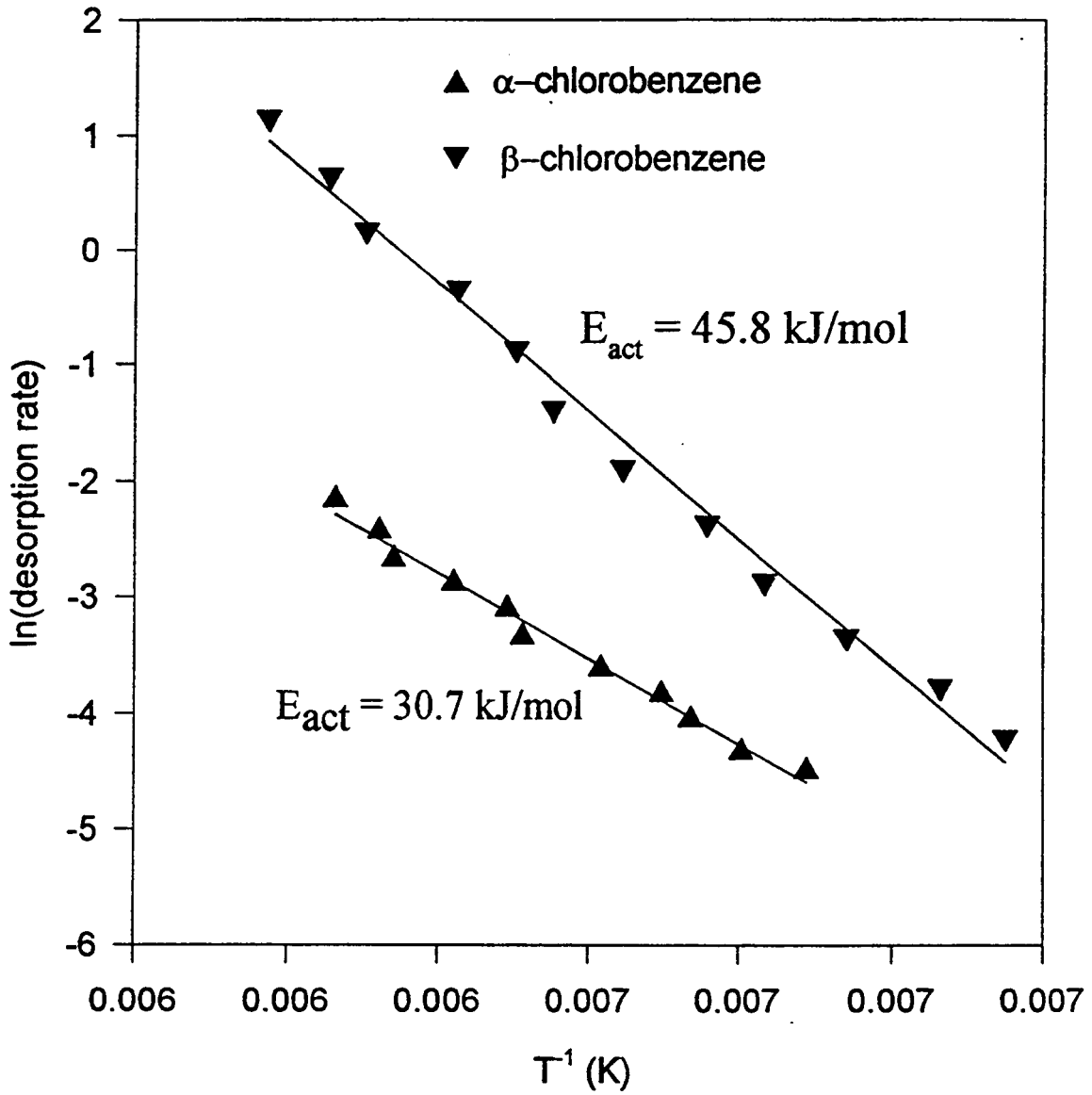

Figure 3-7. A leading edge analysis for a zeroth order plot of the natural log of the desorption rate versus inverse temperature. Both curves represent chlorobenzene desorption from an amorphous ice film. The lower E_{act} is shown for the α- chlorobenzene directly interacting with the ice surface. The higher E_{act} is given for the condensed β-chlorobenzene.

abstraction of a hydrogen by a phenyl radical from an adjacent parent molecule or from another phenyl product. Similar results are seen for chlorobenzene on ice. Stronger interaction with the ice would suggest the formation of aqueous induced products such as phenol and HCl. The absence of the species indicates that the interface region between the substrate and adsorbate is unreactive or at most weakly interactive. The gas phase like photochemistry of chlorobenzene on ice is similar for submonolayer as well as multilayer coverages. For multilayer quantities, the availability of nearby molecules for hydrogen abstraction is evident, but for the submonolayer region, there is less opportunity for intermolecular interaction between chlorobenzene monomers. The gas phase photochemistry for submonolayer coverages of chlorobenzene gives further support to possible island aggregation by lateral attractive forces. Isotopic studies indicate that hydrogen abstraction from an adjacent phenyl ring to form completely deuterated benzene is preferred over abstraction of hydrogen from the ice to form d_5-benzene. This also suggests appreciable lateral diffusion on the surface of the ice.

The fate of the chlorine is of considerable interest. Considering that the interaction between chlorobenzene and ice is weak and that the photochemistry of chlorobenzene under these experimental conditions is similar to gas phase photolysis, the mechanistic pathway of photodissociation would be the formation of diradicals as opposed to zwitterionic dissociation that occurs in the presence of aqueous media. As mentioned previously, the chlorine once dissociated is not found in the desorption spectrum. The XPS study indicates that chlorine diffuses through the ice matrix to the nickel surface. The exact species that diffuses (HCl, Cl_2, Cl) is not clear.

The lack of chlorinated compounds such as HCl and HOCl supports the claim of weak interaction between the ice surface and molecular chlorobenzene during the photolysis. The enthalpy of reaction at 298 K for the following reactions are 68 KJ/mol and 260 KJ/mol respectively.

$$(3.2)\quad H_2O + Cl \rightarrow HCl + OH$$

$$(3.3)\quad H_2O + Cl \rightarrow HOCl + H$$

Both of these endothermic reactions are energetically unfavorable at the substrate temperature of 100 K. At this temperature , thermal energy is on the order of 0.83 kJ/mol. Also, the small cross section for H_2O at 254 nm is not considered efficient enough to produce appreciable amounts of hydroxyl and hydrogen radicals at the adsorbate-ice surface interface. There are reports, however, which indicate fluoresence measurements from hydroxyl species trapped within an ice matrix upon irradiation at 260 nm[64]. Our lack of detection of reaction products such as phenol, HCl, and HOCl indicate that photodissociation and therefore reactivity of H_2O at ~100K is negligible. Based on the energetics of the system, we conclude that the chlorine radical remains unattached in the ice matrix. Assuming that the above reactions are unlikely, the transport mechanism for chlorine to the surface of the nickel appears to be atomic chlorine diffusion through the ice matrix.

Radicals are not as easily solvated as ions, and at 100 K, the ice can be considered as an inert rectangular cage in which gas phase atomic chlorine diffuses. The diffusion mechanism of atomic chlorine in an ice matrix is considered by us to be an entropy driven process. Once chlorine is photodissociated, the radical disperses through the ice media.

The nickel surface, however, can act as a sink for the removal of atomic chlorine from the ice matrix by irreversible chemisorption. This chlorine uptake by the nickel surface initiates a concentration gradient away from the surface of the ice. No chlorine species were found to be released from the surface to the ambient indicating preferential diffusion into the ice. An average distance can be approximated for diffusion of atomic chlorine from the ice surface to the nickel with an appropriate diffusion coefficient. An experimental diffusion coefficient for atomic chlorine in ice is not known, but HCl diffusion through ice has been investigated [65-67]. The diffusion of atomic chlorine through the ice matrix could follow the general diffusion equation found in most physical chemistry texts.

$$(3.4) \quad \partial c/\partial t = D(\partial^2 c/\partial x^2) - v(\partial c/\partial x)$$

where D is the diffusion coefficient and v is the velocity of the diffusing particles flowing through a confined region of area α. The solution to this second order differential equation is

$$(3.5) \quad c = N\exp(-x^2/4Dt)/\alpha(\pi Dt)^{1/2}$$

If one assumes similar diffusion coefficients for HCl (10^{-12} cm^2/sec)[65] and atomic chlorine, then an average distance to diffuse for a given period of time can be approximated. If we imagine the ice film as a rigid rectangle of depth dx and surface area α, then the average distance traveled by the chlorine atoms is

$$(3.6) \quad \langle x \rangle = \int (x_\delta c N \alpha) dx$$

where x_δ is the distance traveled from the origin, c is the concentration(molar), and N is the number of particles present in the ice at all times. Combining equations 3.5 and 3.6 and integrating gives the average distance traveled as

$$(3.7) \quad \langle x \rangle = 2(Dt/\pi)^{1/2}$$

Equation 3.7 gives the mean distance traveled by the chlorine radicals as a function of the square root of the time traveled. This gives some interesting insight to our experimental observations. Assuming an ice film thickness of approximately 50 Å, the time for all photodissociated chlorine atoms to diffuse to the nickel surface is approximately 10^{-3} secs. This would explain the XPS results of only two chlorine signals, one for chlorine on the surface and one for chlorine on the nickel. The fast diffusion negates the possibility of detecting a bulk chlorine constituent.

CONCLUSION

The photochemistry of chlorobenzene adsorbed to a thin ice film was investigated. The photoproducts observed were similar to gas phase photolysis of chlorobenzene indicating very little interaction between chlorobenzene and the ice. Benzene is formed during UV photolysis which desorbs at a temperature of 145 K. Atomic chlorine is observed on the nickel surface after thermal desorption by Auger analysis, and no other chlorine species were found to desorb. The XPS data indicates that two chlorine species are present, one on the ice surface (as molecular chlorobenzene) and one below the ice surface on the nickel at a temperature of ~100 K which is well below the sublimation temperature of the ice film. We propose that chlorine access to the nickel surface is a consequence of

diffusion through the ice matrix. Although the identification of the transport species has not been ascertained, we believe atomic chlorine may be the more likely candidate due to the endothermic energy barrier required to produce molecular chlorine species (HCl, HOCl).

Chapter IV

THEORETICAL TECHNIQUES

The theoretical methods employed within this volume are mostly at the ab initio level of theory accompanied with some Density Functional Theory (DFT) for comparative purposes. All calculations were performed within the *Gaussian 92* package of programs[27] on an IBM RISC 6000 work station. A detailed description of the Hartree-Fock ab initio method will not be given here; however, the reader is referred to excellent references on the subject[28,29,68]. This chapter is given to aid the reader in understanding the techniques and approximations involved in calculating properties of a particular system. Also, a description is given of the cause and effect of adjusting parameters (Hamiltonians, basis sets, etc.) within the model.

The term ab initio means "from the beginning." Ab initio calculations start with a variation of the time independent Schrodinger equation. A wave function is chosen which describes the chemical system under investigation and an appropriate Hamiltonian operates on the wave function in a manner consistent with the iterative process of the Hartree-Fock Self-Consistent Field (HF-SCF) method[28]. These calculations are inherently mathematical in content with essentially no empirical data incorporated except for the universal constants shown in table 4-1. Through manipulations (first and second derivatives) of the SCF total energy, ab initio methods allow fairly accurate determination of a wide number of physical observables such as dipole moments, ionization potentials, binding energies, and vibrational frequencies to name a few.

Table 4-1. Constants used by *Gaussian 92* program package.

Conversion factors
1 Bohr = .529177249 Angstroms
1 Atomic Mass Unit = $1.6605402 \times 10^{-27}$ Kilograms
1 Electron Charge = 4.803242×10^{-10} electrostatic units (ESU)
Plank's Constant = $6.6260755 \times 10^{-34}$ J*s
Avogadro's Number = 6.0221367×10^{23}
1 Calorie = 4.184 Joules
1 Hartree = $4.3597482 \times 10^{-18}$ Joules
Speed of Light = $2.99792458 \times 10^{10}$ cm/sec
Boltzmann Constant = 1.380658×10^{-23} J/K
Inverse Fine Structure Constant = 137.0359895
Molar Volume of Ideal Gas at 273.15 K = .022411 m^3

Modeling a specific system requires a standard input file of the specifications of the molecular system and the parameters involved in the calculation. The level of theory invoked in the computation depends on the choice of Hamiltonian. The choice of Hamiltonians at the zeroth order Hartree-Fock level are: Restricted Hartree-Fock (RHF), Unrestricted Hartree-Fock (UHF), and Restricted Open Hartree-Fock (ROHF). Higher order corrections to the energies can be calculated by Moller-Plesset theory (MP). For the theoretical work in this volume, only the second order corrections to the energies at the Moller-Plesset (MP2) level were investigated for a particular chemical system. There are also several Hamiltonians consistent with Density Functional theory (DFT) offered by *Gaussian 92*. The two most utilized DFT Hamiltonians in this volume were the Becke exchange functional with Lee, Yang, and Parr correlation functionals (BLYP)[69,70] and the Slater exchange functional with Vosko, Wilkes, and Nusair correlation functionals (SVWN)[71].

The calculated properties of a specific chemical system are in most cases largely dependent on the choice of basis sets. Basis sets are mathematical functions that represent the atomic orbitals comprising the atomic or molecular structure under investigation. Standard basis sets for individual atoms up to the transition metals have been established. There are essentially two atomic orbital basis functions used for ab initio calculations. These are Slater-type orbitals (STOs) and Gaussian-type orbitals (GTOs). GTOs are the more applied basis orbitals in use today. The cartesian GTOs are mathematical functions describing the angular and radial distribution of electron density in accord with the following equation

$$(4.1) \quad g_{(i)a,b,c}(r,\theta,\varphi) = N_{a,b,c}(x^a y^b z^c)\exp(-\alpha r^2)$$

where g_i is the atomic orbital, $N_{a,b,c}$ is a normalization constant, a,b, and c are nonnegative integers, and α is an orbital exponent. Standard basis sets are constructed by optimization of the orbital exponent, α, for individual atoms under various molecular environments[72].

Large savings in computational time can be achieved by using linear combinations of the atomic orbitals, g_i, to form Contracted Gaussian-type functions (CGTFs). For example, the 6-31G, 6-31G*, and 6-31+G* basis sets are comprised of CGTFs which are linear combinations of primitive gaussians (g_i). The 6-31G basis set is defined as follows. The first number represents the CGTFs assigned to each inner-core orbital of an atom. The number 6 indicates that the CGTF for each inner-core orbital is composed of a linear combination of 6 primitive gaussians (g_i). The latter numbers in 6-31G represent the valence atomic orbitals. The 31 designation indicates that there are two CGTFs on the valence orbitals. One is composed of a linear combinations of three primitive gaussians, and the other is composed of a single diffuse primitive gaussian. A diffuse primitive gaussian is one with a small orbital exponent (α) which results in a lower gradient with increasing distance from the center. The 6-31G* and 6-31+G* basis sets are similar except for the addition of a polarization function (d gaussian) on each non-hydrogen valence orbital for the 6-31G* and a polarization function along with four highly diffuse functions on each non-hydrogen atomic center for the 6-31+G*. The polarization functions are necessary to accurately describe strained geometries. A substantial difference in the calculated geometries for chlorobenzene can be observed for the 6-31G

and 6-31G* basis sets. The 6-31+G* basis set with the diffuse functions is sometimes necessary to describe species with electron density far removed from the atomic centers. Anions and van der Waals complexes sometimes require diffuse functions to accurately describe their properties. A good rule of thumb to follow is that increasing size of basis set leads to more accurate wave functions and subsequently better representation of properties of a particular chemical system. However, very large basis sets, such as 6-311++G**, are not currently feasible for large systems such as benzene and the halobenzenes. A very large basis set necessarily requires a substantial amount of computational time and disk storage due to the large number of integrals necessary to evaluate. As a general rule, the number of two-electron integrals is proportional to the fourth power of the number of primitive gaussians. For example, calculation of the HF energy for a chlorine atom will require the evaluation of at least 88^4 two-electron integrals (For Cl, a product of 10 inner-core electrons and 6 primitive gaussians gives 60; plus (7x3)+7 for the valence gives a total of 88). Hardware (disk storage) and computational time will greatly dictate not only the chemical system to investigate but also the accuracy at which the calculations are to be performed. These two considerations must be incorporated before efficient use can be made of the calculations.

A description of the procedures and approximations for calculating the various properties of a molecular system will now be given here. The calculated properties of a particular chemical system depend on the total minimum energy of the system. Optimization of the molecular structure under investigation is first necessary to locate a true local or global minimum (depending on which is sought) on the potential energy

surface (PES). Optimizations can be performed for all variable coordinates which span the allowed degrees of freedom (full optimization) or for specified coordinates with all other variables fixed (partial optimization). Full and partial optimizations were performed for the various systems investigated in this volume and are labeled as such. All non-complexed structures reported here have been optimized at very tight convergence criteria. However, due to the large amplitude motion of the bimolecular complexes, it was found that very tight convergence criteria was not feasible for most of the larger complexes, i.e. chlorobenzene-H_2O. Nevertheless, the tight convergence criteria was found to be sufficient for the zeroth order calculations regarding the complexes.

The degree of accuracy for calculations of the true ground state energy of a molecular species depends on the threshold limits set prior to optimization. The location of the ground state minimum is recognized by optimization to within four threshold values for each variable coordinate. These are 1) maximum dE/dR, 2) rms dE/dR, 3) maximum displacement, and 4) rms displacement. Depending on the accuracy required, these thresholds can be set for *tight* convergence or *verytight* convergence with the latter giving a better representation of the true minimum and hence more accurate properties dependent on the first and second derivatives of the total energy.

True minima for a particular molecular structure can be ascertained by determining the frequencies of the normal modes of vibrations. The vibrational frequencies for the normal modes are calculated using the harmonic approximation. The frequencies are calculated from second derivatives of the total energy with respect to nuclear coordinates. Only analytical frequencies were calculated in this volume. However, an optimization must first

be performed on the molecular system prior to frequency evaluation. The calculated frequencies are valid only for stationary points on the potential energy surface. Calculations of the frequencies for points on the PES other than stationary points (minimums) results in negative frequencies. Negative frequencies (imaginary frequencies) indicate that the minimum found on the PES is not a legitimate minimum. However, the number of negative frequencies can be useful by providing a description of the local potential energy surface. For instance, one negative frequency value indicates that the structure is a 1st order saddle point and is a transition state connecting two minima. In general, the order of the saddle point follows [x^{th}], where x is the number of imaginary frequencies.

Binding energies of bimolecular van der Waals and hydrogen bonded complexes are often determined theoretically by ab initio techniques. The binding energy (E_{bind}) of a bimolecular complex (AB) is the energy required to dissociate the complex into its molecular constituents and is represented by the following equation

$$(4.2) \quad AB \rightarrow A + B$$

$$(4.3) \quad E_{bind} = [E_{AB} - (E_A + E_b)]$$

The total ground state energy of complex AB and the constituents A and B are calculated at a specified level of theory. The combined energies of A and B are subtracted from the total energy of complex AB to give the binding energy. However, certain corrections and approximations are employed. Basis set superposition error (BSSE) is incorporated in calculations of the total energies of molecular constituents A and B. BSSE arises due to the fact that more basis sets are employed for the calculation of the complex than are

employed on the constituents thereby resulting in calculation of a slightly more positive artificial ground state energy for the constituents. To compensate for this artificial minimum energy, the counterpoise technique[73] is employed to correct for the BSSE error. This technique involves superimposing artificial ghost atoms (nuclear potential set to zero) on one of the constituents to allocate the needed basis sets for energy minimization. This is likewise performed for the other constituent. When included, BSSE corrections to the molecular constituents will always lower the total calculated binding energy for the complex.

Ionization potentials for atoms or molecules can also be calculated with ab initio techniques in a manner similar to the binding energy determination. Ionization potentials (IPs) are taken as the difference in the total ground state energy of the neutral species and the ionized state of the ion species. For example, the IP for chlorobenzene is calculated as the difference between the neutral chlorobenzene ground state and the chlorobenzene cation with a single positive charge and a multiplicity of 2. This is consistent with calculations of vertical ionization potentials. For adiabatic ionization potentials, the ionized species is allowed to fully optimize its geometry under its new electronic environment. A general rule of thumb is that calculated adiabatic IPs are always less than the corresponding vertical IPs with the relative difference depending on the degree of geometric relaxation upon ionization. Electron affinities (EAs) are calculated as the negative of the IPs.

Chapter V

THEORETICAL RESULTS OF CHLOROBENZENE AND CHLOROBENZENE-H_2O COMPLEX

Ab initio calculations were performed to determine the interactions between chlorobenzene and H_2O at the molecular level. The structures and energetics were calculated for one to one complexes of chlorobenzene and H_2O, benzene and H_2O, and fluorobenzene and H_2O. The latter two complexes were investigated to provide complementary information to the chlorobenzene-H_2O system.

The interaction between monomers of H_2O and the above aromatic compounds is primarily hydrogen bonding. The extent of the binding interaction and orientation has not been found to be greatly dependent on the substituent to the phenyl ring. H_2O complexation with benzene has been studied previously at both the experimental and theoretical levels[74-79]. H_2O binds to the surface of benzene with the water hydrogens participating in a π-type hydrogen bond to the π ring. The orientation and substantial mobility of H_2O on top of the benzene is such that effective C_{6v} symmetry is observed. The chlorobenzene complex, however, does not allow the tumbling of H_2O as observed for benzene. Calculations show that the H_2O molecule is bound to the surface of the phenyl ring with one hydrogen preferentially directed toward the para-carbon and the other directed over the center of the π-ring with the plane of the H_2O molecule perpendicular to the plane of chlorobenzene.

Interestingly, it was found that the binding energy of the benzene-H_2O complex was larger than the binding energies of both the chlorobenzene-H_2O and fluorobenzene-H_2O complexes. The binding energies at the MP2/6-31G*//RHF/6-31G* level of theory were determined to be 2.210 kcal/mol, 1.884 kcal/mol, and 1.892 kcal/mol respectively. The chlorobenzene and fluorobenzene complexes were found to have very similar binding energies which indicates that the binding mechanism is independent of the specific halogen.

Geometries and vibrational spectra were calculated here for isolated chlorobenzene and benzene and for the complexes of both molecules with H_2O. The harmonic approximation was used for the vibrational calculations. Both frequencies and intensities were calculated for the above species. It was found during the course of this work that Wilson's notation[80] for labeling the normal modes of benzene was still being used to label the corresponding modes of substituted benzenes (chlorobenzene, fluorobenzene) even though the symmetry of both structures are dissimilar. A correlation diagram is provided here between the normal modes of benzene and the equivalent normal modes of chlorobenzene. The correlation diagram describes the splitting of the degenerate modes of benzene to the daughter modes as a result of ring substitution. The labeling of the normal modes for both benzene and chlorobenzene is consistent with Mulliken notation.

For the chlorobenzene-H_2O complex, the perturbations to the free H_2O normal modes and the free chlorobenzene modes as a result of complexation is used here to probe the extent of hydrogen bonding occurring within the complex. The calculated fluctuations in intensities and frequency shifts are used to describe the intermolecular interactions.

GEOMETRY AND ENERGETICS

Geometry of Benzene. Atomic labeling for benzene is seen in figure 5-1. The benzene molecule is highly symmetric with all carbon-carbon bond lengths the same as well as all carbon-hydrogen bond lengths being similar. The planar hexagonal structure with all bond angles at 120° gives a 6-fold rotational axis perpendicular to the plane of the ring and allows for the structure to be classified as possessing D_{6h} symmetry. The bond distances and angles as well as other spectroscopic properties of benzene have been calculated at several different levels of theory to give an indication of how well the physical properties of aromatic compounds can be modeled at the ab initio level.

The calculated values for the geometry as well as some important spectroscopic properties are shown in table 5-1 along with the experimental values. All C-C-C and C-C-H bond angles are 120.0° and are not shown in the table. Within the RHF level for the various basis sets, the benzene structure itself is not overly dependent on the choice of basis set. The carbon-carbon (C-C) bond lengths show a variation of only a few thousandths of an angstrom from the 6-31G to the 6-31++G** basis set. The carbon-hydrogen (C-H) bond lengths show a somewhat smaller variation above 6-31G. Both the calculated C-C and C-H bond lengths at all basis sets show deviations to the nearest hundredth of an angstrom from the experimental values of 1.397 Å and 1.086 Å respectively[81].

The C-C and C-H bond distances are improved with the inclusion of electron correlation at the MP2 level of theory. The C-C and C-H bond distances calculated at the

R (C-C) = 1.38617
R (C-H) = 1.07561
α (C-C-C) = 120.00000
α (C-C-H) = 120.00000

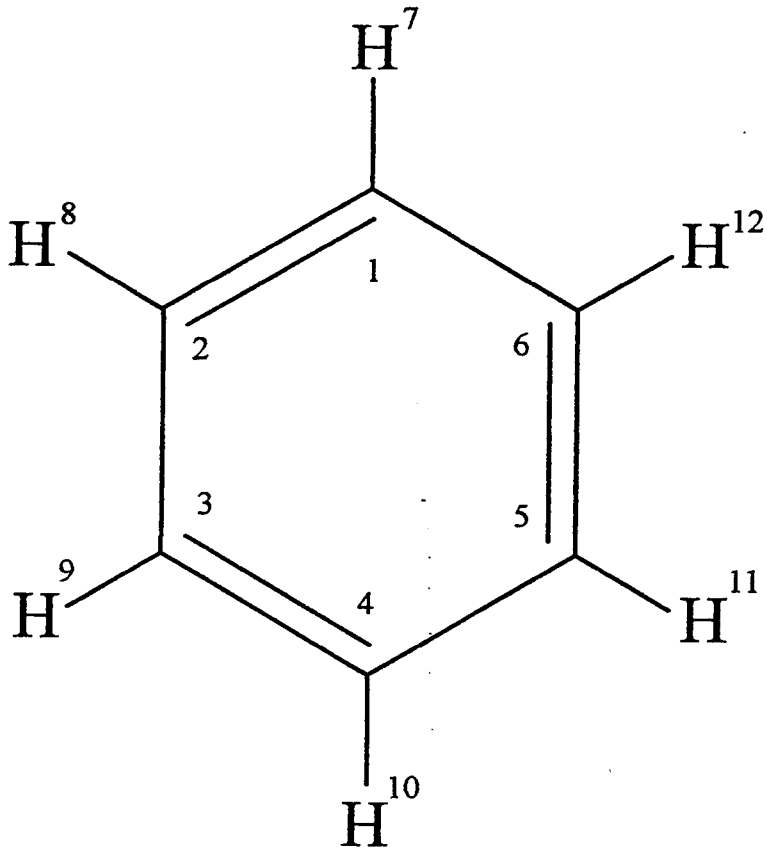

Figure 5-1. Optimized geometry of benzene at RHF/6-31G* with *verytight* convergence criteria. Structure has D_{6h} symmetry.

Table 5-1. Calculated values for benzene at various levels of theory. Convergence criteria for optimization is *very tight.*

	R (C-C) Å	R (C-H) Å	Polarizability Å^3				IP (eV)	Energy (a.u.)
			α_{xx}	α_{yy}	α_{zz}	α_{avg}		
RHF/6-31G	1.388302	1.073287	10.025	10.025	2.711	7.587	5.66	230.624474915
RHF/6-31G*	1.386174	1.075606	10.115	10.115	3.077	7.769	7.80	230.703137024
RHF/6-31+G*	1.388128	1.075664	10.952	10.952	6.009	9.304	12.64	230.711092524
RHF/6-31++G**	1.387948	1.075776	11.035	11.035	6.142	9.404	12.60	230.721913012
MP2/6-31G	1.412760	1.091102	---	---	---	---	11.27	231.140758886
MP2/6-31G*	1.396791	1.087424	---	---	---	---	9.20	231.457733612
BLYP/6-31G*	1.406675	1.094372	10.892	10.892	3.138	8.307	8.75	232.132389355
BLYP/6-31+G*	1.408831	1.094763	12.173	12.175	6.293	10.214	8.97	232.144613915
SVWN/6-31G*	1.390474	1.096045	10.718	10.718	3.157	8.198	10.01	230.903228833
SVWN/6-31+G*	1.392126	1.096577	11.825	11.827	6.032	9.895	10.16	230.912516999
Experimental	1.397[a]	1.086[a]		10.32[b]			9.24[c]	---

[a]Langseth, A.; Stoicheff, B.P. *Can. J. Phys.* 1956, 34, 350.
[b]Hirschfelder, J.O., Curtis, C.F.; Bird, R.B. *Molecular Theory of Gases and Liquids*, John Wiley & Sones, NewYork, 1954, 950.
[c]Watanabe, K. *J. Chem. Phys.* 1957, 26, 542.

MP2/6-31G* level are 1.397 Å and 1.087 Å respectively and match the experimental values nicely. The polarization functions inherent in 6-31G* seem necessary for an accurate description of benzene at the MP2 level. The MP2/6-31G calculation overestimates the bond lengths more than any other basis set at the MP2 or RHF level of theory.

Ionization potentials (IPs) and polarizability values were also calculated for benzene. The calculated ionization potentials at the RHF level show a large dependence on basis set as seen in table 5-1. The calculated IP values increase with increasing size of basis set at the RHF level and give rather poor comparison to the experimental vertical ionization potential of 9.24 eV[82]. Inclusion of electron correlation at the MP2 level gives more reasonable values for the IP. The calculated IP at MP2/6-31G* gives excellent agreement with the experimental value with a difference of less than 1%.

The calculated polarizability for benzene shows a similar dependence on basis set as did the IP for the RHF level with better values being obtained at higher basis set. Interestingly, the calculated polarizability shows a substantial dependence on the addition of diffuse functions to the basis set. However, for basis sets as large as 6-31++G**, the calculated polarizability is still underestimated by ~ 9%. Polarizability values could not be calculated at the MP2 level due to hardware limitations, but it is expected that the polarizability is largely effected by electron correlation.

Density functional theory (DFT) was also used to characterize the structure and spectroscopic properties of benzene. DFT methods provide similar information compared to MP2 calculations but with less hardware restrictions. Two DFT methods were

attempted consisting of the Beck exchange functional combined with the LYP correlation functionals (BLYP), and another consisting of the Slater exchange functional combined with the VWN correlation functional (SVWN). The DFT results are shown in table 5-1. The C-C bond distances were reasonably handled by both DFT methods at 6-31G* and 6-31+G* with SVWN having the better values. The C-H bonds were overestimated by both methods by approximately a tenth of an angstrom. The IP for benzene is represented better by SVWN than BLYP giving 8.75 eV and 10.01 eV respectively. The addition of a set of diffuse functions to the basis set had less of an effect than that displayed by the RHF and MP2 methods. Also, both DFT methods gave better values than both RHF and MP2 methods for the polarizability of benzene with the addition of diffuse functions inherent in 6-31+G*.

Geometry of chlorobenzene. Atomic labeling for geometry considerations are shown in fig. 5-2. The geometry of chlorobenzene was optimized under the RHF hamiltonian for several basis sets. The calculated geometric parameters and experimental values[83] are shown in table 5-2 for the various methods used. The calculated bond distances and angles are suprisingly similar (with larger basis sets) to the experimental values. Chlorobenzene has C_{2v} symmetry with the C_2 axis along the carbon-chlorine bond. The perturbations to the phenyl ring as a result of chlorine substitution is evident in the angles and bond length differences relative to the benzene structure. The C6-C1-C2 angle shown in figure 5-2 shows a calculated increase of 1.2° at the RHF/6-31G* level from the usual 120° of benzene due to the chlorine substituent. The increase in the angle could be contributed to the electron withdrawing effect of the chlorine substituent. The reduction

R (1-2) = 1.383002
R (2-3) = 1.385445
R (3-4) = 1.385374
R (1-7) = 1.745285
R (2-8) = 1.073449
R (3-9) = 1.075035
R (4-10) = 1.074874
α (1-2-3) = 119.0712
α (2-3-4) = 120.3988
α (3-4-5) = 119.7776
α (2-1-6) = 121.2823
α (7-1-2) = 119.3589
α (8-2-3) = 120.8570
α (9-3-4) = 120.1748

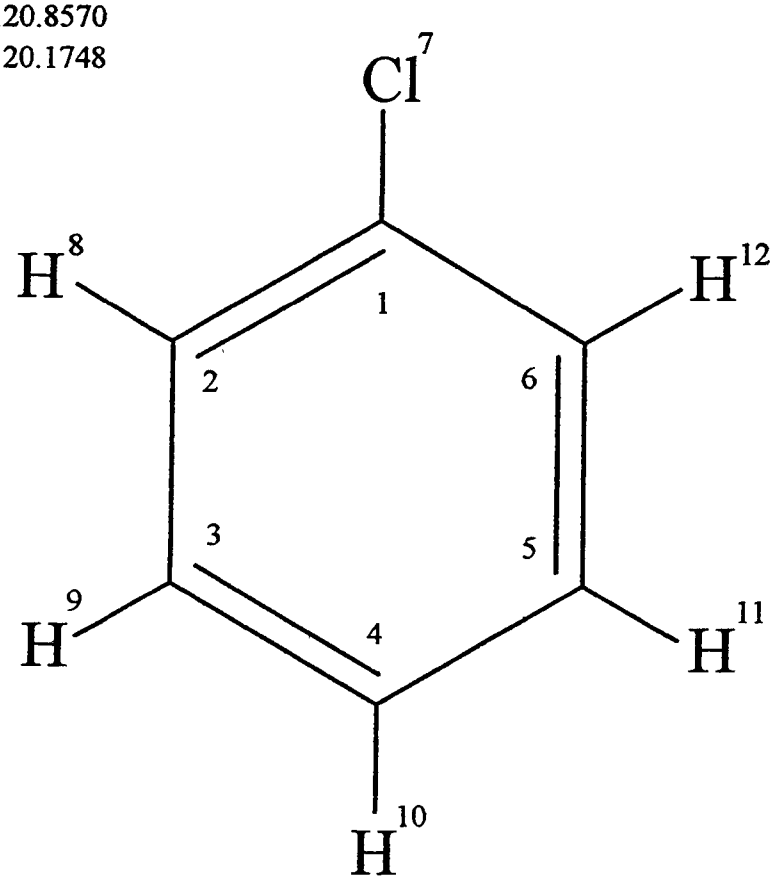

Figure 5-2. Optimized geometry of chlorobenzene at RHF/6-31G* with *verytight* convergence criteria. Structure has C_{2v} symmetry.

Table 5-2. Optimized values for chlorobenzene at various levels of theory. See Figure 5-2 for numbering scheme. Polarizabilities are given as xx, yy, zz tensors along with the average value in paranthesis.

	RHF/6-31G	RHF/6-31G*	RHF/6-31+G*	Experimental[a]
R (C1-C2)	1.380052	1.383002	1.384192	1.3908(18)
R (C2-C3)	1.388296	1.385445	1.387283	1.3942(16)
R (C3-C4)	1.387627	1.385374	1.387109	1.4000(12)
R (C1-Cl7)	1.811884	1.745285	1.744205	1.7390(23)
R (C2-H8)	1.070669	1.073449	1.073768	1.0779(21)
R (C3-H9)	1.072478	1.075035	1.075204	1.0872(21)
R (C4-H10)	1.072451	1.074874	1.075023	1.0795(21)
α (C1-C2-C3)	118.7661	119.0712	119.1095	119.05(15)
α (C2-C3-C4)	120.2697	120.3988	120.3991	120.24(12)
α (C3-C4-C5)	119.9312	119.7776	119.7388	119.79(11)
α (C2-C1-C6)	121.9972	121.2823	121.2441	121.65(23)
α (Cl7-C1-C2)	119.0014	119.3589	119.3780	119.17
α (H8-C2-C3)	120.9476	120.8570	120.7941	121.28
α (H9-C3-C4)	120.2366	120.1748	120.1728	119.35
α (H10-C4-C3)	120.0344	120.1112	120.1306	120.10
E(RHF) (a.u.)	689.501937948	689.603345067	689.610160333	---
dipole (Debye)	2.7337	2.1483	2.0679	1.691[b]
Ionization Potential (eV)	8.389	8.033	8.139	9.073[c]
Polarizability Å^3	10.236, 13.677, 3.142, (9.018)	10.542, 13.564, 3.773, (9.293)	11.601, 14.511 6.609, 10.907	14.1[d]
ZPVE (a.u.)	.0990058	.0977162	.0975967	---

[a]All bond lengths and angles obtained from Cradock, S; Muir, J.; Rankin, D.W., *J of Mol Struc.*, **1990**, 220, 205-215.

[b]Potts, A.W.; Lyus, M.L.; Le, E.P.F.; Fattahallah, G.H. *J. Chem. Soc. Farada II* **1980**, 76, 556.

[c]Ripoche, X.; Asselin, P.; Piuzzi, F.; Dimicoli, I. *Chem Phys.* **1993**, 175, 379.

[d]Miller, T.M.; Bederson, B. *Advances in Atomic and Molecular Physics* 1977,13, 1 references therein.

in electron density localized around the substituted carbon results in relaxation of the 120° hexagonal requirement of the benzene ring.

The chlorine substituent also affects the C-C bond distances relative to the benzene structure. The calculated values for the C-C bond distances show a lengthening of carbon-carbon bonds with increasing distance away from the chlorine bound carbon. However, from table 5-2, the C2-C3 bond length is somewhat higher than the C3-C4 bond length. This is consistent for all basis sets at the RHF level. The experimental values for the carbon-carbon bond distances show a similar increase in bond lengths with increasing distance from the chlorine substituted carbon but with the C3-C4 bond having a larger bond length than C2-C3.

The calculated values for the carbon-hydrogen bond distances are very similar to the experimental values. The calculated values also agree with the experimental ordering of C-H bond lengths. The largest C-H bond length is at the meta position with the para and the ortho C-H bond distances being somewhat shorter. Interestingly, the ortho and para positions of chlorobenzene are the primary reaction sites for electrophilic aromatic substitution. The shortening of the bond length at these positions could be interpreted as an increase in the partial negative character of the carbons at these positions relative to the meta position. From an electrostatic approach, this would indicate an increase in the bond strengths (shorter bond length) at these positions. The possibility of stronger bond formation for electrophilic substituents could be considered as a driving force for substitution at these positions.

Better agreement of all calculated geometric bond distances and angles of chlorobenzene with experimental values are apparent with increasing size of basis set under the Hartree-Fock level of theory as shown in table 5-2. However, the carbon-chlorine bond distance shows a more pronounced dependence on size of basis set. The calculated carbon-chlorine bond distance is given as 1.811 Å with the 6-31G basis set which gives a rather large difference (4%) from the experimentally determined value of 1.739 Å[83]. The basis set dependence is easily seen when the polarization functions are added to the 6-31G basis set. The carbon-chlorine bond distance is better represented by the 6-31G* basis set giving a 0.36% error (an order of magnitude difference from 6-31G) when compared to the experimental bond distance. The addition of diffuse functions inclusive in 6-31+G* improves the C-Cl bond distance only slightly. The experimental C-Cl bond distance in chlorobenzene is intermediate between the C-Cl bond distances of vinyl chloride(1.726 Å[84]) and methyl chloride(1.785 Å[85]). Incidentally, the calculated values of 1.737 Å and 1.784 Å for vinyl chloride and methyl chloride respectively optimized at RHF/6-31G* agree well with the experimental values. Good agreement with experimental values and reasonable computational time establish the 6-31G* basis set as a *minimum* choice of basis set for aromatic structures at the RHF level with the added polarization functions being a necessity.

The ionization potential and polarizability were also calculated for chlorobenzene at various basis sets under the RHF hamiltonian. The calculated ionization potential shows no consistent pattern with basis set. For the 6-31+G* basis set, the calculated IP for chlorobenzene is 8.14 eV. This value is reasonably close to the experimental value of 9.07

eV[86] as shown in table 5-2. Calculations of the polarizability of chlorobenzene show a correlation with increasing size of basis set. However, the calculated values fall considerably short of the experimentally determined 14.1 $Å^3$.[87]

Calculations at the MP2 level of theory were also performed for structural characterization of chlorobenzene. The calculated values are shown in table 5-3a. The C-C bond lengths show similar results to the RHF level. However, unlike the RHF/6-31G*, the MP2/6-31G* method agrees with the order of increasing C-C bond distance with increasing distance away from the substituted carbon. No substantial improvement is observed for the C-Cl bond distance at the MP2 level. The C-H bond length at the meta position is much better represented by MP2/6-31G* with excellent comparison to the experimental value. The ortho and para C-H bond lengths are overestimated at the MP2 level and are better represented at the RHF/6-31G* level.

Dipole moment of chlorobenzene. The dipole moment for gas phase chlorobenzene is 1.69D[88] with the negative end of the dipole vector located on the chlorine. The dipole moment for chlorobenzene is poorly represented at the RHF level of theory for all basis set attempts. At the RHF level, the dipole moment improves with increasing basis set, but it is still greatly overestimated giving a 22% error with RHF/6-31+G*. Electron correlation methods (ie MP2, QCISDT,...) are essential for accurate representation of dipole moments. The calculated dipole moment at MP2/6-31G* using the MP2 density gives a dipole moment of 1.8891 which reduces the error by half relative to the RHF level but is still rather high.

Table 5-3a. Optimized values for chlorobenzene at the MP2 level of theory. Optimization is at *verytight* convergence criteria. See Figure 5-2 for numbering scheme.

	MP2/6-31G	MP2/6-31G*	Experimental
R (C1-C2)	1.404701	1.394936	1.3908(18)
R (C2-C3)	1.412796	1.395807	1.3942(16)
R (C3-C4)	1.412244	1.396353	1.4000(12)
R (C1-Cl7)	1.841017	1.742509	1.7390(23)
R (C2-H8)	1.089058	1.086204	1.0779(21)
R (C3-H9)	1.090470	1.087128	1.0872(21)
R (C4-H10)	1.090272	1.086750	1.0795(21)
α (C1-C2-C3)	118.8337	119.0493	119.05(15)
α (C2-C3-C4)	120.3314	120.4649	120.24(12)
α (C3-C4-C5)	119.8120	119.7247	119.79(11)
α (C2-C1-C6)	121.8578	121.2470	121.65(23)
α (Cl7-C1-C2)	119.0711	119.3765	119.17
α (H8-C2-C3)	120.9280	120.9942	121.28
α (H9-C3-C4)	120.2702	120.1787	119.35
α (H10-C4-C3)	120.0940	120.1377	120.10
E(RHF) (a.u.)	690.06372505452	690.49059583178	---
dipole (Debye)	2.3545	1.8891	1.69

It is widely known that Density Functional Theory (DFT) methods offer adequate treatment of electron correlation and provide reasonable values for dipole moments while also being computationally feasible. The BLYP and SVWN functionals were used with several basis sets, and the calculated dipole moments are shown in tables 5-3b,c. The BLYP/6-31+G* gives a value of 1.8775 D. This value however is still quite large giving an 11% error to the experimental dipole. The SVWN gave surprisingly good results for the dipole of chlorobenzene. With SVWN/6-31+G*, the dipole for chlorobenzene was calculated to be 1.7097 D which reduces the error to < 1%.

Benzene-H_2O geometry. The calculated minimum geometry for the benzene-H_2O complex is shown in figure 5-3. This geometry was obtained by optimizing only the intermolecular variables while fixing the individual geometries at their free RHF/6-31G* optimized geometry. The center of mass separation for the two monomers is calculated to be 3.531 Å which overestimates the experimentally observed center of mass separation of 3.32 Å[79]. For ease of calculation, the oxygen approximates the center of mass for the water molecule. As seen in figure 5-3, the water molecule acts as a proton donor and is bound to the center of the benzene ring with the C_2 axis of water *approximately* parallel with the C_6 axis of benzene. The approximate designation is necessary due to the C_2 axis of water being slightly off center of the C_6 axis of benzene thereby perturbing the expected overall C_{2v} symmetry to C_s. This is an unusual hydrogen bonding scheme in that the hydrogens of the water molecule are both pointing symmetrically toward the center of the ring.

Table 5-3b. Optimized values for chlorobenzene at the BLYP level of theory. Optimization is at *verytight* convergence criteria. See Figure 5-2 for numbering scheme.

	BLYP/6-31G	BLYP/6-31G*	BLYP/6-31+G*	Experimental[a]
R (C1-C2)	1.403271	1.404153	1.405565	1.3908(18)
R (C2-C3)	1.411696	1.406137	1.408158	1.3942(16)
R (C3-C4)	1.410341	1.406034	1.407991	1.4000(12)
R (C1-Cl7)	1.854330	1.783580	1.783299	1.7390(23)
R (C2-H8)	1.090246	1.091808	1.092357	1.0779(21)
R (C3-H9)	1.092663	1.093930	1.094327	1.0872(21)
R (C4-H10)	1.092405	1.093536	1.093887	1.0795(21)
α (C1-C2-C3)	118.3914	118.8151	118.8570	119.05(15)
α (C2-C3-C4)	120.4117	120.4988	120.5060	120.24(12)
α (C3-C4-C5)	119.9231	119.7726	119.7218	119.79(11)
α (C2-C1-C6)	122.4708	121.5996	121.5521	121.65(23)
α (Cl7-C1-C2)	118.7646	119.2002	119.2239	119.17
α (H8-C2-C3)	121.0772	121.0378	120.9440	121.28
α (H9-C3-C4)	120.2649	120.2181	120.2260	119.35
α (H10-C4-C3)	120.0385	120.1137	120.1391	120.10
Energy(RHF) (a.u.)	691.653866465	691.718122048	691.730426314	---
dipole (Debye)	2.3911	1.9037	1.8775	1.69

Table 5-3c. Optimized values for chlorobenzene at the SVWN level of theory. Optimization is at *verytight* convergence criteria. See Figure 5-2 for numbering scheme.

	SVWN/6-31G	SVWN/6-31G*	SVWN/6-31+G*	Experimental
R (C1-C2)	1.387709	1.388864	1.390047	1.3908(18)
R (C2-C3)	1.394401	1.389286	1.390752	1.3942(16)
R (C3-C4)	1.394217	1.390161	1.391629	1.4000(12)
R (C1-Cl7)	1.800898	1.733945	1.733312	1.7390(23)
R (C2-H8)	1.093232	1.094592	1.095320	1.0779(21)
R (C3-H9)	1.094516	1.095673	1.096233	1.0872(21)
R (C4-H10)	1.094214	1.095216	1.095758	1.0795(21)
α (C1-C2-C3)	118.6048	118.9804	119.0319	119.05(15)
α (C2-C3-C4)	120.3722	120.4686	120.4785	120.24(12)
α (C3-C4-C5)	119.8965	119.7572	119.7068	119.79(11)
α (C2-C1-C6)	122.1498	121.3447	121.2724	121.65(23)
α (Cl7-C1-C2)	118.9251	119.3276	119.3638	119.17
α (H8-C2-C3)	121.2902	121.3103	121.2031	121.28
α (H9-C3-C4)	120.2356	120.2017	120.2049	119.35
α (H10-C4-C3)	120.0517	120.1214	120.1466	120.10
Energy(RHF) (a.u.)	689.279676351	689.357655865	689.367143136	---
dipole (Debye)	2.2081	1.7428	1.7097	1.69

Oxygen-ring center separation = 3.531013

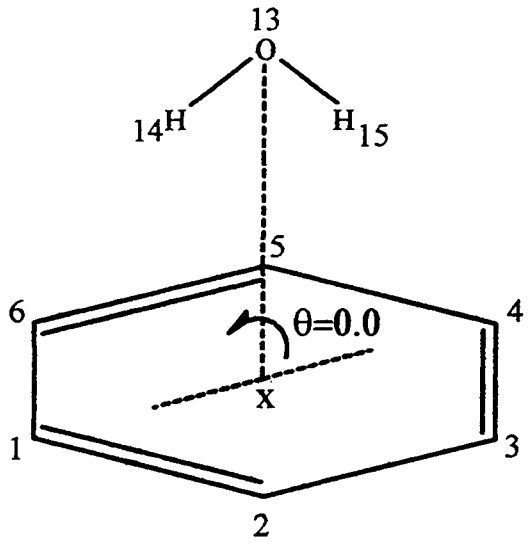

Figure 5-3. Optimized geometry for benzene-H_2O calculated at RHF/6-31G*. The structure has C_s symmetry. θ = 15-13-X-4 dihedral.

The benzene-H_2O complex has been extensively studied both experimentally and theoretically. However, there is still debate over the exact orientation of the water molecule at the global minimum and over whether a single or double hydrogen bond is being formed to the benzene ring. The two possible binding orientations for the water molecule to the benzene ring are shown in figure 5-4a and 5-4b. Zwier has reported calculations[75] and presented experimental evidence[74] in a recent paper that indicates preferential bonding of one hydrogen to the benzene ring to give the global minimum atop the benzene surface as seen in figure 5-4b. He also indicates a double minimum with a small potential barrier of 20-50 cm^{-1} for hydrogen "swapping". However, Bredas *et al.*[76] have performed ab initio calculations which indicate that the symmetric double hydrogen bond complex is more stable than the single hydrogen bond complex by .25 kcal/mol. However, it is also noteworthy to mention that both authors argue from experimental and theoretical results that the potential surface for mobility of the water molecule across the benzene ring is very flat. This flat potential gives rise to freedom of motion (tumbling, rotation) for the water molecule within the vicinity of the benzene surface. Furthermore, there exists experimental evidence for large amplitude motion of the water atop of the benzene ring giving rise to effective C_{6v} symmetry where both hydrogens are equilavent[78]

Single point energy calculations at the RHF/6-31G* level were performed for structures 5-4a and 5-4b at the experimental monomer (center of mass) separation distance of 3.32 A.[79] The oxygen position in H_2O was taken as an approximate center of mass for both orientations. The energy difference was found to be .68 kcal/mol in favor of 5-4a where both hydrogens of H_2O are directed toward the ring. Also the barrier to rotation of H_2O

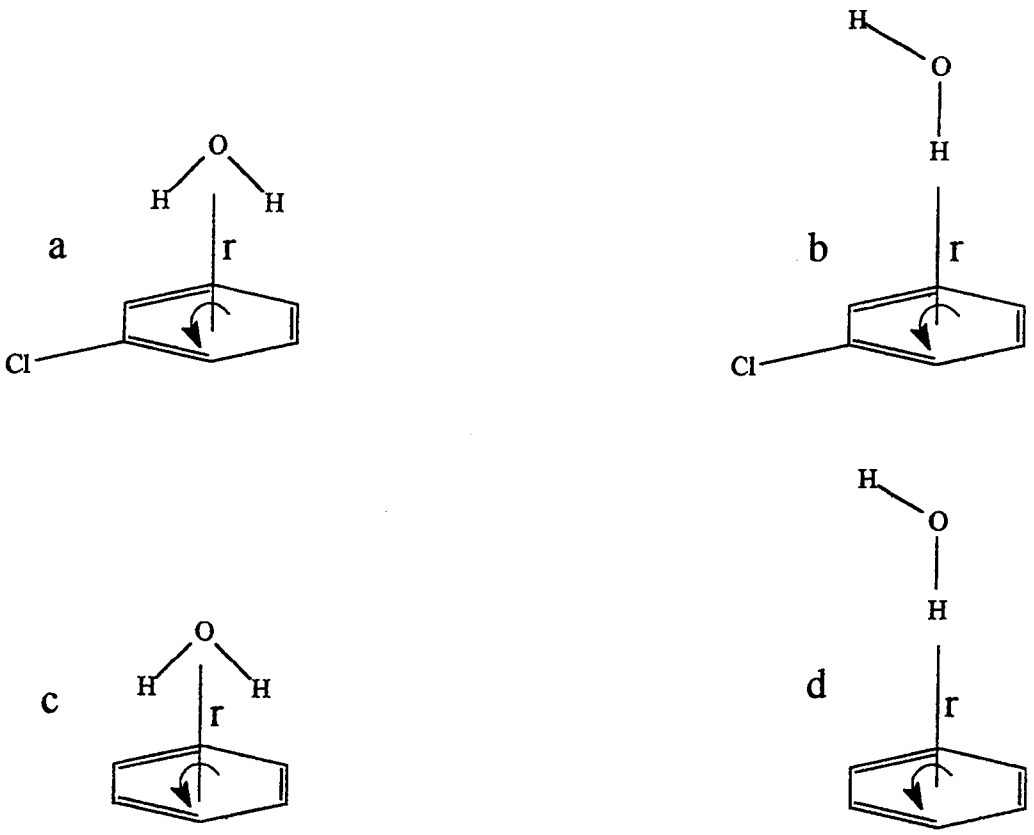

Figure 5-4. Orientational considerations for H_2O complexes with benzene and chlorobenzene.

along the center of mass coordinates was found to be essentially negligible in agreement with the computations by Bredas *et al.*[76]. MP2/6-31G* calculations were also performed for the optimization along the center of mass coordinate for the more stable geometry of figure 5-5a. Inclusion of electron correlation was shown to reduce the center of mass separation giving a distance of 3.26 Å which brings the value remarkably close to the experimentally observed mean separation.

The binding energy of the benzene-H_2O complex has been calculated at the RHF/6-31G* level of theory. The binding energy was found to be 1.605 kcal/mol. Inclusion of electron correlation at the MP2/6-31G*//RHF/6-31G* improves the binding energy to 2.210 kcal/mol. This value agrees quite well with the most recent experimental value for the dissociation energy of benzene-H_2O which is given by Cheng et al[77] and is 2.25 ± (.28) kcal/mol. The MP2 binding energy reported here does not include ZPVE(zero point vibrational energy), but this is expected to reduce the binding energy only slightly.

Chlorobenzene-H_2O geometry. Calculated values for the chlorobenzene-H_2O complex are shown in table 5-4. The complex geometry was investigated under RHF and MP2//RHF levels of theory with several basis sets at the constrained and unconstrained individual geometries. *Tight* convergence criteria was used for optimization to insure location of legitimate minima. Figure 5-5 shows the geometry of the fully optimized complex optimized under RHF/6-31G*. Considering the symmetry of the benzene-H_2O system, it seems reasonable to assume that the reduction of symmetry inherent in chlorobenzene should shift the binding site for H_2O due to an anisotropic distrubution of electron density relative to the center of the ring. Our calculations show that this is

Table 5-4. Calculated values for H_2O complexes with Benzene, Chlorobenzene, and Fluorobenzene at both the RHF/6-31G* and MP2/6-31G*//RHF/6-31G* levels of theory.

RHF/6-31G*	Benzene-H_2O	Chlorobenzene-H_2O	Fluorobenzene-H_2O
Separation (Å)	3.531013	3.633065	3.641632
Complex Energy (a.u.)	306.717920441	765.617087982	405.568506645
Aromatic Energy(bsse) (a.u.)	230.703981299	689.603888919	329.555295999
H_2O Energy(bsse) (a.u.)	76.0113807100	76.0111908967	76.0111991675
Total Binding Energy (kcal/mol)	1.605	1.260	1.262
MP26-31G*//RHF/6-31G*	Benzene-H_2O	Chlorobenzene-H_2O	Fluorobenzene-H_2O
Complex Energy (a.u.)	307.658291618	766.6901264805	406.6759941837
Aromatic Energy(bsse) (a.u.)	231.457840418	690.4904657732	330.4763061788
H_2O Energy(bsse) (a.u.)	76.196929885	76.19665840979	76.196672464125
Binding Energy kcal/mol	2.210	1.884	1.892

(13-14)=3.631151
(1-7) = 1.744106
(4-15) = 2.898242
(1-13-14) = 134.7489
(4-15-14) = 171.5244
(16-14-15) = 105.0001

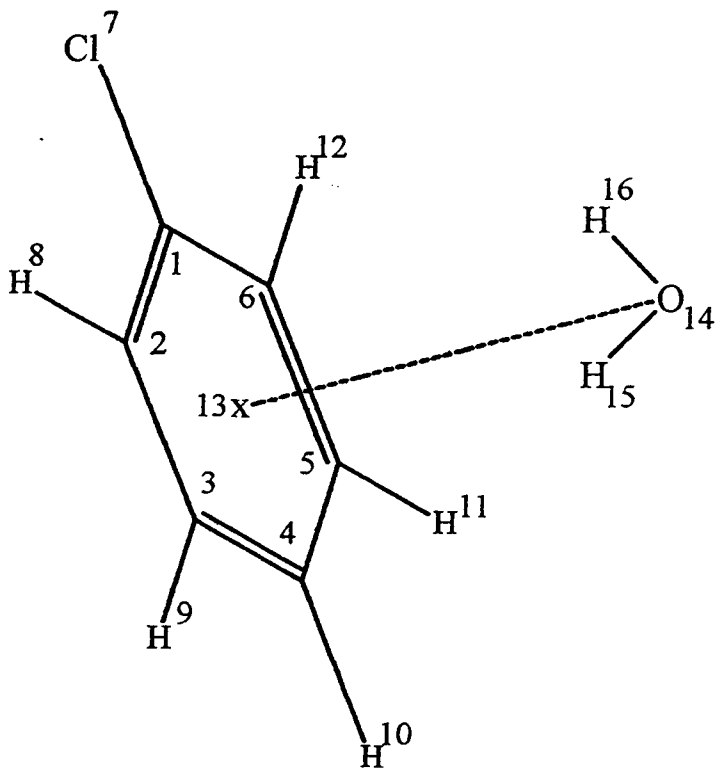

Figure 5-5. Fully optimized minimum geometry for chlorobenzene-H_2O calculated at RHF/6-31G*. Complex has C_1 symmetry.

indeed the case with asymmetric hydrogen bonding relative to the center of the ring. The H_2O molecule occupies a tilted position away from the axis perpendicular to the ring as shown in figure 5-5. The plane of the H_2O monomer bisects the plane of chlorobenzene perpendicularly. Interestingly, one hydrogen from H_2O is preferentially directed toward the para-carbon and the other is positioned over the top of the π ring. According to tentative interpretations of Mulliken population assignments, the para-carbon of chlorobenzene is consistently one of the more electronegative carbons for a number of basis sets and could be considered a preferred Lewis base site for electrophilic attachment. This geometric orientation for the complex could facilitate charge transfer between H15 and C4 in accord with hydrogen bonding interaction. It also suggests localized charge donation within the phenyl ring in contrast with the more symmetric delocalized benzene π donation. This preferred geometry introduces an interesting possibility. The hydrogen bond between H15 and C4 could be considered as having more σ character with charge transfer between the H15 1s atomic orbital and the C4 p_y atomic orbital (perpendicular to the phenyl ring).whereas the other hydrogen, being directed more toward the center of the phenyl ring, could be considered as more of a traditional π-bonded hydrogen bond.

The geometries for the two constituents in the complex are not substantially different from the individual monomers. The H-O-H angle shows the only substantial deviation from free monomer geometry and is reduced by .5 ° from the gas phase molecule.

Binding Energy. The binding energy of the chlorobenzene-H_2O complex has been calculated at the RHF/6-31G* level of theory (see table 5-4). Corrections for the basis set

superposition error (BSSE) were included by using the counterpoise method referred to in chapter 4. The binding energy at RHF/6-31G* for the complex is estimated to be 1.26 kcal/mol. Inclusion of electron correlation at the MP2/6-31G*//RHF/6-31G* level brings the total binding energy as 1.884 kcal/mol. These values are without zero point corrections, but ZPVE is expected to reduce these values only slightly. Although the chlorobenzene-H_2O complex has not been experimentally investigated, this value is not too far removed from the experimentally determined benzene-H_2O binding energy as would be expected.

For comparative purposes, the fluorobenzene-H_2O complex was also investigated. Calculated values for this complex are shown in table 5-4. Surprisingly, the binding orientation and energetics were very similar to the chlorobenzene-H_2O complex. The calculated center of mass separation for the fluorobenzene complex showed only a .01 Å increase from the chlorobenzene complex under the same basis set and hamiltonian. The binding energy was also found to be similar. The binding energy for the fluorobenzene-H_2O complex was determined to be 1.262 kcal/mol at the RHF/6-31G* level and deviates from the chlorobenzene complex binding energy to the nearest thousandths. Inclusion of electron correlation increased the binding energy to 1.892 kcal/mol which is also similar to the chlorobenzene-H_2O complex. The orientation of H_2O above fluorobenzene is very similar to the chlorobenzene complex. The binding properties of the fluorobenzene-H_2O and chlorobenzene-H_2O complexes relative to the benzene-H_2O complex are compared in the discussion section.

VIBRATIONAL ANALYSIS

Benzene. The normal modes of vibration for benzene have been calculated at the RHF/6-31G* level of theory and are shown in table 5-5 along with the experimental values. The numbering scheme for the vibrational modes are consistent with Mulliken notation. It is well known that vibrational frequencies calculated at the RHF level routinely give higher values than expected. To compensate for this overestimation, the usual practice is to scale[89] the frequencies by a factor of .89 to bring them closer to experimental values. As can be seen from the table, this provides reasonable estimates for the vibrational frequencies. However, the .89 factor generally fails for the higher frequencies characteristic of the C-H stretching mode. Errors in this region can sometimes be as high as 55 cm^{-1}, but the ordering of the modes remains consistent.

The benzene normal modes have been extensively investigated both experimentally and theoretically beginning with Wilson's influential paper[80] in 1934. A brief description (in terms of modeling considerations) of the normal modes will be given here to provide information for comparison with substitutional derivatives of benzene and for bimolecular complexes with benzene. For a detailed analysis of the modes, the reader is referred to Wilson's original paper.

The benzene molecule has D_{6h} symmetry and possesses 30 vibrational degrees of freedom of which 10 are degenerate giving 20 normal modes of vibration. Of the 20

Table 5-5. Calculated Vibrational Frequencies of Benzene RHF/6-31G*

No.	Sym.	Frequency (cm-1)	Adjusted Freq. (x.89)	Experimental[a]
ν_{20}	E_{2u}	453.4410	403.5625	410
ν_{18}	E_{2g}	665.5251	592.3173	606
ν_4	A_{2u}	764.8617	680.7269	673
ν_8	B_{2g}	777.0835	691.6043	703
ν_{11}	E_{1g}	961.7398	855.9484	849
ν_2	A_{1g}	1083.9867	964.7482	992
ν_6	B_{1u}	1096.5588	975.9373	1010
ν_{19}	E_{2u}	1100.5338	979.4751	975
ν_7	B_{2g}	1136.7075	1011.6697	995
ν_{14}	E_{1u}	1142.1639	1016.5259	1038
ν_{10}	B_{2u}	1197.2797	1065.5789	1150
ν_{17}	E_{2g}	1294.2915	1151.9194	1178
ν_9	B_{2u}	1351.6397	1202.9593	1310
ν_3	A_{2g}	1508.0647	1342.1776	1326
ν_{13}	E_{1u}	1652.1539	1470.4170	1486
ν_{16}	E_{2g}	1797.4670	1599.7456	1596
ν_5	B_{1u}	3348.3848	2980.0625	3068
ν_{15}	E_{2g}	3359.3540	2989.8251	3047
ν_{12}	E_{1u}	3377.7949	3006.2375	3063
ν_1	A_{1g}	3389.6593	3016.7968	3062

[a] experimental frequencies are from National Bureau of Standards [90]

normal modes, only 4 ($3E_{1u}$ and $1A_{2u}$) are IR active by selection rules. The calculated intensities of these IR active modes at the RHF/6-31G* level show the A_{2u} (ν_4) C-H bend mode to be the most intense followed by the E_{1u} (ν_{12}) C-H stretch at somewhat less intensity. The two E_{1u} modes of ν_{13} and ν_{14} are approximately a factor of 10 lower in intensity relative to the previous two.

There are 7 Raman active modes which consist of 2 A_{1g}, 1 E_{1g}, and 4 E_{2g}. The calculated highest intensity Raman active modes are the ν_1 (A_{1g}) C-H stretching mode and the ν_{15} (E_{2g}) C-H stretching mode. The calculated intensities at RHF/6-31G* contrasts with the relative intensities reported by the National Bureau of Standards[90] which indicate that the ν_2 A_{1g} (ring stretching,breathing) mode is of higher intensity than the ν_{15} mode. The remaining Raman active modes are the ν_{16} (Ring stretch), ν_{17} (C-H bend), ν_{18} (ring deformation), and ν_{11} (C-H bend) and are given in descending order of expected intensities.

There are two anomalies in the positions of the calculated frequencies when compared to the values observed experimentally. Both calculated B_{2u} frequencies are substantially shifted from the expected correction curve given by the .89 factor. The ν_9 (Ring stretch, Kekule) and the ν_{10} (C-H bend) modes are about 100 cm^{-1} lower than the experimentally observed values. These frequencies are inactive in both IR and Raman, but are weakly seen in the IR spectra of the liquid phase due to relaxation of selection rules in condensed phase systems.

It is interesting that upon recent literature investigation of the vibrational modes of benzene, it was found that the ν_9 B_{2u} mode is unique in other reports as well[91,92]. The ν_9 B_{2u} mode consists of non totally symmetric carbon stretches within the ring with very little inclusion of the hydrogen displacements as shown in figure 5-6. Haas *et al.*[91] have calculated the ν_9 fundamental in the ground state (S_o) and first excited state (S_1) at the CIS/6-31+G level of theory. Their value of 1231 cm^{-1} for the S_o ν_9 fundamental agrees reasonably well with our calculated value of 1203 cm^{-1} considering the difference in basis set (6-31+G as compared to our 6-31G*).

In a recent paper, Haas *et al.*[91] proposed to use the ν_9 (their ν_{14}) mode as a probe to resolve the ongoing debate of the role of π delocalization to the structure of benzene. It has been suggested (by them) that the π electrons tend to distort the benzene structure to a Kekule geometry (D_{3h}); whereas the traditional view dictates that the π electrons *stabilize* the benzene geometry by delocalization to give the highly symmetric D_{6h} structure. In the report by Haas *et al.*, it was indicated that the ν_9 mode in the $S_0 \rightarrow S_1$ transition ($1A_{1g} \rightarrow 1B_{2u}$) underwent an increase in its frequency in going from the ground state to the excited state. In contrast, all other vibrational modes showed a decrease in frequency upon excitation which is consistent with the relaxation of the benzene geometry upon entering the first excited state. They suggest that the increase in the ν_9 vibrational frequency upon excitation to the first excited state could be explained in the following

ν_9 normal mode (B_{2u})

Calculated frequency = 1203 cm^{-1}

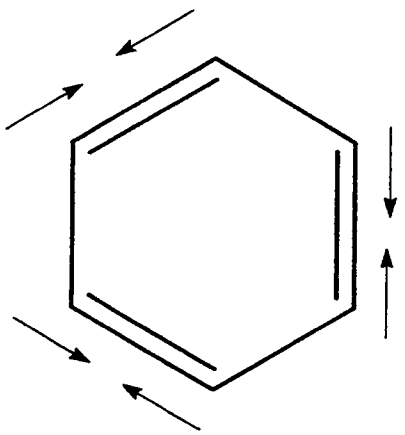

Figure 5-6. B_{2u} normal mode of vibration for benzene.

manner. They assume that the normal tendency for the π electrons is to distort the benzene structure to D_{3h} symmetry which is similar to the ν_9 B_{2u} deformation mode. Assuming a $\pi\pi^*$ transition for the first excited state, the promotion of an electron from a π bonding orbital to an antibonding orbital should reveal the σ bonding character of the ring and its influence on the carbon displacements of the ν_9 mode. They suggest a higher vibrational frequency for the ν_9 mode should result. However, their arguments seem to this author to strengthen the opposite view. If the π electrons are responsible for the distortion (D_{3h}) of the benzene ring (as they suggest), then a reduction of electron density from these bonding orbitals by excitation to an antibonding orbital should in fact result in a reduction of restoring power to the B_{2u} mode and a smaller frequency for the ν_9 fundamental and not a higher frequency as suggested by Haas *et al.* The fact that the ν_9 frequency is experimentally observed to increase suggests that π electrons act to counter the displacement of the ν_9 mode.

An interesting possibility inspired by the above arguments is the effect of complexation on the ν_9 normal mode of benzene with H_2O. The vibrational frequencies of the benzene-H_2O complex were calculated to investigate shifts in the ν_9 fundamental relative to uncomplexed benzene. It should be noted, however, that the isotropic interaction of H_2O with benzene and the large amplitude motion of H_2O atop of benzene render the vibrational calculations as suspect due to the harmonic approximation inherent in the calculations. The calculated value at the RHF/6-31G* level for the ν_9 normal mode in the benzene-H_2O complex was found to be 1207.3418 cm^{-1} which is only ~ 5 cm^{-1} higher than

the calculated value for the unperturbed benzene. However, both B_{2u} peaks showed an increase in frequency as expected based on the above arguments.

Several other modes showed substantial deviation in the complex relative to the free benzene. The lone A_{2u} mode of benzene at the calculated frequency of 681 cm^{-1} was found to increase by approximately 8 cm^{-1} upon complexation with H_2O. The A_{2u} mode of benzene is an out of plane mode and consists of all carbons going into the plane and all hydrogens displacing out of the plane in a symmetric manner. The only other noticeable shift in calculated frequency for benzene upon complexation with water was the symmetric hydrogen stretch (A_{1g}). This normal mode has a calculated value in free benzene at 3017 cm^{-1}. This mode was found to decrease by a substantial 27 cm^{-1} in the benzene-H_2O complex.

Chlorobenzene vibrational modes. The normal modes of vibration for chlorobenzene have been calculated at the RHF/6-31G* level of theory. Visual descriptions of the displacements of each normal mode are seen in figure 5-7. The calculated values as seen in table 5-6 are scaled by a factor of .89. The Mulliken notation is used for assigning the normal modes.

The coordinate system gives the C_2 axis of chlorobenzene parallel with the z axis and the plane of the molecule in the yz plane as shown in figure 5-7. C_{2v} chlorobenzene has 30 normal modes of which 11 are of A_1 symmetry, 3 are of A_2 symmetry, 6 are of B_1 symmetry, and 10 are of B_2 symmetry. As can be seen in table 5-6, the calculated modes, after scaling, are in reasonable agreement with the experimental values of Whiffen[93] and

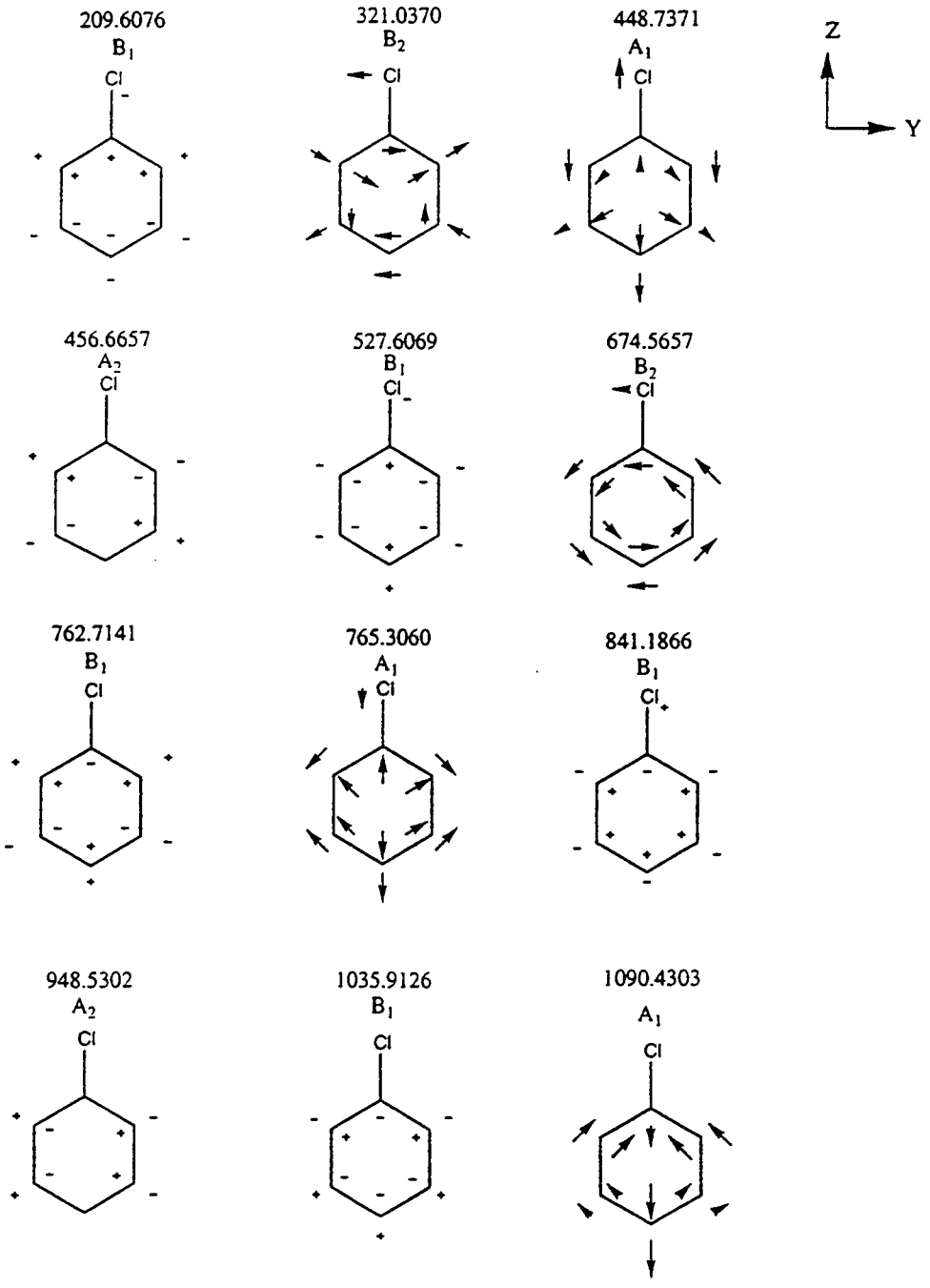

Figure 5-7a. Calculated normal modes of vibration for chlorobenzene at the RHF/6-31G* level of theory. Atomic displacements within each normal mode are shown.

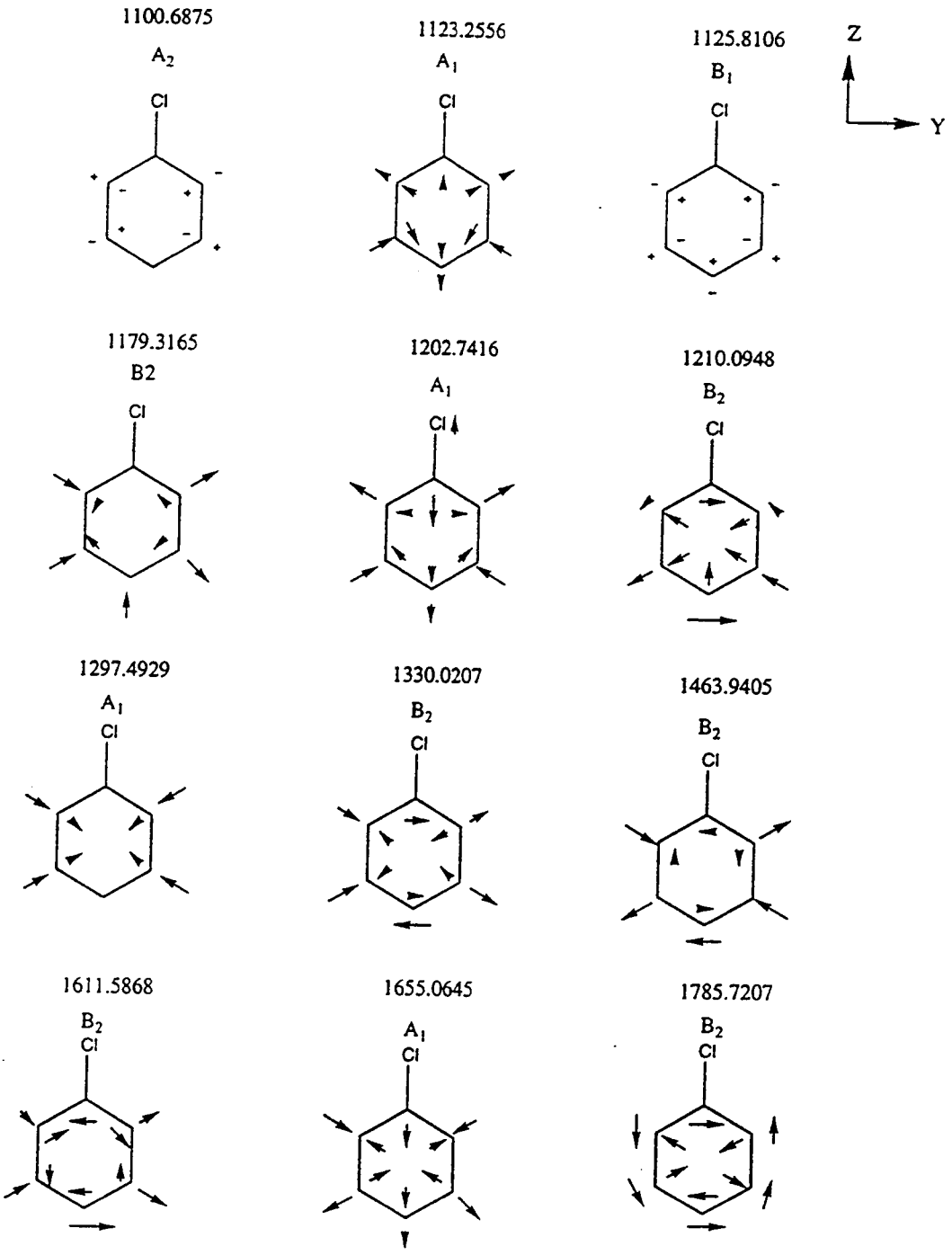

Figure 5-7b. Calculated normal modes of vibration for chlorobenzene at the RHF/6-31G* level of theory. Atomic displacements within each normal mode are shown.

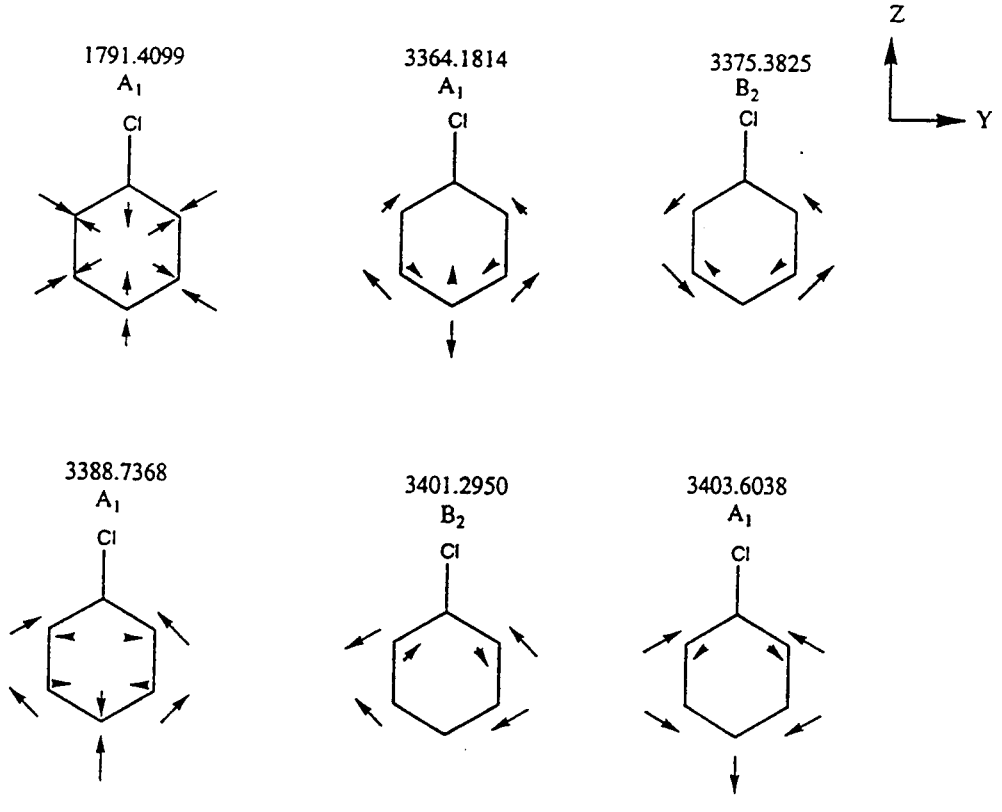

Figure 5-7c. Calculated normal modes of vibration for chlorobenzene at the RHF/6-31G* level of theory. Atomic displacements within each normal mode are shown.

Table 5-6. Calculated Vibrational Frequencies for Chlorobenzene at RHF/6-31G*

No.	Sym.	frequency (cm^{-1})	Adjusted frequency (x.89)	Experimental[a]
ν_{20}	B_1	209.6076	186.5508	196†
ν_{30}	B_2	321.0370	285.7229	294.8
ν_{11}	A_1	448.7371	399.3760	416.8
ν_{14}	A_2	456.6657	406.4325	400†
ν_{19}	B_1	527.6069	469.5701	467†
ν_{29}	B_2	674.5657	600.3635	614.8
ν_{18}	B_1	762.7141	678.8155	682†
ν_{10}	A_1	765.3060	681.1223	706.0
ν_{17}	B_1	841.1866	748.6561	740†
ν_{13}	A_2	948.5302	844.1919	832†
ν_{16}	B_1	1035.9126	921.9622	902†
ν_9	A_1	1090.4303	970.4830	1025.4
ν_{12}	A_2	1100.6875	979.6119	965†
ν_8	A_1	1123.2556	999.6975	1003.3
ν_{15}	B_1	1125.8106	1001.9714	985
ν_{28}	B_2	1179.3165	1049.5917	1068
ν_7	A_1	1202.7416	1070.4400	1092.0
ν_{27}	B_2	1210.0948	1076.9844	1157†
ν_6	A_1	1297.4929	1154.7687	1153
ν_{26}	B_2	1330.0207	1183.7184	1270.5
ν_{25}	B_2	1463.9405	1302.9070	1326
ν_{24}	B_2	1611.5868	1434.3123	1448
ν_5	A_1	1655.0645	1473.0074	1483
ν_{23}	B_2	1785.7207	1589.2914	1598
ν_4	A_1	1791.4099	1594.3548	1586
ν_3	A_1	3364.1814	2994.1214	3031
ν_{22}	B_2	3375.3825	3004.0904	3067
ν_2	A_1	3388.7368	3015.9758	3054
ν_{21}	B_2	3401.2950	3027.1526	3096
ν_1	A_1	3403.6038	3029.2074	3082

[a] experimental values are from Bist[94]. † values are from Whiffen[93].

Bist[94]. However, the C-H modes have proven difficult to model. The scaling factor of .89 does not seem sufficient for the calculated C-H fundamentals. This is similar to the calculated benzene C-H frequencies. The order of the C-H modes are however consistent with experimental assignments.

During the course of this investigation, it was found that Wilson's notation[80] for the benzene structure was still being applied to monosubstituted benzenes (chlorobenzene). Wilson's notation for benzene is consistent with D_{6h} symmetry where degenerate vibrational modes exist. However, for addition of a chlorine substituent to the ring, the degeneracy of the D_{6h} symmetry normal modes is removed upon C_{2v} formation. For example, the degenerate E_{2g} 6a and 6b vibrational modes (Wilson notation) of experimental frequency 606 cm^{-1} in benzene are split in chlorobenzene into ν_{11} (A_1) and ν29 (B_2) at experimental frequencies of 416.8 cm^{-1} and 614.8 cm^{-1} respectively.

A correlation diagram (Table 5-7) between Wilson's notation and our notation (Mulliken notation) was constructed to aid in assigning normal modes of chlorobenzene relative to the benzene structure. This was found to be a difficult and tedious task for two reasons. The *Gaussian 92* ab initio program is such that the coordinate system of the molecule is defined by the symmetry of the molecule with the highest principal axis being labeled the *z* axis. As such, the plane of chlorobenzene was placed in the *yz* coordinate plane to facilitate assignment of symmetry adapted basis functions. However, Wilson used a coordinate system with the C_2 axis of benzene on the *y* axis and the plane of the molecule in the *yx* plane. Also, the experimental values of the chlorobenzene vibrational modes by Whiffen was arrived by using the C_2 axis as the *z* axis with the plane of the

Table 5-7. Correlation Table ($D_{6h} \rightarrow C_{2v}$)

No.	⊗	Benzene D_{6h}[a]	Chlorobenzene C_{2v}[b]	No.
ν_{20}	16a 16b	403.5625(410) E_{2u}	B_1 186.5508(196†)	ν_{20}
ν_{18}	6a 6b	592.3173(606) E_{2g}	B_2 285.7229(294.8)	ν_{30}
ν_4	11	680.7269(673) A_{2u}	A_1 399.3760(416.8)	ν_{11}
ν_8	4	691.6043(703) B_{2g}	A_2 406.4325(400†)	ν_{14}
ν_{11}	10a 10b	855.9484(849) E_{1g}	B_1 469.5701(467†)	ν_{19}
ν_2	1	964.7482(992) A_{1g}	B_2 600.3635(614.8)	ν_{29}
ν_6	12	975.9373(1010) B_{1u}	B_1 678.8155(682†)	ν_{18}
ν_{19}	17a 17b	979.4751(975) E_{2u}	A_1 681.1223(706)	ν_{10}
ν_7	5	1011.6697(995) B_{2g}	B_1 748.6561(740†)	ν_{17}
ν_{14}	18a 18b	1016.5259(1038) E_{1u}	A_2 844.1919(832†)	ν_{13}
ν_{10}	14	1065.5789(1150) B_{2u}	B_1 921.9622(902†)	ν_{16}
ν_{17}	9a 9b	1151.9194(1178) E_{2g}	A_1 970.4830(1025.4)	ν_9
ν_9	15	1202.9593(1310) B_{2u}	A_2 979.6119(965†)	ν_{12}
ν_3	3	1342.1776(1326) A_{2g}	A_1 999.6975(1003.3)	ν_8
ν_{13}	19a 19b	1470.4170(1486) E_{1u}	B_1 1001.9714(985)	ν_{15}
ν_{16}	8a 8b	1599.7456(1596) E_{2g}	B_2 1049.5917(1068)	ν_{28}
ν_5	13	2980.0625(3068) B_{1u}	A_1 1070.4400(1092)	ν_7
ν_{15}	7a 7b	2989.8251(3047) E_{2g}	B_2 1076.9844(1157†)	ν_{27}
ν_{12}	20a 20b	3006.2375(3063) E_{1u}	A_1 1154.7687(1153)	ν_6
ν_1	2	3016.7968(3062) A_{1g}	B_2 1183.7184(1270.5)	ν_{26}
			B_2 1302.9070(1326)	ν_{25}
			B_2 1434.3123(1448)	ν_{24}
			A_1 1473.0074(1483)	ν_5
			B_2 1589.2914(1598)	ν_{23}
			A_1 1594.3548(1586)	ν_4
			A_1 2994.1214(3031)	ν_3
			B_2 3004.0904(3067)	ν_{22}
			A_1 3015.9758(3054)	ν_2
			B_2 3027.1526(3096)	ν_{21}
			A_1 3029.2074(3082)	ν_1

⊗Wilson notation.

[a]calculated values are adjusted(x.89) ; values in parenthesis are from National Bureau of Standards.

[b]calculated values are adjusted(x.89) ; values in parenthesis are from Bist ; † are from Whiffen.

molecule in the *xz* plane. This proved difficult in accounting and comparing the compilation of normal modes between the three sources. However, it was found that we could match the assignments of Whiffen's results by interchanging the B_1 and B_2 modes of our calculated frequencies. This facilitated comparison with Wilson's notation for the benzene modes.

The other difficulty was inherent in correlating the degenerate modes of benzene with the modes of chlorobenzene. It was found that the splitting of some of the degenerate modes in benzene by chlorine substitution was quite large. Some of the chlorobenzene frequencies assigned to the degenerate modes of benzene deviated substantially from the frequency of the degernate modes. Nevertheless, the frequencies of benzene were correlated to chlorobenzene based on expected intensities, selection rules, and atomic displacements. The latter method was quite useful in assigning the correlation due to the fact that a few of the benzene modes were unperturbed by substitution of the chlorine. However, the C-H modes proved especially difficult to assign, and the assignments given here are tentative.

Chlorobenzene-H_2O vibrational analysis. Vibrational frequencies for the chlorobenzene-H_2O complex have been calculated at the RHF/6-31G* level and are shown in table 5-8. In addition to the 30 normal modes of chlorobenzene, 9 new modes arise upon chlorobenzene complexation with H_2O of which 3 of these are essentially the normal modes of H_2O. The other 6 modes make up the intermolecular modes of the complex. The intermolecular modes are shown in figure 5-8. Although the frequency values were calculated for these modes, they should not be taken literally. The large amplitude motion

Table 5-8. Calculated Vibrational Frequencies for Chlorobenzene-H_2O Complex at RHF/6-31G*.

No.	Frequency(cm-1)	Adjusted Freq. (x.89)	Assignment[a]
ν_{39}	22.2159	19.7722	Cl sensitve bimolecular stretch
ν_{38}	28.1548	25.0578	Bimolecular planar bend
ν_{37}	65.5541	58.3431	Bimolecular stretch
ν_{36}	70.9851	63.1767	rotation about O-C4 axis
ν_{35}	121.5106	108.1444	rocking in the dihedral
ν_{34}	187.7484	167.0961	h2o planar waddle out of dihedral
ν_{33}	211.5155	188.2488	ν_{20} 186.5508 B_1 Chlorobenzene
ν_{32}	321.1242	285.8005	ν_{30} 285.7229 B_2 Chlorobenzene
ν_{31}	448.9265	399.5446	ν_{11} 399.3760 A_1 Chlorobenzene
ν_{30}	456.5422	406.3226	ν_{14} 406.4325 A_2 Chlorobenzene
ν_{29}	529.2968	471.0742	ν_{19} 469.5701 B_1 Chlorobenzene
ν_{28}	674.0831	599.9340	ν_{29} 600.3635 B_2 Chlorobenzene
ν_{27}	762.7394	678.8381	ν_{18} 678.8155 B_1 Chlorobenzene
ν_{26}	766.1276	681.8536	ν_{10} 681.1223 A_1 Chlorobenzene
ν_{25}	846.0353	752.9714	ν_{17} 748.6561 B_1 Chlorobenzene
ν_{24}	952.8383	848.0261	ν_{13} 844.1919 A_2 Chlorobenzene
ν_{23}	1039.5874	925.2328	ν_{16} 921.9622 B_1 Chlorobenzene
ν_{22}	1090.1518	970.2351	ν_9 970.4830 A_1 Chlorobenzene
ν_{21}	1105.3862	983.7937	ν_{12} 979.6119 A_2 Chlorobenzene
ν_{20}	1122.0351	998.6112	ν_8 999.6975 A_1 Chlorobenzene
ν_{19}	1128.0958	1004.0053	ν_{15} 1001.9714 B_1 Chlorobenzene
ν_{18}	1179.1282	1049.4241	ν_{28} 1049.5917 B_2 Chlorobenzene
ν_{17}	1203.0370	1070.7029	ν_7 1070.4400 A_1 Chlorobenzene
ν_{16}	1210.0685	1076.9610	ν_{27} 1076.9844 B_2 Chlorobenzene
ν_{15}	1297.8265	1155.0656	ν_6 1154.7687 A_1 Chlorobenzene
ν_{14}	1330.5094	1184.1534	ν_{26} 1183.7184 B_2 Chlorobenzene
ν_{13}	1463.9380	1302.9048	ν_{25} 1302.9070 B_2 Chlorobenzene
ν_{12}	1610.1477	1433.0315	ν_{24} 1434.3123 B_2 Chlorobenzene
ν_{11}	1653.3165	1471.4517	ν_5 1473.0074 A_1 Chlorobenzene

No.	Frequency(cm-1)	Adjusted Freq. (x.89)	Assignment[a]
ν_{10}	1781.9948	1585.9754	ν_{23} 1589.2914 B_2 Chlorobenzene
ν_9	1789.0607	1592.2640	ν_4 1594.3548 A_1 Chlorobenzene
ν_8	1832.6610	1631.0683	ν_2 1625.6377 A_1 H_2O
ν_7	3369.0994	2998.4985	ν_3 2994.1214 A_1 Chlorobenzene
ν_6	3380.4094	3008.5644	ν_{22} 3004.0904 B_2 Chlorobenzene
ν_5	3392.1498	3019.0133	ν_2 3015.9758 A_1 Chlorobenzene
ν_4	3403.9614	3029.5257	ν_{21} 3027.1526 B_2 Chlorobenzene
ν_3	3406.2301	3031.5448	ν_1 3029.2074 A_1 Chlorobenzene
ν_2	4073.1423	3625.0967	ν_1 3622.7156 A_1 H_2O
ν_1	4185.0427	3724.6880	ν_3 3727.9500 B_2 H_2O

[a] assignment frequencies are adjusted frequencies (x.89)

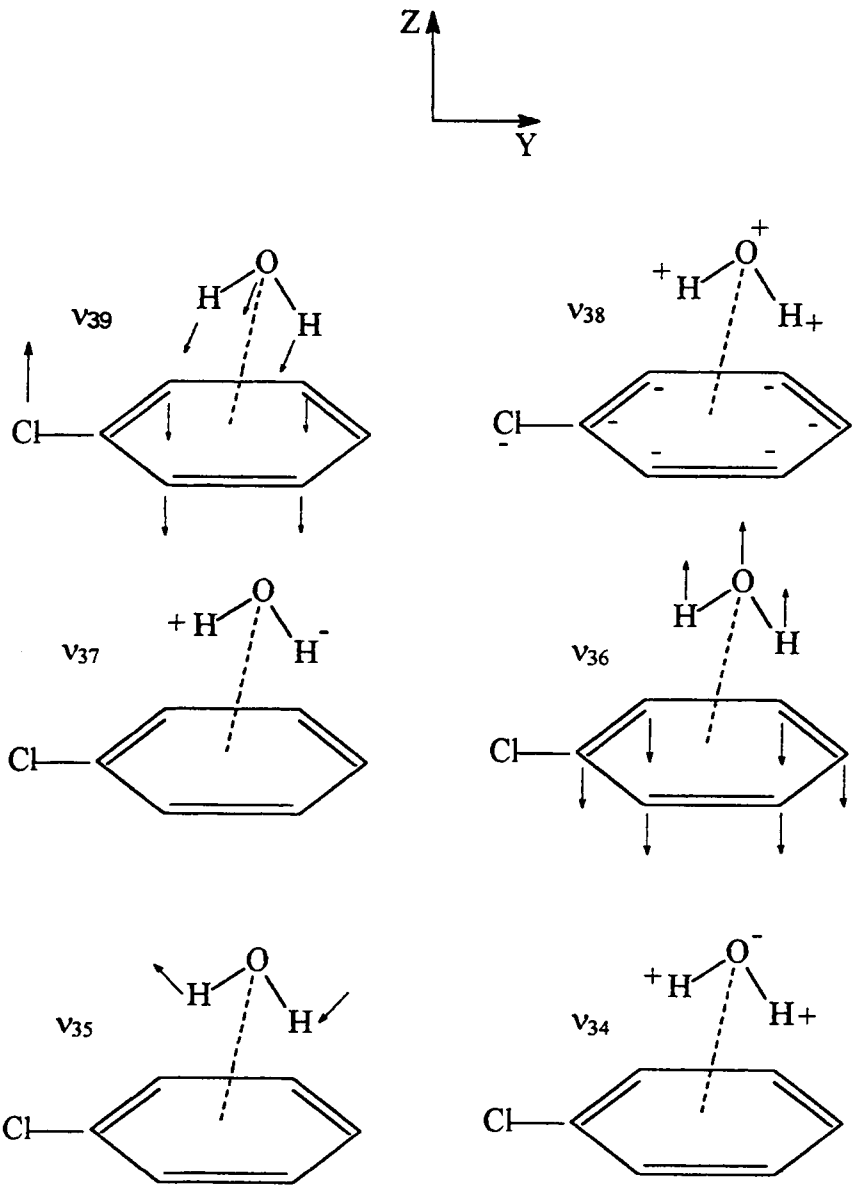

Figure 5-8. Intermolecular modes of the chlorobenzene-H_2O complex. The plane of the chlorobenzene ring is in the xy plane with the plane of the water molecule in the yz plane. The plane of the water molecule bisects the C_2 axis of chlorobenzene from a perpendicular direction.

of the intermolecular coordinates gives rise to anharmonicity which was not accounted for in our calculations. The complex frequencies in table 5-8 were calculated for the ground state of the fully optimized chlorobenzene-H_2O complex. Very little changes in the calculated frequencies for the individual monomers in the complex were found relative to the free monomers. This attests to the weak interaction between the two molecules and the negligible structural changes accompanying complex formation. For the chlorobenzene monomer in the complex, deviations in the vibrational frequencies were between 1 and 4 cm^{-1}. However, these slight shifts were used for binding comparisons and especially to verify correlation assignments between chlorobenzene and benzene.

14 modes representing the normal modes of the chlorobenzene monomer within the complex were observed to have no deviations greater than 1 cm^{-1} relative to free chlorobenzene. The remaining 16 modes showed deviations greater than 1 cm^{-1} but no larger than 5 cm^{-1}. Of these 16 modes that showed larger deviations, 12 modes were found to increase in frequency with the remaining 4 modes decreasing. The normal modes that decreased were v_5 (1471 cm^{-1}) and v_{24} (1433 cm^{-1}) of symmetry A_1 and B_2 respectively. These two modes are correlated to the v_{13} E_{1u} mode of benzene. The other two were v_4 (1594 cm^{-1}) and v_{23} (1589 cm^{-1}) of symmetry A_1 and B_2 respectively. These modes belong to a degenerate mode of benzene as well (v_{16} E_{2g}). Interestingly, the previous two degenerate benzene modes were found not to deviate at all when complexed to H_2O, yet the four daughter modes (v4, v5, v23, v24) of v_{13} E_{1u} and v_{16} E_{2g} were found to decrease in the chlorobenzene-H_2O complex. Large displacements in carbon 4 of chlorobenzene in the complex was the only correlation between the decreasing frequency

and v4, v5, v23, and v24 of chlorobenzene. This however, could support the possibility of the para carbon acting as a σ-hydrogen bond acceptor as a contributing bonding scheme.

An interesting observation was made for the 12 modes of chlorobenzene in the complex that were found to display an increase in frequency. All five of the C-H stretching frequencies (ν_1, ν_2, ν_3, ν_{22}, ν_{23}) were found to increase in frequency. The contribution of H_2O to the increase of these frequencies is not completely understood; however, it was observed that all C-H bond lengths in the complex gave a decrease in bond length although slight. This could indicate stronger C-H bonding giving an increase in the force constant. The other 7 modes of chlorobenzene (ν_{12}, ν_{13}, ν_{15}, ν_{16}, ν_{17}, ν_{19}, ν_{20}) that were found to increase in frequency had one thing in common. They were all out of plane displacement modes. Chlorobenzene, as well as benzene, has 9 out of plane modes. These out of plane modes are expected to show the deviation observed due to the ring displacements being parallel to the plane of the H_2O. The in plane modes of chlorobenzene would be expected to show the opposite trend as they are perpendicular to the plane of H_2O. This assumes of course that the electron density and therefore the force constants indicative of an in plane mode remain unchanged upon complex formation which is not entirely expected.

It was mentioned previously that complex formation of benzene with H_2O shows an increase frequency by approximately 5 cm^{-1} in the Kekule displacement modes ν_9 and ν_{10} for benzene. The corresponding modes in chlorobenzene are the ν_{28} and ν_{25} normal modes. Unlike benzene, the chlorobenzene Kekule modes were not found to deviate from

the free monomer value upon complexation with H_2O. This was an unexpected find at first. It was previously stated that π electron density donation from the benzene ring to the hydrogens of water resulted in weakening of the stabilization of the ring with a corresponding increase in the observed frequency of the Kekule mode. With this in mind, it was expected that the chlorobenzene complex would show the same observation. However, since the corresponding chlorobenzene Kekule modes do not deviate from their observed free monomer value, it seems reasonable to suggest that the chlorobenzene ring is donating electron density not from the π distribution, but from the σ orbitals. This also lends support to the possibility of H15 in H_2O participating in a σ-type hydrogen bond with the para carbon of chlorobenzene.

DISCUSSION

The ordering of the binding energies for the three complexes, benzene-H_2O, chlorobenzene-H_2O, and fluorobenzene-H_2O were unexpected. The classical approach would suggest that the dipole-dipole interactions of the chlorobenzene and fluorobenzene complexes would be larger than the dipole-induced dipole interaction of benzene-H_2O with the latter having the lower binding energy. The fact that benzene-H_2O has the higher binding energy suggests that the classical explanation is not a sufficient approach. This is not surprising considering the orientation of the individual molecules in the complexes. For example, the chlorobenzene dipole is approximately at an angle of between 60° and 90° with the H_2O dipole moment. At this geometry, dipole-dipole interaction is

unfavorable. Similar structures for fluorobenzene and benzene would indicate a likewise interaction.

Hydrogen bonding between the aromatic compounds and the H_2O molecule is the most likely interaction. For benzene, the water molecule approaches the ring symmetrically due to the D_{6h} symmetry of benzene. A double π-hydrogen bond is formed by electron density donation from the delocalized π orbitals to both hydrogens of the water molecule. However, for chlorobenzene and fluorobenzene, the electron density in the ring is not uniform. Tentative interpretation of Mulliken charge assignments for chlorobenzene indicates that the substituted carbon shows a decrease in electron density and the para-carbon has a substantial negative charge, whereas in benzene, all carbons have identical negative charges. Similar results were found for fluorobenzene as well.

The weaker binding energy could be attributed to a reduction in electron density within the ring due to electron-withdrawing effects by the halogen substituent. It is generally accepted that chlorine and fluorine have substantial electron withdrawing character via inductive σ pathways. However, they are also known to stabilize the ring by electron donation through the π orbitals. It stands to reason that the observed decrease in binding energy for chlorobenzene and fluorobenzene indicates that both substituents are greater electron withdrawers than donators which results in a net decrease in electron density to the ring. However, this does not explain the almost identical binding energies for the chlorobenzene and fluorobenzene complexes. Atomic chlorine and fluorine have dissimilar electron withdrawing capability. Based on the electronegativities of the two centers, the

fluorobenzene-H_2O complex would be expected to have a lower binding energy than chlorobenzene-H_2O. However, it could be argued that the similarities in the binding energy may be a result of a balanced attack by both substituents. For example, fluorine inductively withdraws electron density more efficiently than chlorine. However, chlorine is expected to donate electron density to the ring by π overlap to a larger extent than fluorine. It is possible that a balance between these two effects results in similar changes in the electron density of the phenyl ring relative to each constituent.

The intermolecular separations show a positive correlation with the binding energies. For the benzene-H_2O complex, the oxygen (considered the approximate CM) of water is calculated to be 3.53 A away from the center of the benzene ring at the RHF/6-31G* level. Likewise for the chlorobenzene and fluorobenzene complexes, the center of mass separations are 3.63 Å and 3.64 Å respectively. The larger separation for both the chlorobenzene and fluorobenzene complexes suggest less electron density in the ring to form the π-hydrogen bond in agreement with the above interpretations.

A possible explanation for the observed binding energies and orientations of the three complexes could be as follows.. Each constituent withdraws (to a greater extent than donation) electron density from the phenyl ring via inductive σ-channels. The loss of electron density from the ring would therefore be localized primarily to the sigma framework (p_z,p_x atomic orbitals). On the other hand, the perpendicular π atomic orbital (p_y) on the carbons, and especially that on the para-carbon, would be less affected by the reduction in electron density from the σ framework regardless of the withdrawing

substituent. This indifference exhibited by the p_y orbital to electron density loss in the ring could possibly account for two calculated observables: 1) the preferred geometry of H_2O above the substituted ring with one hydrogen preferentially directed toward the para-carbon in forming a σ-hydrogen bond, and 2) the relatively small difference between the water binding energies of the two substituted benzene rings.

An NBO analysis was performed on each complex to characterize the bond orbital contributions to the binding energy and structure. The analysis indicated that the electron density exchange was from the aromatic ring to the H_2O component in all the complexes. For the benzene-H_2O complex, charge density is transferred from a π bonding orbital (BD) on the benzene ring to an anti-bonding orbital (BD*) situated along the O13-H14 (see figure 5-3) and O13-H15 bonds of the water molecule. The charge exchange to these two BD* orbitals are found to be symmetric in accord with the structure. For the chlorobenzene and fluorobenzene complexes, the charge exchange was again from the π BD orbital on the phenyl ring to the BD* along the O-H coordinate of the water molecule. However, the charge transfer was preferentially toward the hydrogen of water (H15, see fig. 5-5) nearest the para-carbon of the substituted ring. As shown in table 5-9, the charge transfer to the water molecule is asymmetric in the substituted complexes with BD* (O13-H15) receiving the majority of the charge transfer. Also, the amount of charge transfer between the above bond orbitals was observed to increase with decreasing intermolecular separation. This could possibly explain the similarities in the chlorobenzene and fluorobenzene complexation energies and also the distinction of these two complexes

Table 5-9. Natural Bond Orbital analysis of the bimolecular complexes giving the occupancy of the specified bond orbital. The atomic nomenclature can be seen in figure 5-5. For fluorobenzene and chlorobenzene, H15 is nearest the para-carbon of the substituted ring. For benzene, the oxygen is labeled 13.

NBO	Chlorobenzene-H_2O	Fluorobenzene-H_2O	Benzene-H_2O
BD* O14-H16	.00013	.00017	.00107
BD* O14-H15	.00150	.00185	.00107
BD C2-C3	1.65874	1.67631	1.66175
BD C1-C6	1.68119	1.65717	1.66504
BD C4-C5	1.65940	1.66939	1.66501

from benzene-H_2O. However, a detailed description of why the water molecule preferentially approaches the para-carbon could not be deduced from the *NBO occupancy* distributions.. If σ-hydrogen bond formation occurs and is the dominating interaction, the more probable bonding scheme would be head-on overlap between the p_y orbital of C4 (para-carbon) and the BD* of O13-H15 which is predominantly centered on the hydrogen.

Chapter VI

CHLORINE ANION AND RADICAL COMPLEXATION WITH WATER

Complexation of either a chlorine anion or a chlorine radical with a single water molecule is investigated here at the ab initio level of theory. The focus of this chapter is to provide information on three fronts: 1) How does the interaction between a Cl radical and a Cl anion with a water molecule differ, and what are the bonding mechanisms involved? 2) Can the equilibrium constant for the chlorine radical complex with water and the monomer constituents be calculated, and if so, does it provide any information about the existing conditions of chlorine radicals in thin ice films at 90K? 3) And last, what are the theoretical structural properties of the H_2OCl^+ cation complex, which is believed to be a reaction intermediate for hydrolysis of chlorine nitrate adsorbed on ice particulates?

Complexation between a chlorine anion and a water molecule(s) have been well studied both experimentally and theoretically. However, a theoretical investigation of the bonding of the complex in terms of bond orbitals has not been reported. The H_2OCl^- anion complex is described here in detail only to provide comparative arguments for bonding differences between the anion complex and the radical complex. The gas phase complex between a chlorine radical and a water monomer, on the other hand, has not been investigated experimentally or theoretically to the author's knowledge. The H_2OCl^+ cation, however, has recently come under investigation as a potentially important reaction intermediate for conversion of chlorine reservoir compounds to photoactive species. A

theoretical investigation of this cation is attempted here, and the frequencies of the normal modes of vibration are compared to the experimental values.

H_2OCl^-

Geometry. The optimized complex between the chlorine anion and the water monomer is shown in fig 6-1. This structure is obtained at the RHF level with a 6-31+G* basis set. Very tight convergence criteria was used during optimization for the location of the minimum in the potential. The complex was investigated as a negatively charged singlet using RHF techniques, and a full optimization was performed with all variables linearly independent. Vibrational analysis on the complex gave all positive values for the vibrational normal modes as is required for a true minimum in the potential surface. The complex possesses a C_s symmetry where the chlorine is off center from the "apparent" C_2 axis of the water by 1.83 Å. The water geometry in the complex has changed substantially from the free monomer as calculated under the same basis set, and as a result, the C_2 symmetry axis is exaggerated. The reduction in symmetry of complexed water is due to preferential binding by the chlorine anion to one of the hydrogens. The oxygen-hydrogen bond distance for the hydrogen nearest the chlorine gives an increase in the bond length of 0.013 Å from the free monomer at 6-31+G*. The other oxygen-hydrogen bond distance is similar to the free monomer showing a deviation of 0.00038 Å. The H-O-H angle in the complex has decreased by 4.2° relative to the calculated value in the monomer. The chlorine anion distance from the oxygen of the water molecule is 3.31Å. This is consistent

H_2OCl^- Complex

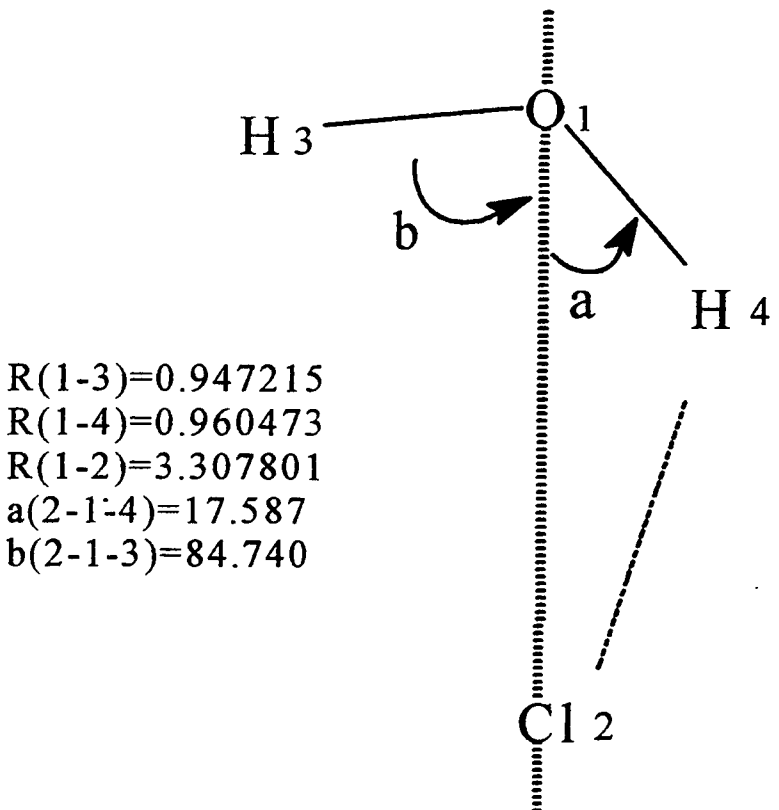

R(1-3)=0.947215
R(1-4)=0.960473
R(1-2)=3.307801
a(2-1-4)=17.587
b(2-1-3)=84.740

Figure 6-1. Calculated structure of the chlorine anion complex with H_2O at RHF/6-31+G*. Complex has C_s symmetry.

with the distances between complexes displaying van der Waals type interactions. The chlorine appears to be participating in a hydrogen bond with the centers (O1-H4---Cl2) as shown in figure 6-1. The H4-Cl2 distance is 2.41 Å and the O1-H4---Cl2 angle is 155.5°. The opposite hydrogen is 3.36 Å away from the chlorine.

Dipole. The dipole of the complex is given as 3.2532 D as compared to the calculated free monomer dipole of water as 2.2851 D with the 6-31+G* basis set. The complex dipole is oriented at 24.23° in the plane with respect to the oxygen-chlorine bond axis. The negative end of the dipole moment is located near the chlorine. The orientation of the dipole in the complex has changed sign and magnitude relative to the orientation of the free water monomer. The sign change can be attributed to the relatively large distance between the water and the chlorine anion. From strictly an electrostatic point of view, the hydrogens' close proximity to the oxygen diminishes the apparent negative charge on the oxygen with respect to the chlorine thereby effectively increasing the chlorine's contribution to the sign of the dipole. The total increase in the magnitude of the dipole is probably more attributed to the greater distance between effective charges and not necessarily a product of charge transfer between the chlorine anion and the water monomer.

Vibrational Frequencies. The normal modes for the H_2OCl^- complex have been calculated at the RHF level with a 6-31+G* basis set. The complex belongs to the C_s symmetry group and possesses 6 normal modes of vibration of symmetry A' or A". The calculated frequencies are given in table 6-1a along with the calculated frequencies for the free water monomer. The vibrational frequencies of the water molecule in the complex

Table 6-1a. Vibrational Frequencies (cm^{-1})* of H_2OCl^- complex and H_2O monomer at the RHF/6-31+G* level.

Frequency	H_2OCl^-	H_2O	Experimental[a]	Mode
ν_1 A' (ν_1 A_1)	3476.0335	3623.2655	(3825.32)	Symmetric stretch
ν_2 A' (ν_2 A_1)	1651.8366	1599.0169	(1653.91)	Bending
ν_3 A'	235.3342	---		Rocking of H_2O on Cl-O axis
ν_4 A'	136.7962	---		Complex stretch along Cl-O axis
ν_5 A'' (ν_3 B_2)	3684.8281	3729.2946	(3935.59)	Asymmetric stretch
ν_6 A''	624.9058	---		Planar distortion

* Calculated vibrational frequencies are corrected by a factor of (.89).
[a] Experimental frequencies for free H_2O were found in Herzberg and are in parenthesis.

Table 6-1b. Force constants(mDyne/Å) for H_2OCl^- Complex and H_2O monomer at the RHF/6-31+G* level.

Frequency	H_2OCl^-	H_2O
ν_1 A' (ν_1 A_1)	9.5144	10.2053
ν_2 A' (ν_2 A_1)	2.1935	2.0592
ν_3 A'	0.0426	---
ν_4 A'	.1121	---
ν_5 A'' (ν_3 B_2)	10.7979	11.2124
ν_6 A''	0.3098	---

has shifted substantially from the vibrational frequencies of the free water monomer for a similar basis set. The symmetric bending mode has blueshifted by 59 cm^{-1} relative to the free monomer. Likewise, there exist considerable shifts in the symmetric stretching and asymmetric stretching frequencies. These two stretching normal modes are redshifted, however, by 166 cm^{-1} and 50 cm^{-1} respectively. The changes in the symmetric and asymmetric stretching frequencies can be rationalized as being a product of contributions from changes in the force constants relative to changes in the reduced mass for each normal mode. Although chlorine is participating in hydrogen bond formation, the large distance from the water molecule effectively negates any contribution of the chlorine mass to the reduced mass of a particular normal mode in the water monomer. This essentially results in similar reduced masses contributing to the H_2O normal modes within the complex. As seen in table 6-1b, the largest contribution to the changes in H_2O frequencies within the complex stems from changes in the force constants for the H_2O's normal modes relative to the free water monomer. The symmetric bending mode shows a 6% increase in the force constant upon complexation with very little change in reduced mass. The force constant increase allows a blueshift in the bending mode relative to the free water monomer. Likewise, the redshift for both the symmetric and asymmetric stretching frequencies is attributed to a decrease in the force constant (7% and 3.5% respectively) for these normal modes with similar reduced masses.

Three new vibrational modes are the result of complexation between H_2O and the chlorine anion. The frequencies for these intermolecular modes are given in table 6-1a. These three vibrational modes have lower frequency relative to the intramolecular modes

of H_2O. Intermolecular modes in weakly bound complexes occur at lower frequency and large amplitude due to the flat curvature of the potential. The "intermolecular stretch" mode occurs in the far IR region at 137 cm^{-1} and is the lowest of the intermolecular mode frequencies. The stretching occurs along the Cl---O axis as shown in figure 6-2b. The next higher frequency at 235 cm^{-1} is shown in figure 6-2a. This mode represents an in-plane rocking motion along the Cl---O axis. Figure 6-2c shows the highest energy intermolecular vibration at 625 cm^{-1}. This mode represents a planar distortion of the complex with the hydrogens coming out of the plane and the chlorine and oxygen going into the plane. The IR intensities for these intermolecular modes have been calculated as well. While the absolute intensities are not to be taken as correct due to the harmonic approximation made in the calculation, the relative intensities could provide useful information. The intermolecular stretching mode was found to have the lowest intensity. Relative to this stretch, the rocking mode and the planar distortion have intensities that are six and fourteen times greater respectively. Experimentally, the planar distortion mode should be the more feasible mode to observe not only due to the higher intensity but also due to the more convient IR region where it occurs.

Energy. The ground state energy of the H_2OCl^- complex and the individual constituents are given in table 6-2. The energies for the complex and free H_2O represent the global minimums found for the fully optimized structures with the 6-31+G* basis set. The binding energy(E_b) for the complex is determined by

$$(6.1) \quad E_b = E_{complex} - (E_{H2O} + E_{Cl})$$

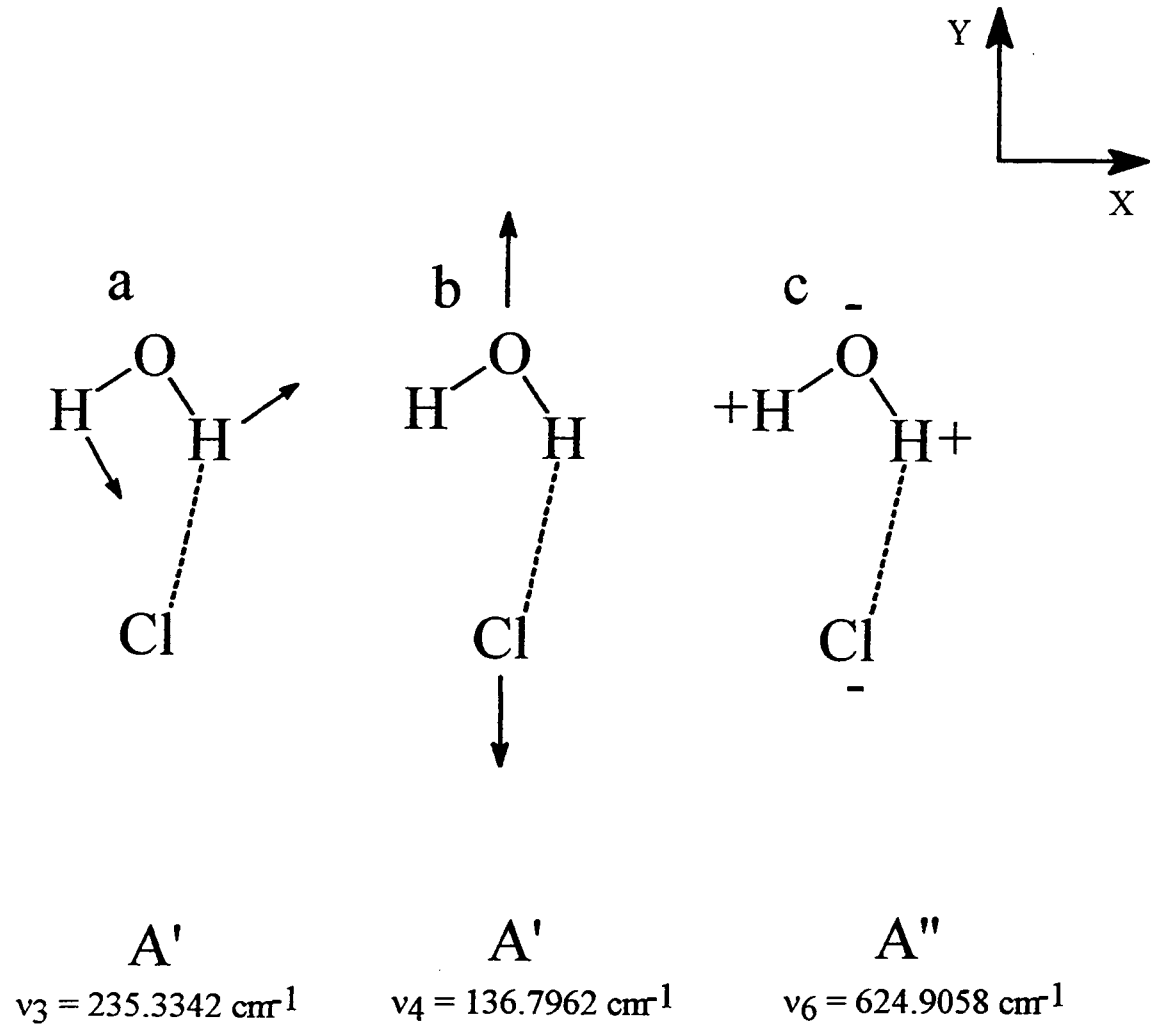

Figure 6-2. Vibrational displacements for the intermolecular normal modes of H_2OCl^-. Complex has C_s symmetry.

Table 6-2. Calculated values for the Chlorine anion-Water Complex(H_2OCl^-). The values were calculated at the RHF level with a 6-31+G* basis set.

Parameter	H_2O	H_2OCl^-	Cl^-
r(O1-H3) Å	.947596	.947215	---
r(O1-H4) Å	.947596	.960473	---
r(O1-Cl2) Å	---	3.307801	---
r(H4-Cl2) Å	---	2.409760	---
∠(H-O-H) (Degrees)	106.5222	102.327	---
∠(O1-H4—Cl2) (Degrees)	---	155.49	---
Dipole (Debye)	2.2851	3.2532	---
Polarizability (10^{-24} cm^3)	.874	---	1.956
Energy(a.u.)	76.017743172	535.577464159	459.539660881
BSSE[a] Energy(a.u.)	76.0180434176	---	459.539683646
ZPVE(a.u.)	.0229137	.0251104	---
Binding Energy[b] (kcal/mol)	---	11.0	---

[a]The BSSE corrections for H_2O are at the free monomer optimized geometry superimposed on the H_2O distorted structure within the complex.
[b]The binding energy includes the BSSE correction and the ZPVE correction.

The binding energy was corrected for basis set superposition error (BSSE) by using the counterpoise method.[73] The bsse correction for H_2O is at the 6-31+G* optimized free molecule geometry superimposed on the position of H_2O within the complex. Also, to arrive at a physically real binding energy, corrections for the zero point vibrational energy(ZPVE) were included. The ZPVE correction consisted of adding the zero point vibrational energies of the complex and the free H_2O to the corresponding total bsse corrected energies. The binding energy for the H_2OCl^- complex determined in this manner is 11 kcal/mol. The contributions from electron correlation were also considered. The geometries for H_2O and H_2OCl^- obtained at the RHF/6-31+G* level were used for a single point energy calculation at the MP2 level of theory which accounts for correlation effects. The values are given in table 6-3. The binding energy with electron correlation included was found to be 12.4 kcal/mol. This value is somewhat lower than the value calculated by Monte Carlo/ab initio methods[95] of 13.3 kcal/mol. However, the value calculated here is in reasonable agreement with the experimental value of 13.1 kcal/mol.[96] The validity of this calculated value rests on the assumption of calculating the second order energy correction (MP2) at the fixed geometry that corresponds to the order energy. To test the validity of this assumption, the complex and the free H_2O monomer were allowed to fully optimize in a MP2 calculation. The value obtained by this procedure for the binding energy of the complex was 12.1 kcal/mol. With only 0.3 kcal/mol difference, the previous assumption is within reason. The lower value for the fully optimized complex stems primarily from a greater energy minimum in the complex due to full optimization.

Table 6-3. Calculated values for the fully optimized H_2OCl^- Complex under MP2/6-31+G*

	H_2O	H_2OCl^-	Cl^-
r(O1-H3) Å	.970882	.970381	---
r(O1-H4) Å	.970882	.992977	---
r(O1-Cl2) Å	---	3.181430	---
H-O-H angle °	105.4686	101.6269	---
dipole (Debye)	2.3275	3.0543	---
Energy* a.u.	76.2087427051	535.903734387	459.6711453813
Energy** a.u.	76.2097765650	535.905483412	459.6711453813
Binding Energy[a] kcal/mol	---	12.4* ; 12.1**	---

* Energies are calculated with MP2/6-31+G* at the RHF/6-31+G* fixed geometry.
**Geometries are optimized under the MP2/6-31+G* to arrive at the energies.
[a] binding energies include bsse corrections and zpve corrections. The zpve value for free H_2O was calculated at RHF/6-31+G*. Zpve for the complex is found for each corresponding hamiltonian.

NBO Analysis. A natural bond orbital analysis[97] constructs bonding orbitals between atomic centers and gives the electron occupation for each. Shown in table 6-4 is the occupation of various bonding orbitals for the H_2OCl^- complex as a function of separation between the H_2O monomer and the Cl^- monomer. As can be seen from the values, the largest shift in occupation occurs within the anti-bonding orbital between oxygen and hydrogen (4) shown in figure 1. This hydrogen is closest to the chlorine anion and is considered to be contributing to hydrogen bond formation by charge transfer between the chlorine anion and the σ^* antibonding orbital on O1-H4. The electron acceptor (O1-H4) σ^* orbital is gaining electron density with increasing proximity between H_2O and Cl^-. The primary donating natural orbital is a lone pair (LP) situated on the chlorine anion. This donating orbital increases its capacity for donation with increasing proximity. The increase in the occupation of the σ^* orbital on the O1-H4 bond contributes to the destabilization of this bond and hence an increase in the bond length is observed relative to the O1-H3 bond length. The remaining natural bond orbitals as seen in table 6-4 show essentially no change in their occupation and therefore contribute very little to the interaction energy.

The stable geometry that is observed for the complex can be considered as dependent on the feasibility with which the hydrogen bond can be formed and hence on the orientation of which charge transfer is best achieved. The dependence of the total energy and charge transfer on the angles of interaction between the two monomers are shown in Tables 6-5a and 6-5b. These values were computed by using a trial geometry for the complex. The geometry for the complex is shown in Figure 6-3 (this is not a legitimate

Table 6-4. Occupation of Natural Bond Orbitals in H_2OCl^- complex as a function of monomer separation (R).

Natural Bond Orbital	R 2.7 Å	R 3.3 Å	R 4.0 Å
BD O1-H3	1.99966	1.99997	1.99993
BD O1-H4	1.99938	1.99981	1.99982
LP1 O1	1.99994	1.99995	1.99998
LP2 O1	1.99730	1.99958	1.99992
BD* O1-H3	.00052	.00027	.00009
BD* O1-H4	.08328	.01778	.00289
LP1 Cl^-	1.99999	2.00000	2.00000
LP2 Cl^-	1.99967	1.99997	2.00000
LP3 Cl^-	1.99945	1.99991	1.99998
LP4 Cl^-	1.91085	1.97999	1.99651

Table 6-5a. Charge occupation and energy for H_2OCl^- complex as a function of angle (α)[a]

Angle	0	10	20	30	40	50	60
BD O1-H2	1.99983	1.99985	1.99988	1.99992	1.99994	1.99991	1.99979
BD O1-H3	1.99983	1.99981	1.99981	1.99980	1.99980	1.99978	1.99972
LP1 O	1.99994	1.99994	1.99994	1.99994	1.99995	1.99995	1.99995
LP2 O	1.99990	1.99988	1.99980	1.99966	1.99942	1.99903	1.99850
BD* O1-H2	.00278	.00174	.00110	.00072	.00048	.00035	.00032
BD* O1-H3	.00278	.00450	.00736	.01212	.01996	.03246	.05112
LP1 Cl	2.00000	2.00000	2.00000	2.00000	2.00000	2.00000	2.00000
LP2 Cl	1.99999	1.99999	1.99999	1.99998	1.99995	1.99990	1.99993
LP3 Cl	1.99887	1.99906	1.99939	1.99964	1.99980	1.99989	1.99978
LP4 Cl	1.99511	1.99415	1.99130	1.98616	1.97762	1.96412	1.94424
Energy a.u.	535.57537324	535.57545966	535.57567948	535.57589824	535.57583672	535.57498041	535.57243003

[a] Angle considerations is shown in Figure 3. (BD)=bonding; (BD*)=anti-bonding; (LP)=lone pair

Table 6-5b. Charge occupation and energy for H_2OCl^- complex as a function of angle (β)[a]

Angle	0	20	40	60	80	100	120	140	160	180
BD O1-H2	1.99983	1.99984	1.99986	1.99987	1.99988	1.99989	1.99988	1.99984	1.99978	1.99976
BD O1-H3	1.99983	1.99984	1.99986	1.99987	1.99988	1.99989	1.99988	1.99984	1.99978	1.99976
LP1 O	1.99994	1.99995	1.99995	1.99993	1.99991	1.99989	1.99986	1.99986	1.99992	1.99997
LP2 O	1.99990	1.99976	1.99946	1.99919	1.99903	1.99897	1.99897	1.99907	1.99919	1.99923
BD* O1-H2	.00278	.00236	.00148	.00074	.00037	.00026	.00029	.00039	.00048	.00052
BD* O1-H3	.00278	.00236	.00148	.00074	.00037	.00026	.00029	.00039	.00048	.00052
LP1 Cl	2.00000	1.99999	2.00000	2.00000	2.00000	2.00000	1.99999	1.99998	1.99997	1.99997
LP2 Cl	1.99999	1.99999	1.99993	1.99986	1.99996	2.00000	1.99999	1.99998	1.99997	1.99997
LP3 Cl	1.99887	1.99907	1.99947	1.99980	1.99987	1.99995	1.99997	1.99996	1.99995	1.99994
LP4 Cl	1.99511	1.99583	1.99733	1.99854	1.99901	1.99892	1.99865	1.99834	1.99809	1.99799
RY* O1	.00009	.00010	.00016	.00030	.00050	.00072	.00092	.00106	.00114	.00117
Energy a.u.	535.5753732 4	535.5732754 9	535.5677205 2	535.560369 47	535.5528677 4	535.5464080 6	535.5416066 7	535.5385139 7	535.536858 99	535.536347 22

[a] Angle considerations is shown in Figure 3. (BD)=bonding; (BD*)=anti-bonding; (LP)=lone pair; (RY*)=Rydberg orbital

O1-H2 = .947596
O1-H3 = .947596
H-O-H = 106.5222
O1-Cl4 = 3.307801

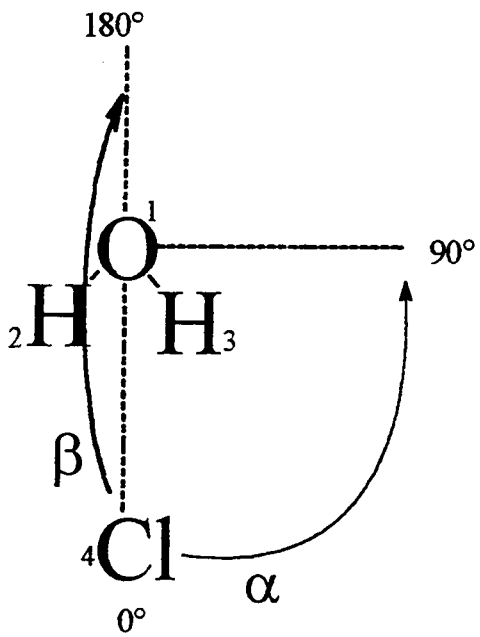

Figure 6-3. Trial geometry of H_2OCl^- complex for angle considerations.

minimum structure) along with the bond distances and angles used. The H_2O geometry within the trial complex is the minimum in the corresponding free H_2O geometry calculated with RHF/6-31+G*. The oxygen-chlorine distance is taken from the actual distance within the true minimum complex structure. One can see from table 6-5a that as the chlorine moves through the angle α, the charge transfer from a lone pair on chlorine to the anti-bonding orbital of O1-H3 increases monotonically through an angle of 60°. If charge transfer was the only criteria for choosing a geometry for optimum interaction, then it would be obvious why the chlorine anion chooses the one hydrogen over the more symmetric two hydrogen orientation. From table 6-5a, the total charge transfer (BD* O1-H2, BD*O1-H3) is more easily achieved for the chlorine anion attacking one hydrogen than for the chlorine attacking both hydrogens symmetrically. However, charge transfer cannot be the only complex stabilization occurring. The total energy in table 6-5a increases through ~35° but then decreases with increasing angle α. This indicates that the feasibility of charge transfer is not the only criteria for hydrogen bond formation and therefore complex stabilization. For the trial geometry in figure 6-3, it seems reasonable to assume that the chlorine is in an ideal geometry for ion-dipole interactions from a classical point of view. Movement of the chlorine through angle α at a fixed radius will decrease the classical interaction energy by $2\cos\alpha$ with a maximum at $\alpha=0$.

$$(6.2) \quad E_{classical} = (q\mu/4\pi\varepsilon_0 r^2) \times (1-2\cos\alpha)$$

where μ is the dipole of H_2O and q is the charge on the chlorine anion which is assumed here as one unit charge. Therefore, there appears to be a balance between the electrostatic

attraction and the charge transfer which results in the preferred asymmetric complex geometry shown in Figure 6-1.

H_2OCl

Geometry. The optimized stable geometry of the complex between a chlorine radical and a water monomer(H_2OCl) is shown in figure 6-4 along with calculated properties of the complex in table 6-6. Due to the open shell nature of this system, the complex was optimized at the Unrestricted Hartree Fock (UHF) level with a 6-31+G* basis set. The complex contains a C_s structure with the symmetry plane bisecting the H-O-H angle. Unlike the chlorine anion complex with water, the chlorine radical approaches the water monomer toward the oxygen. Assuming oxygen to be roughly the center of mass of the H_2O monomer, the chlorine radical shows a closer proximity to the center of mass than does the chlorine anion by ~ .3 Å under the same basis set(6-31+G*). The H_2O geometry within the complex shows very little distortion when compared to the free H_2O monomer for similar basis sets. With the 6-31+G* basis set, the O-H distance within the complex is only .00034 Å shorter than the free H_2O bond distance. Also, the chlorine radical complex possesses symmetric O-H bond lengths in contrast to the chlorine anion complex which displays asymmetric O-H bond lengths due to hydrogen bonding. The H-O-H angle within the radical complex is very similar to the H-O-H angle for the free water monomer giving a deviation of only 0.13°. The complex displays a tetrahedral like structure with the oxygen as the center and the chlorine radical occupying one of the lone pairs on the

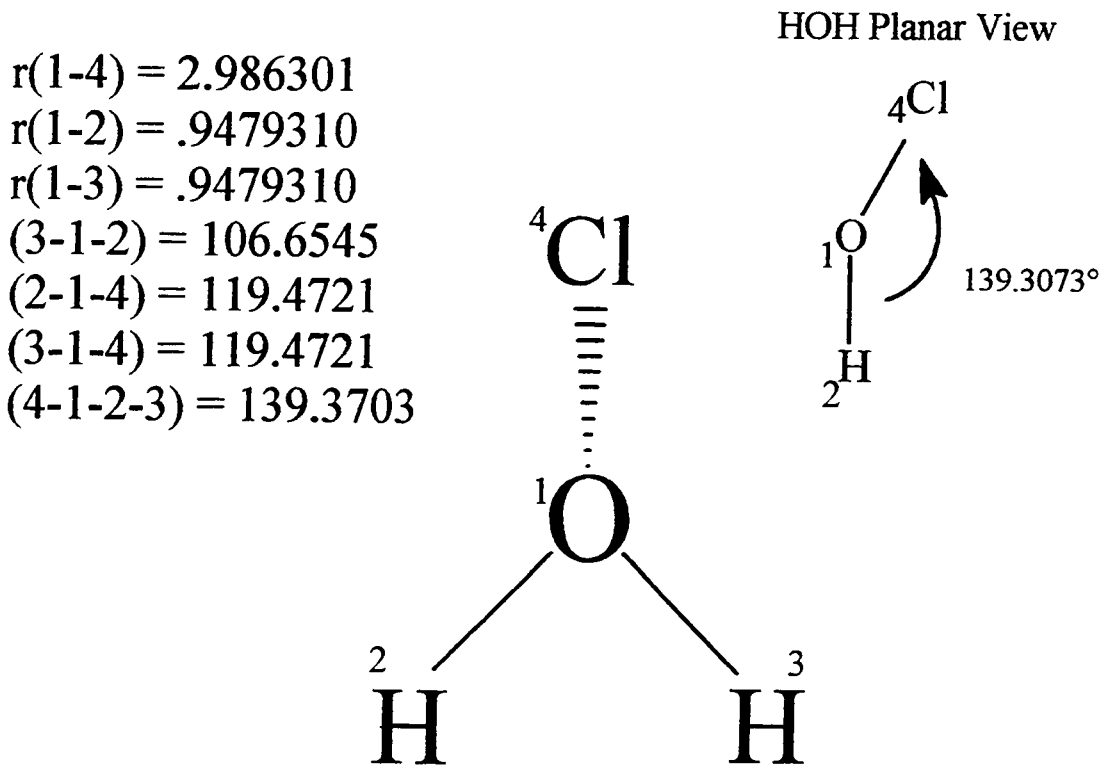

Figure 6-4. Geometry of the H_2OCl radical complex calculated at the UHF/6-31+G* level of theory. The structure has C_s symmetry.

Table 6-6. Calculated values for the Chlorine Radical-Water Complex (H_2OCl) using a basis set of 6-31+G* at the UHF level. Complex is C_s symmetry.

	H_2OCl	H_2O	Cl
r(O1-H2) Å	.947931	.947596	---
r(O1-H3) Å	.947931	.947596	---
r(O1-Cl4) Å	2.986308	---	---
∠ (H-O-H)	106.6545	106.5222	---
dihedral ∠ (Cl-O-H-H)	139.3703	---	---
Dipole (Debye)	2.4932	2.2851	---
Polarizability (10^{-24} cm^3)		.874	.990
ZPVE (a.u.)	.0236487	.0229137	---
Energy (a.u.)	535.469351596	76.017743172	459.448712078
Energy(BSSE) (a.u.)	---	76.0179083072[a]	459.448907400
Binding Energy (kcal/mol)	1.13[b]	---	---

[a]BSSE corrections for H_2O energy is made with the RHF/6-31+G* optimized geometry of the free H_2O superimposed on the complex.
[b]Binding energy includes ZPVE and BSSE corrections.

oxygen. As shown in figure 6-4, the chlorine makes an angle of 139.3° with the plane of the H_2O monomer at the 6-31+G* basis set. This angle, however, along with the Cl—O distance shows considerable deviation with basis set change as shown in table 6-7.

Optimizations which include electron correlation effects were also performed. The radical complex was optimized at the MP2 level of theory with a 6-31+G* basis set. The calculated values for the stable geometry are shown in table 6-8. The H_2O--Cl distance changed substantially from the UHF values. The Cl—O distance decreased by .3 Å from the UHF/6-31+G* structure. The planar angle (see figure 6-4) was optimized at 119° which is 20° smaller than the UHF value. An angle of 119° brings the structure more in line with a tetrahedral geometry. The O-H distance was found to increase with inclusion of electron correlation by .03 Å.

Dipole. The dipole of the radical complex is not expected to deviate from the free H_2O dipole as much as in the chlorine anion complex. The dipole for the radical complex was calculated to be 2.4932 Debye. This value is .21 D higher than the free H_2O dipole calculated under the same basis set. The orientation of the dipole remains essentially unchanged with respect to H_2O. Inclusion of electron correlation (MP2) to the calculations gives the dipole of the radical complex at 2.5842 D giving a difference of .09D. The higher MP2 value for the dipole is largely a result of increased O-H bond lengths for the MP2 optimized H_2O within the complex and not necessarily due to the chlorine interaction. Similar calculations on the free H_2O show an increase in the O-H bond distance and a corresponding increase in the dipole of .04 D.

Table 6-7. Calculated values for the H_2OCl radical complex with various basis sets.

	6-31G*	6-31+G*	6-311+G**	6-311++G**
Complex Energy (au)	535.4622566 43	535.4693515 96	535.5304658 12	535.5305719 41
Dipole (Debye)	2.3990	2.4932	2.4191	2.4137
O-Cl distance Å	2.952581	2.986308	3.012761	3.014444
O-H distance Å	.947761	.947931	.941486	.941480
H-O-Cl-H dihedral angle	116.967	139.3703	154.546	153.086
H-O-H angle	105.7401	106.6545	106.5420	106.5378
H_2O[a] Energy a.u.	76.01186472 92	76.01790830 72	76.05353368 85	76.05360781 22
Cl[a] Energy a.u.	459.4480721 65	459.4489074 00	459.4744088 17	459.4744445 08
E_b[b] Binding Energy kcal/mol	.836	1.13	1.16	1.15
ZPVE a.u.				
Complex	.0239628	.0236487	.0237062	.0237196
H_2O	.0229770	.0229137	.0230375	.0230399

[a]energies are corrected for BSSE

[b]Binding energy includes ZPVE (calculated from each basis set) and BSSE corrections

Table 6-8. Calculated values for Chlorine and H_2O radical complex with MP2/6-31+G*

	H_2OCl	H_2O	Cl
r (O-H) Å	.972249	.970882	---
r (O-Cl) Å	2.699902	---	---
∠ H-O-H	105.5642	105.4686	---
Dipole (Debye)	2.5842	2.3275	---
ZPVE a.u.	.0226291	.0212402	---
Energy a.u.	535.76944325585	76.210903945342*†	459.55551118341*
Binding Energy kcal/mol	1.03	---	---

* Energies are corrected for BSSE.

† BSSE correction for H_2O involved superimposing the MP2/6-31+G* geometry for free H_2O onto the complex and calculating the energy.

Vibrational Frequencies. The calculated vibrational frequencies for the radical complex are shown in table 6-9a. The frequencies were calculated at the UHF and MP2 levels of theory with a 6-31+G* basis set. The UHF (RHF for free H_2O) frequencies are corrected by a factor of .89. The H_2O frequencies within the complex show very little deviation from the free H_2O monomer frequencies. This is attributed to the small changes in geometry upon complexation with the chlorine radical. At the MP2 level, the H_2O frequencies within the complex again remain similar to the free H_2O frequencies for similar basis sets even though the chlorine-oxygen distance has decreased by .3 Å. This indicates very little perturbation introduced by complexation to the H_2O normal modes. The intermolecular modes (shown in figure 6-5) appear to be highly dependent on the method of calculation. The inclusion of electron correlation as mentioned previously draws the chlorine closer to the center of mass of the H_2O monomer. This is reflected in the changes in the vibrational frequencies of the intermolecular modes calculated at the MP2 level with respect to those calculated at the UHF level. The frequencies for the intermolcular modes increase substantially with inclusion of electron correlation as can be seen in table 6-9a. The higher frequencies are the result of increased force constants (shorter Cl—O distance) for the intermolecular modes (table 6-9b).

Energy. Table 6-7 gives the binding energy (kcal/mol) for the chlorine-H_2O radical complex as a function of various basis sets. The binding energy at UHF/6-31+G* is calculated to be 1.13 kcal/mol. The binding energy(E_b) was calculated as

$$(6.3) \quad E_b = E_{complex} - (E_{H2O} + E_{Cl})$$

Table 6-9a. Calculated Vibrational Frequencies for the Chlorine-H_2O radical complex

Frequency	UHF/6-31+G* H_2OCl[a]	MP2/6-31+G* H_2OCl	RHF/6-31+G* H_2O[a]	MP2/6-31+G* H_2O	Mode
ν_1 A' (ν_1 A_1)	3621.6704	3734.9819	3623.2655 (3825.32)[b]	3747.9007	Symmetric Stretch
ν_2 A' (ν_2 A_1)	1600.6410	1682.4996	1599.0169 (1653.91)	1681.8433	Bending
ν_3 A'	90.1257	247.1648	---	---	Symmetric Stretch along Cl---O axis
ν_4 A'	68.5017	125.7477	---	---	Planar Bend
ν_5 A'' (ν_3 B_2)	3726.5506	3878.9813	3729.2946 (3935.59)	3893.6521	Asymmetric Stretch
ν_6 A''	131.2333	263.6350	---		Planar Distortion

[a] Frequencies are corrected by a factor of (x.89).
[b]Experimental values for free H_2O were found in Herzberg and are in parenthesis.

Table 6-9b. Calculated Force Constants (mDyne/Å)

Frequency	H_2OCl (UHF/6-31+G*)	H_2OCl (MP2/6-31+G*)	H_2O (RHF/6-31+G*)	H_2O (MP2/6-31+G*)
ν_1 A' (ν_1 A_1)	10.1961	8.5841	10.2053	8.6441
ν_2 A' (ν_2 A_1)	2.0641	1.8073	2.0592	1.8056
ν_3 A'	.0148	.0463	---	---
ν_4 A'	.0061	.0463	---	---
ν_5 A'' (ν_3 B_2)	11.1968	9.6004	11.2124	9.6721
ν_6 A''	.0137	.0430	---	---

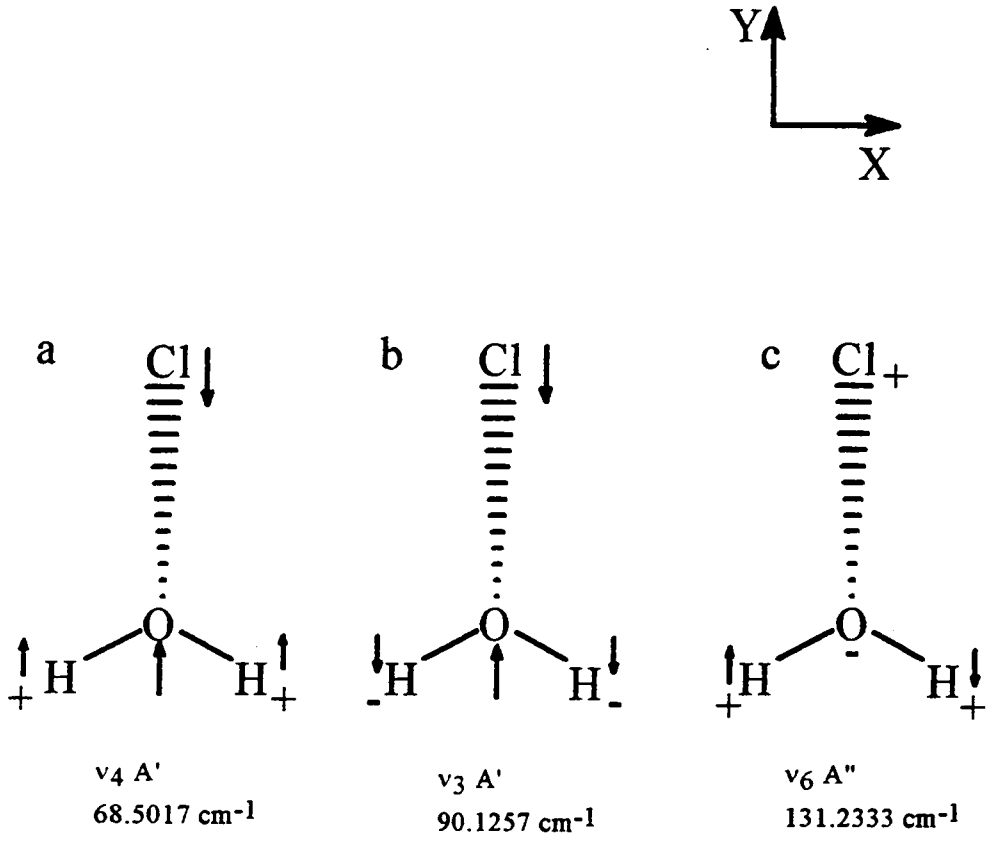

Figure 6-5. Vibrational displacements for the intermolecular normal modes of the H_2OCl radical complex calculated at UHF/6-31+G*.

where E_{H2O} and E_{Cl} are BSSE corrected energies. The energies for H_2O and the chlorine radical were corrected for basis set superposition error by the counterpoise technique. The BSSE corrected energy for H_2O was calculated by superimposing the free RHF optimized H_2O geometry onto the complex and removing the chlorine atom by setting its nuclear charge to zero. The superposition of the optimized free H_2O onto the complex is necessary to compensate for the distortion of H_2O within the complex. Equation 6.3 is more correctly written as

$$(6.4)\quad E_b = E_{complex} - (E_{H2O} + E_{Cl}) + (E'_{H2O} - E''_{H2O})$$

where E'_{H2O} and E''_{H2O} are non-BSSE optimized H_2O structures at the free geometry and the complexed geometry respectively. Superimposing the true H_2O geometry on the complex for the BSSE correction approximates the second term in equation 6.4. The error involved in the above approximation is minimal (to the nearest thousandths in the binding energy).

As can be seen in table 6-7, the larger basis sets give very little correction to the binding energy of the complex which reflects the small change in geometry for the higher basis sets. There is however a large difference in 6-31G* and 6-31+G* basis sets for the energies as well as the geometries. The diffuse functions appear to be necessary for adequate treatment of the radical complex. The values shown in table 6-7 indicate that the 6-31+G* basis set is probably the smallest basis set that can be used to arrive at reasonable binding energies and geometries.

The electron correlation effects on the binding energy of the radical complex were also investigated. The binding energy was determined at the MP2 level as 1.03 kcal/mol which

is similar to the UHF calculated values albeit smaller by .1 kcal/mol. This is a somewhat surprising result since electron correlation should normally increase the binding energy of weakly bound complexes, especially dipole-induced dipole systems, due to the addition of dispersion forces to the complex that accompany electron correlation. Also, the decrease in the chlorine—oxygen distance by inclusion of electron correlation would seem to indicate a more tightly bound complex. The lack of binding energy dependence on the electron correlation (dispersion forces) seems to indicate a more covalent rather than electrostatic binding mechanism.

NBO Analysis. The natural bond orbitals formed for the H_2OCl radical complex as a function of monomer separation are shown in tables 6-10a and 6-10b. Due to the open shell nature of the radical complex, the occupancy of the bond orbitals are split into Alpha and Beta spin. The primary bonding scheme for the complex can be attributed to charge donation from one of the oxygen lone pairs to the unfilled 3p orbital on the chlorine atom. From table 6-10b, the largest shift in charge density occurs with the loss of charge for the lone pair (LP2) on oxygen with an approximately equal amount of charge being gained by the unfilled lone pair (LP*) on the chlorine. This charge transfer becomes more pronounced with decreasing distance between the chlorine and oxygen centers. Also, as the Cl—O distances decreases, there appears to be back donation of charge from one of the lone pairs on chlorine (LP4) to an antibonding Rydberg orbital centered on the oxygen. With increasing proximity between the chlorine and the oxygen ($\leq$ 2 Å), a bonding orbital is formed between the chlorine and oxygen. The bonding orbital is primarily composed of the Cl 3p and the O 2p. This bonding orbital, however, is not

Table 6-10a. Occupation of natural bond orbitals in H_2OCl radical complex. **Alpha** Spin. Values are calculated as a function of monomer separation at the UHF/6-31+G* optimized geometry.

Natural Bond Orbital	R 2.386 Å	R 2.586 Å	R 2.786 Å	R 2.986 Å	R 3.186 Å
BD O1-H2	.99983	.99987	.99990	.99992	.99993
BD O1-H3	.99983	.99987	.99990	.99992	.99993
LP1 O1	.99986	.99990	.99992	.99993	.99996
LP2 O2	.99925	.99957	.99975	.99986	.99989
RY* O1	.000268	.00179	.00123	.00088	.00064
BD* O1-H2	.00095	.00053	.00030	.00018	.00011
BD* O1-H3	.00095	.00053	.00030	.00018	.00011
LP1 Cl	.99995	.99997	.99999	.99999	1.00000
LP2 Cl	.99971	.99987	.99994	.99997	.99999
LP3 Cl	.99969	.99982	.99990	.99995	.99997
LP4 Cl	.99595	.99744	.99834	.99888	.99923

BD=bonding; BD*=antibonding; LP=lone pair; RY* antibonding Rydberg orbital

Table 6-10b. Occupation of natural bond orbitals in H_2OCl radical complex. **Beta** Spin

Natural Bond Orbital	R 2.386 Å	R 2.586 Å	R 2.786 Å	R 2.986 Å	R 3.186 Å
BD O1-H2	.99915	.99949	.99970	.99982	.99987
BD O1-H3	.99915	.99949	.99970	.99982	.99987
LP1 O1	.99985	.99989	.99992	.99993	.99994
LP2 O2	.95921	.97804	.98858	.99408	.99690
RY* O1	.00013	.00009	.00007	.00005	.00005
BD* O1-H2	.00046	.00023	.00012	.00008	.00005
BD* O1-H3	.00046	.00023	.00012	.00008	.00005
LP1 Cl	.99995	.99997	.99999	.99999	1.00000
LP2 Cl	.99968	.99985	.99993	.99997	.99998
LP3 Cl	.99944	.99969	.99982	.99989	.99993
LP*Cl	.04211	.02271	.01181	.00611	.00318

realistic due to the nonstability of the complex at such close chlorine-oxygen distances. The energy for the radical complex with an O—Cl distance of 2.08 Å is 17.2 kcal/mol higher in energy than the stable O—Cl distance of 2.98 Å. This large increase in energy is not necessarily due to nuclear charge repulsions between the oxygen and the chlorine. On the contrary, stable compounds with O—Cl bonds are known. The ClO radical has a stable geometry at a separation of 1.62 Å (UHF/6-31+G*) and HOCl has an O-Cl distance of 1.67 Å (RHF/6-31+G*). The higher energy for the H_2OCl radical complex with a O-Cl distance of 2 Å is due primarily to destabilization of the O-H bonds by chlorine lone pair charge donation into the σ^* on the O-H bond.

The ionization potential (IP) for the H_2OCl radical complex was also calculated at the UHF/6-31+G* and MP2/6-31+G* levels of theory. The values for the vertical ionization potential were 13.4 eV and 12.3 eV respectively. Inclusion of the zpve calculated by each method for the ground state geometry lowered the values to 12.7 eV and 11.7 eV respectively. For comparison, the free H_2O vertical ionization potential was calculated. The value obtained at the MP2/6-31+G* level was 11.85 eV (ZPVE inclusive) which is lower than the experimental value of 12.6 eV. From the NBO analysis, the ionized electron appears to be localized entirely on the nonbonded lone pair on the H_2O.

DISCUSSION

The differences in interaction between H_2OCl^- and H_2OCl radical complex are considerable. The optimized geometry of each complex obviously reflects the preferred

interaction between the two monomers. In the anion complex, the interaction is primarily a contribution from two attractive terms: hydrogen bonding and electrostatic dipole-ion interactions. The calculated stable geometry for the anion complex is planar with the chlorine anion preferentially bonded to one of the H_2O hydrogens. The radical complex, on the other hand, is better described as arising from partial covalent bonding between the oxygen and the chlorine, and as a result, the optimized structure for the radical complex shows the chlorine interacting with one of the lone pairs of the oxygen. The bonding mechanism for both structures is crucial to interpreting the large differences in binding energy as a sum of electrostatics (i.e. dipole-ion, London dispersion forces), hydrogen bonding, or delocalization of charge by covalent bonding. However, it is difficult to separate the contributions as independent of each other. Hydrogen bonding is in fact an electrostatic interaction as well as a charge transfer interaction. The anion complex participates strongly in hydrogen bonding and forms a stable hydrogen bonded complex as shown in Figure 6-1. From the NBO analysis, the interaction at the stable separation consists of charge transfer from a lone pair on the chlorine anion to the σ^* antibonding orbital localized on the O-H bond. The charge transfer increases with decreasing separation between the hydrogen and chlorine anion until too much charge is introduced into the σ^* which destabilizes the whole complex, with a positive increase in total energy. The optimized separation defines the charge transfer contribution to stabilization of the complex and hydrogen bond formation. However, the electrostatic contribution is inherent in the charge transfer. The simple act of allowing charge to flow from one center to another induces an electrostatic force between the two centers. Actually, the

electrostatic attraction would be a necessary precursor to the formation of a hydrogen bond. This is the well known hydrogen bonding requirement of a hydrogen between two electronegative centers (N,O,F). The ability for charge transfer is greatly dependent on the separation between the two centers. The electrostatic attraction however has an r^{-2} dependence and falls off less rapidly than the charge transfer upon increasing separation. Therefore, the electrostatic attraction between the chlorine anion and the partial positive hydrogens would be the dominant interaction as the chlorine anion approaches the water molecule.

The H_2OCl radical complex does not show similar hydrogen bonding preferences. Optimization of the radical complex with the chlorine radical participating in hydrogen bonding was performed, and no minima under verytight convergence criteria were found. To provide information about the unfavorable energetics required for hydrogen bond formation with the radical, a single point energy calculation was performed on the anion complex structure previously shown figure 6-1. The anion complex structure was altered by replacing the chlorine anion with the chlorine radical. To simplify matters, the chlorine radical replaced structure is denoted as structure "A" and the chlorine anion complex is denoted as "B". The energy difference between this forced geometry, A, and the true (H_2OCl) radical complex geometry (not to be confused with structure B) calculated at similar levels (UHF/6-31+G*) was only 3.79 kcal/mol. An NBO analysis was performed on structures A and B and is shown in table 6-11. The charge transfer to the σ^*(O-H) on the water is less facile for the chlorine radical than for the chlorine anion. Occupation values for the σ^*(O-H) from table 6-11 give a total of .01168 for the chlorine radical

Table 6-11. An NBO analysis showing charge occupation values for the stable optimized chlorine anion complex (B) shown in Figure 1 and the complex with the chlorine anion replaced by the chlorine radical for the same geometry (A). Values calculated at RHF/6-31+G* (A) and UHF/6-31+G* (B).

Natural Bond Orbital	Structure A		Structure B
	α	β	
BD O1-H3	.99995	.99992	1.99997
BD O1-H4	.99988	.99986	1.99981
LP1 O1	.99993	.99994	1.99995
LP2 O1	.99991	.99979	1.99958
BD* O1-H3	.00006	.00007	.00027
BD* O1-H4	.00527	.00641	.01778
LP1 Cl	1.00000	.99999	2.0000
LP2 Cl	.99999	.99999	1.99997
LP3 Cl	.99997	.99270	1.99991
LP4 Cl LP*4 Cl	.99440	.00025	1.97999

complex (A) and .01778 for the chlorine anion complex under similar basis sets at the geometry of the optimized stable anion complex (B). All the other NBO's showed little perturbation in their values. Although the charge transfer is only slightly larger for complex B, it costs more energetically for the complex to donate charge density from an already half-filled subshell.

In the previous experimental chapter, it was suggested that chlorine radicals may be diffusing an ice medium. Complexation between H_2O and a chlorine radical could lead to the following equilibrium being established

$$(6.5)\quad H_2O + Cl \leftrightarrow H_2OCl$$

By calculating the thermodynamic equilibrium values ΔG, ΔH, and ΔS, an equilibrium constant K_{eq} can be obtained by the following equation.

$$(6.6)\quad \Delta G = -RT\ln K_{eq}$$

Calculation of the vibrational frequencies allows the determination of the enthalpy and entropy changes for reaction 6.5. The change in enthalpy (ΔH) at 298K and 1atm for complex formation is found to be -5.88 kcal/mol. ΔS is calculated to be 25.217 kcal/mol*K. Using the equation

$$(6.7)\quad \Delta G = \Delta H - T\Delta S$$

the Gibbs free energy for complex formation is found to be -19.336 kcal/mol. Inserting this value into equation 6.6 allows for the determination of the equilibrium constant at 298K. K_{eq} is found to be 5.84×10^{-15}. Such a small value indicates that the weak

interaction assumption made for the chlorine radicals in the ice matrix is reasonable, and at 90 K, the K_{eq} is expected to be lower due to a reduction in population of rotational and vibrational states of the complex.

H_2OCl^+

The hydrolysis of chlorine nitrate produces volatile hypochlorous acid and nitric acid consistent with the following reaction

$$(6.8) \quad ClONO_2 + H_2O \rightarrow HOCl + HNO_3$$

However, the exact mechanism in which reaction 6.8 occurs on the surface of the ice particulates in the stratosphere is still being debated. Several possible mechanisms have been proposed for the heterogeneous nature of the above reaction. It has recently been proposed that the H_2OCl^+ cation may act as an intermediate for reaction 6.8

$$(6.9) \quad ClONO_2 + H_2O \rightarrow [H_2OCl^+ \text{---} NO_3^-] \rightarrow HOCl + HNO_3$$

Sodeau *et al.*[18] investigated the photolysis of chlorine nitrate adsorbed to an ice surface and reported what they termed the first optical observation of the H_2OCl^+ cation. They give vibrational frequencies based on shifts in the H_2O fundamentals which they believe were consistent with the formation of H_2OCl^+ on the ice surface.

We present here ab initio calculations of the structure and properties of the H_2OCl^+ cation along with the normal modes of vibration. All calculations were performed using the Gaussian 92 suite of programs. Full geometry optimizations were carried out at the second order Moller-Plesset (MP2) level of theory for several basis sets. Frequency

calculations at the MP2 level with various basis sets were performed for H_2OCl^+ and H_2O using the harmonic approximation. This approximation is considered valid given the revealed covalent nature of the cation. The calculated normal modes are obtained by averaging the values found with the basis sets shown in table 6-12. These calculated frequency values are then scaled by a factor of 0.95. Adiabatic and vertical electron affinities (EA) were calculated by determining the difference in total energy between the H_2OCl^+ cation and the relaxed and constrained neutral H_2OCl complex respectively. Zero point energies were not included in the EA values. Orbital occupations and charge assignments were determined by the Natural Bond Orbital method.

The calculated minimum geometry of the H_2OCl^+ cation is shown in figure 6-6. The chlorine is bound to the oxygen of the water molecule through one of the lone pairs to give a pseudo-tetrahedral arrangement. The calculated chlorine-oxygen separation with the 6-311++G** basis set is 1.75 Å and is very similar to oxygen-chlorine covalent interaction observed in other compounds such as OCl_2 and HOCl. The similarities in the bond lengths suggest that the oxygen-chlorine bond in H_2OCl^+ is covalent. Calculations of the ionization scheme of the neutral H_2OCl tend to support this conclusion. The neutral H_2OCl molecule shows a much larger O-Cl separation with a value of 2.70 Å at the calculated minimum geometry and is indicative of van der Waals bond formation. Very little perturbation to the structure of H_2O is found upon neutral complexation with the chlorine radical. Natural bond orbital analysis of the neutral H_2OCl molecule indicates that the interaction along the O-Cl coordinate is mostly charge donation from a lone pair (LP) on the oxygen to an unfilled lone pair (LP*) centered on the chlorine. However,

Table 6-12. Calculated values for H_2OCl^+ cation as a function of basis set at the MP2 level of theory. Cation has C_s symmetry. The polarizability values are given in units of $Å^3$ as tensor coordinates of xx, yy, and zz respectively. The average polarizability is given in parentheses. Both vertical (V) and adiabatic (A) electron affinities are given in units of eV. Dipole moments are calculated in Debye.

parameter	6-31+G*	6-31+G**	6-31++G**	6-311++G**
O-H Å	.997644	.987562	.987573	.982311
O-Cl Å	1.761530	1.758408	1.758393	1.754914
H-O-H °	109.2848	110.2370	110.1879	109.5145
H-O-Cl °	109.3332	109.9871	109.9162	111.0162
Energy a.u.	535.41451898603	535.43416312623	535.43457976449	535.50439681094
Polarizability	3.223, 1.695, 1.489, (2.136)			3.225, 1.707, 1.522, (2.151)
Electron Afinity (EA)	V 7.467 A 9.654	7.469	7.469	7.488
Dipole	4.094			3.6011

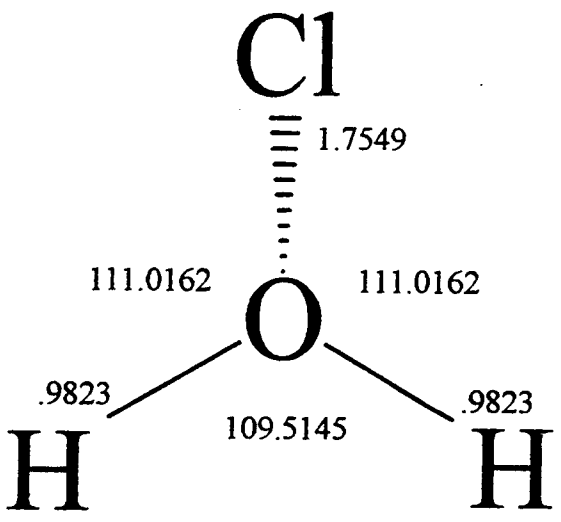

Figure 6-6. Optimized geometry of the H_2OCl^+ cation at the MP2/6-311++G** level of theory. Cation possesses C_s symmetry. The chlorine dihedral with the H-O-H plane is 122.9401°.

analysis of the bond orbitals for the cation show that the O-Cl bonding scheme is primarily due to overlap of the O_{2p} and Cl_{3p} atomic orbitals resulting in an increased interaction along the O-Cl coordinate relative to the neutral molecule with formation of σ type bond. Significant perturbations to the structure of H_2O occur upon formation of the cation with an H-O-H angle increase of ~ 5 ° relative to the neutral H_2OCl molecule. The increase in the H-O-H angle along with a decrease in the O-Cl bond length constitute the major structural changes of the cation while the O-H bond lengths show an increase of only ~ 0.025 Å. With such pronounced changes in structure upon ionization of the neutral compound, a considerable difference between the vertical and adiabatic electron affinities of the cation is expected and observed (see table 6-12). The average vertical and adiabatic electron affinities calculated for the various basis sets show that the vertical EA of the cation is approximately 2.2 eV lower than the adiabatic EA of the cation.

The calculated vibrational frequencies for the H_2OCl^+ cation are shown in table 6-13 along with calculated and experimental values for the neutral H_2O molecule for comparative purposes. The normal modes calculated here are indicative of gas phase values and are not directly comparable to the vibrational frequencies determined from adsorbates on an ice surface as given by Sodeau *et al.*, but the relative positioning and intensities of the calculated normal modes could facilitate assignment. The H_2OCl^+ cation possesses C_s symmetry and has 6 normal modes of vibration of which 4 are of A' symmetry and 2 are of A" symmetry. All modes are IR active and Raman inactive in the gas phase, however, under the experimental conditions of Sodeau *et al.*, a relaxation of the selection rules is expected due to solvation effects. Both the symmetric and asymmetric

Table 6-13. Calculated vibrational frequencies for H_2O and H_2OCl^+ at the MP2 level of theory. Experimental values for H_2O were collected from Herzberg.

Normal mode	H_2O experimental (cm^{-1})	H_2O calculated (cm^{-1})	H_2OCl^+ calculated (cm^{-1})
A' ν_1	(A1) 3657 ν_1	(A1) 3637.48 ν_1	3358.02
A' ν_2	(A1) 1595 ν_2	(A1) 1585.03 ν_2	1560.91
A' ν_3	---	---	838.05
A' ν_4	---	---	647.23
A" ν_5	(B2) 3756 ν_3	(B2) 3774.14 ν_3	3456.03
A" ν_6	---	---	1019.31

O-H stretches for the H_2OCl^+ cation show a reduction in the calculated frequency relative to the frequencies calculated for the free H_2O molecule under similar levels of theory. The lower frequencies are attributed to a reduction in the force constants along the O-H bond for both stretching modes relative to the free H_2O monomer. The lower force constants are also evident in the larger O-H bond lengths observed for the cation and are attributed to charge donation from a LP orbital on chlorine to the antibonding sigma orbital (BD*) along the O-H coordinate. Although the reduction in the O-H stretching frequencies is primarily the result of intramolecular processes, an added reduction is expected for intermolecular interactions consistent with the cation acting as a hydrogen donor for hydrogen bond formation. This is expected to lower the O-H stretching frequency to a value similar to the value reported by Sodeau ($3300cm^{-1}$).

The H-O-H bending mode for the cation is less affected by the chlorine substituent. The calculated value for this mode in the cation is only 25 cm^{-1} lower than the calculated value for the bending mode in the free H_2O molecule and is probably subject to the limits of the calculation. Like the stretching modes, the bending mode is expected to deviate from the gas phase value upon intermolecular solvation by hydrogen bonding. However, unlike the stretching modes, the bending mode is expected to show an increase in frequency and intensity upon hydrogen bond complexation. Sodeau's tentative assignment of 1650 cm^{-1} to the H-O-H bending mode is considered reasonable and agrees with the above expectations.

The fundamental stretching mode along the O-Cl coordinate is calculated to occur at 647 cm^{-1} and is consistent with experimentally observed O-Cl stretching frequencies for

OCl_2 (639 cm^{-1}) and HOCl (725 cm^{-1}). The intensity for this mode is calculated to be 2 to 3 times smaller than the intensity of the H-O-H bending mode within the H_2OCl^+ cation. Sodeau *et al.* report that they were not able to determine the O-Cl stretching mode due to limitations to the IR detector with a sensitivity cutoff of 700 cm^{-1}. However, it is expected that intermolecular interactions will reduce the calculated fundamental stretching frequency further from the value stated above.

Two other fundamental modes are calculated due to the H_2OCl^+ cation formation. These modes, ν_3 and ν_6, are separated by ~ 180 cm^{-1} and appear in a more feasibly observable region of the spectrum. The higher mode at approximately 1019 cm^{-1} consists of an asymmetric scissoring of the hydrogens relative to the oxygen-chlorine position. This fundamental is calculated to have a relatively low intensity. The lower frequency mode at approximately 838 cm^{-1} , however, shows a significant intensity relative to the other fundamentals and is expected to be a visible integral of the spectrum. This mode consists of a symmetric bending motion of the H_2O plane relative to the chlorine position. These modes were not identified by Sodeau *et al.* in their spectrum. However, their identification of some of the nitrate ion fundamentals in this region of the spectrum suggest that higher resolution may be required for positive assignment of ν_3 and ν_6.

CONCLUSION

An investigation of chlorobenzene adsorbed to ultra-thin films of amorphous ice under UHV conditions has been discussed in this volume. Thin films of ice were grown on a Ni (111) substrate at 10^{-10} torr and at temperatures < 100 K. These layers of ice were found to be continuous and free from large fissures which might allow the parent adsorbates to reach the surface of the nickel substrate. Various coverages of chlorobenzene on ice were explored. For all coverages, chlorobenzene was found to adsorb reversibly to the ice surface. No thermal dissociation of chlorobenzene was observed at temperatures less than the desorbing temperature of ice ~ 160 K. Upon broadband UV irradiation of the sample, chlorobenzene was shown to photolytically dissociate along the carbon-chlorine bond to produce phenyl and chlorine radicals. The sole photoproduct desorbing from the surface of the ice during the TDS studies was benzene. A study using deuterated chlorobenzene indicates that benzene forms preferentially on the surface of ice by hydrogen abstraction of an adjacent chlorobenzene species by the phenyl radical. No chlorine containing species were found to desorb from the surface of the ice after irradiation. An Auger spectrum taken of the system after irradiation and thermal desorption showed atomic chlorine adsorbed to the nickel. Furthermore, XPS studies of irradiated samples of chlorobenzene adsorbed to ice give two chlorine 2p signatures which we believe are consistent with one species existing as chlorine adsorbed to the ice surface in the form of chlorobenzene and the other species as atomic chlorine below the ice surface adsorbed to the nickel surface.

The interactions of chlorine and to a lesser extent organochlorine compounds with the surface of ice was the primary objective of this research. We conclude, based on the discussions in this work, that atomic chlorine does not interact with the ice matrix to any appreciable extent. No observable indication of chlorine reactivity with the ice films could be found from the experimental work. The theoretical investigations of the H_2OCl radical indicate that this van der Waals complex is weakly bound and that very low concentrations of this complex are expected to form at low temperatures (~90K). Given the weak nature of the complex, "uninhibited" diffusion of atomic chlorine through the ice matrix at T < 100 K is a possibility. The lack of a third chlorine XPS signal attributed to chlorine (either atomic or molecular) within the bulk ice lends support to this possibility. Assuming diffusion rates for atomic chlorine greater than or equal to diffusion rates found for HCl in ice, the small distance for the chlorine radical to traverse (<< 50 Å) negates the possibility of observing a bulk matrix chlorine signal in the XPS studies.

Also, studies of the thermal desorption of chlorobenzene adsorbed to the surface of amorphous ice produced unexpected results. It was found that the multilayer region of chlorobenzene adsorbed to ice desorbed at a *higher* temperature than did the chlorobenzene monolayer coverage. This indicated that the lateral interaction between adjacent chlorobenzene monomers was greater than the interaction between the chlorobenzene and the ice at the interface. The theoretical investigations of the one to one complex between H_2O and chlorobenzene indicated a weak interaction ~ 1.89 kcal/mol relative to the benzene-H_2O complex (2.21 kcal/mol). It was not possible to calculate the chlorobenzene dimer at the level of theory as the chlorobenzene-H_2O complex with our

current hardware. However, from the experimental observations and assuming similar properties between the molecular and macroscale counterparts, the chlorobenzene dimer is expected to have a higher binding energy relative to the chlorobenzene-H_2O bimolecular complex. Also, theoretical calculations indicate that the orientational and qualitative binding at the interface would primarily be due to hydrogen bonding. We were not able to determine experimentally the orientation of chlorobenzene on the ice surface, but from the theoretical work, it is expected that the chlorobenzene lies parallel with the ice surface. This orientation facilitates π-hydrogen bond formation with dangling hydrogens from the surface of the ice.

Furthermore, the theoretical work presented in this volume indicates some interesting binding interactions between halobenzenes and a water molecule. It was found that chlorobenzene and fluorobenzene both had similar binding energies as well as similar geometries in complexes with H_2O. The similarities suggest that π-hydrogen bonding may be the more dominant binding contribution within the complexes. Moreover, the higher binding energy for the benzene-H_2O complex lends support to this possibility. Given the electron withdrawing capability of fluorine and chlorine, the lower binding energy of the halobenzene-H_2O complexes can be indicative of loss of π electron density in the ring. However, experimental determination of the binding energies and the geometries for chlorobenzene-H_2O and fluorobenzene-H_2O are needed to corroborate the binding theories presented here.

Further studies of this system are required for an adequate treatment of the current experimental observables. Experimental innovations are necessary to explore the diffusion possibility of chlorine radicals in an ice matrix under UHV conditions. It still remains undetermined whether or not the chlorine is being transported through the ice as atomic chlorine or as molecularly bound chlorine which escapes experimental observation by dissociating upon adsorption to the nickel surface during thermal desorption studies. Also, theoretical modeling must incorporate "larger scale" systems to treat adequately the interfacial region of the adsorbate and the ice surface. The calculations presented in this volume suggest that, at least on a molecular level, hydrogen bonded interfacial regions can be explored at the ab initio level of theory. Assuming a correlation between the macroscopic and microscopic regimes, it may be beneficial to extrapolate macroscale information from processes at the molecular level. In the future, computational advancements should allow for a more detailed description and model of hydrogen bonded interfacial systems.

LIST OF REFERENCES

1. Turco, R.P.; Toon, O.B.; Hamill, P. *J. Geophys. Res.* **1989**, 94, 16493.
2. Tolbert, M.A.; Rossi, M.J.; Golden, D.M. *Science* **1988**, 240, 1018.
3. Leu, M-T. *Geophys. Res. Lett.* **1988**, 15, 851.
4. Solomon, S.; Garcia, R.R.; Rowland, F.S.; Wuebbles, D.J. *Nature* **1986**, 321, 755.
5. McElroy, M.B.; Salawitch, R.J.; Wofsy, S.C.; Logan, J.A. *Nature* **1986**, 321, 759.
6. Toon, O.B.; Turco, R.P. *Scientific American* **1991**, 264, 68.
7. Gertner, B.J.; Hynes, J.T. *Science* **1996**, 271, 1563.
8. Haas, B.; Krellin, K.C.; Kuwata, K.T.; Okumura, M. *J. Phys. Chem.* **1994**, 98, 6740.
9. Schindler, T.; Berg, C.; Niedner-Schatteburg, G.; Bondybey, V.E. *J. Chem. Phys.* **1996**, 104, 3998.
10. Tie, X.; Brassuer, G.P.; Granier, C.; Rudder, A.D.; Larsen, N. *J. Geophys. Res.* **1996**, 101, 12575.
11. Dash, J.G.; Fu, H.Y.; Wettlaufer, J.S. *Rep. Prog. Phys.* **1995**, 58, 115.
12. Rowland, B.; Devlin, J.P. *J. Chem. Phys.* **1991**, 94, 812.
13. Leu, M-T.; Moore, S.B.; Keyser, L.F. *J. Phys. Chem.* **1991**, 95, 7763.
14. Chu, L.T.; Leu, M-T.; Keyser, L.F. *J. Phys. Chem.* **1993**, 97, 7779.
15. Graham, J.D.; Roberts, J.T. *J. Phys. Chem.* **1994**, 98, 5974.
16. Blanchard, J.L.; Roberts, J.T. *Langmuir* **1994**, 10, 3303.
17. Schaff, J.E.; Roberts, J.T. *J. Phys. Chem.* **1994**, 98, 6900.
18. Sodeau, J.R.; Horn, A.B.; Banham, S.F.; Koch, T.G. *J. Phys. Chem.* **1995**, 99, 6258.

19. Hobbs, P.V. *Ice Physics* Clarendon Press: Oxford, **1974**, Chapter 1.

20. Porter, G.; Ward, B. *Proc. R. Soc. A.* **1965**, 287, 457.

21. Ichimura, T.; Mori, Y. *J. Chem. Phys.* **1973**, 58, 288.

22. Asada, T.; Nishimoto, K.; Kitaura, K. *J. Phys. Chem.* **1993**, 97, 7724.

23. Jucks, K.W.; Miller, R.E. *J. Chem. Phys.* **1987**, 86, 6637.

24. Szczesniak, M.M.; Scheiner, S. *J. Chem. Phys.* **1985**, 83, 1778.

25. Pribble, R.N.; Garrett, A.W., Haber, K., Zwier, T.S. *J. Chem. Phys.* **1995**, 103, 531.

26. Cheng, B-M.; Grover, J.R.; Walter, E.A. *Chem. Phys. Lett.* **1995**, 232, 364.

27. Frisch, M.J.; Trucks, G.W.; Head-Gordon, M.; Gill, P.M.W.; Wong, M.W.; Forseman, J.B.; Johnson, B.G.; Schlegel, H.B.; Robb, M.A.; Replogle, E.S.; Gomperts, R.; Andres, J.L.; Raghavachari, K.; Binkley, J.S.; Gonzalez, C.; Martin, R.L.; Fox, D.J.; Defrees, D.J.; Baker, J.; Stewart, J.J.P.; and Pople, J.A. *Gaussian 92* Revision A, Gaussian, Inc., Pittsburg PA, 1992.

28. Pople, J.A.; Beveridge, D.L. *Approximate Molecular Orbital Theory* McGraw-Hill Inc., New York, **1970**.

29. Foresman, J.B.; Frisch, A. *Exploring Chemistry with Electronic Structure Methods* Gaussian, Inc., **1993**.

30. Tolbert, M.A.; Rossi, M.J.; Malhotra, R.; Golden, D.M. *Science* **1987**, 238, 1258.

31. Solomon, S. *Nature* **1990**, 347, 347-353.

32. Jones, A.E.; Shanklin, J.D. *Nature* **1995**, 376, 409-411.

33. World Meteorological Organization, **1990**, vol. 1, rep no. 20.

34. Molina, M.J.; Rowland, F.S. *Nature* **1974**, 249, 810.

35. Farman, J.C.; Gardiner, B.G.; Shanklin, J.D. *Nature* **1985**, 315, 207.

36. Hanson, D.R.; Mauersberger, K. *Geophys. Res. Lett.* **1988**, 15, 855.

37. Moore, S.B.; Keyser, L.F.; Leu, M-T.; Turco, R.P.; Smith, R.H. *Nature* **1990**, 345, 333.

38. Toon, O.B.; Tolbert, M.A. *Nature* **1995**, 375, 218.

39. Molina, M.J.; Tso, T.L.; Molina, L.T.; Wang, F.C.Y. *Science* **1987**, 238, 1253.

40. Leu, M.T. *Geophys. Res. Lett.* **1988**, 15, 17.

41. Molina, L.T.; Molina, M.J.; Stachnik, R.A.; Tom, R.D. *J. Phys. Chem.* **1985**, 89, 3779.

42. Oppliger, R.; Allanic, A.; Rossi, M.J. *J. Phys. Chem. A* **1997**, 101, 1903.

43. Molina, M.J. *The Chemistry of the Atmosphere: Its Impact on Global Change* (Oxford University Press, Oxford, **1994**).

44. Chu, L.T.; Leu, M-T.; Keyser, L.F. *J. Phys. Chem.* **1993**, 97, 12798.

45. Banham, S.F.; Sodeau, J.R.; Horn, A.B.; McCoustra, M.R.S.; Chesters, M.A. *J. Vac. Sci. Technol. A* **1996**, 14, 1620.

46. Hanson, D.R.; Ravishankara, A.R. *J. Phys. Chem.* **1992**, 96, 2682.

47. Wang, L.; Clary, D.C. *J. Chem. Phys.* **1996**, 104, 5663.

48. Delzeit, L.; Rowland, B.; Devlin, J.P. *J. Phys. Chem.* **1993**, 97, 10312.

49. Abbatt, J.P.D.; Molina, M.J. *J. Geophys. Res. Lett.* **1992**, 19, 461.

50. Goodman, J.; Toon, O.B.; Pueschel, R.F.; Snetsinger, K.G.; Verna, S. *J. Geophys. Res.* **1989**, 94, 16449.

51. Lide, D.R. *CRC Handbook of Chemistry and Physics* 73rd ed. **1993**.

52. Barnes, H.T.; Vipond, W.S. *Phys. Rev.* **1909**, 28, 453.

53. Leu, C.C.; Carlson, T.A.; Malik, F.B.; Tuckeer, T.C.; Nestorjer, C.W. *Atomic Data 3* 1971, 1.

54. Ichimura, T.; Mori, Y. *J. Chem. Phys.* **1972**, 58, 288-291.

55. Freedman, A.; Yang, S.C.; Kawasaki, M.; Bersohn, R. *J. Chem. Phys.* **1980**, 72, 1028-1033.

56. Ichimura, T.; Nahara, K.; Mori, Y. *J. Photochem.* **1986**, 33, 49.

57. Bunce, N.J.; Ravanal L. *J. Am. Chem. Soc.* **1977**, 99, 4150.

58. Nobl, C.; Benndorf, C. *Surf. Sci.* **1987**, 182, 499-520.

59. Madey, T.E.; Netzer, T.P. *Surf. Sci.* **1982**, 117, 549.

60. Peebles, D.E.; White, J.M. *Surf. Sci.* **1984**, 144, 512.

61. Mayer, E.; Pletzer, R.J. *J. Chem Phys.* **1984**, 80, 2839.

62. Steinruck, H.P.; Huber, W.; Pache, T.; Menzel, D. *Surf. Sci.* **1989**, 218, 293-316.

63. Dean, J.A. *Lange's Handbook of Chemistry* 14th ed., McGraw-Hill, Inc., **1992**.

64. Quickenden, T.I.; Green, T.A.; Lennon, D. *J. Phys. Chem.* **1996**, 100, 16801-16807.

65. Domine, F; Thibert, E.; Van Landeghem, F.; Silvente, E.; Wagnon, P. *Geophys. Res. Lett.* **1994**, 21, 601-604.

66. Wolff, E.W.; Mulvaney, R.; Oates, K. *Geophys. Res. Lett.* **1989**, 16, 487-490.

67. Krishnan, P.N.; Salomon, R.E. *J. Phys. Chem.* **1969**, 73, 2680-2683.

68. Levine, I.N. *Quantum Chemistry* 4th ed. Prentice-Hall, Inc., **1991**.

69. Becke, A.D. *Phys. Rev. A.* **1988**, 37, 785.

70. Lee, C.; Yang, W.; Parr, R.G. *Phys. Rev. B.* **1988**, 37, 785.

71. Vosko, S.H.; Wilkes, L.; Nusair, M. *Can. J. Phys.* **1980**, 58, 1200.

72. Huzinaga, S. *J. Chem. Phys.* **1965**, 42, 1293.

73. Boys, S.F.; Bernardi, F. *Mol. Phys.* **1970**, 19, 553.

74. Pribble, R.N.; Garrett, A.W.; Haber, K.; Zwier, T.S. *J. Chem. Phys.* **1995**, 103, 531.

75. Augspurger, J.D.; Dykstra, C.E.; Zwier, T.S. *J. Phys. Chem.* **1992**, 96, 7252.

76. Bredas, J.L., Street, G.B. *J. Chem. Phys.* **1989**, 90, 7291.

77. Cheng, B.M.; Grover, J.R.; Walters, E.A. *Chem. Phys. Lett.* **1995**, 232, 364.

78. Engdahl, A.; Nelander, B. *J. Phys. Chem.* **1984**, 89, 2860.

79. Gotch, A.J.; Zwier, T.S. *J. Chem. Phys.* **1992**, 96, 3388.

80. Wilson Jr., E.B. *Phys. Rev.* **1934**, 45, 706.

81. Langseth, A.; Stoicheff, B.P. *Can. J. Phys.* **1956**, 34, 350.

82. Watanabe, K.J. *J. Chem. Phys.* **1957**, 26, 542.

83. Cradock, S.; Muir, J.; Rankin, D.W. *J. Mol Struc.* **1990**, 220, 205-215.

84. Hayashi, M; Inagusa, T. *J. Mol. Struc.* **1990**, 220, 103.

85. Sutton, L.E. *Tables of Interatomic Distances and Configurations in Molecules and Ions* The Chemical Society Special Publication, No. 18, The Chemical Society (London), **1965**.

86. Ripoche, X; Asselin, P.; Piuzzi, F.; Dimicoli, I. *Chem Phys.* **1993**, 175, 379.

87. Miller, T.M.; Bederson, B. *Advances in Atomic and Molecular Physics* **1977**, 13, 1.

88. Nelson, R.D.; Lide, D.R.; Maryott, A.A. *Selected Values of Electric Dipole Moments for Molecules in the Gas Phase*, Natl. Stand. Ref., Data Ser.-Natl. Bur. Stnds., **1967**, 10.

89. Hehre, W.J.; Radom, L.; Schleyer, P.V.R.; Pople, J.H. *Ab Initio Molecular Orbital Theory* Wiley-Interscience, New York, **1985**, chapter 6.

90. *Tables of Molecular Vibrational Frequencies.* Part 1., National Bureau of Standards, **1967**.

91. Haas, Y.; Zilberg, S. *J. Am. Chem. Soc.* **1995**, 117, 5387.

92. Shaik, S.S.; Hiberty, P.C.; Ohanessian, G.; Lefour, J.M. *J. Phys. Chem.* **1988**, 92, 5086.

93. Whiffen, D.H. *J. Chem. Soc.* **1956**, 1350.

94. Bist, H.D.; Sarin, V.N.; Ojha, A.; Jain, Y.S. *Spectrochim. Acta* **1970**, 26A, 841.

95. Asada, T.; Nishimoto, K.; Kitaura, K. *J. Phys. Chem.* **1993**, 97, 7724.

96. Arshadi, M.; Yamdagni, R.; Kebarle, P. *J. Chem. Phys.* **1970**, 74, 1475.

97. *NBO Version 3.1*, E.D. Glendening, A.E. Reed, J.E. Carpenter, and F. Weinhold.

VITA

Terry Vaughn was born in Florence, South Carolina on June 28, 1967. He attended schools in the public system of Dillon County, where he graduated from Latta High School in June, 1985. He join the U.S. Army in 1986 and was honorably discharged in 1990. He entered Francis Marion University, South Carolina during June of 1991 where in May, 1993, he received the Bachelor of Science in Chemistry. He then entered the Ph.D. program at the University of Tennessee, knoxville in the fall of 1993, officially receiving the Ph.D. degree in December of 1997. He is presently a postdoctoral fellow with the Tropospheric Trace Gases and Airborne Measurements Group (TTGAMG) in the Earth and Atmospheric Sciences department at the Georgia Institute of Technology.